Long-Term Timing
of Millisecond Pulsars
and Gravitational Wave Detection

Joris Paul Wim Verbiest
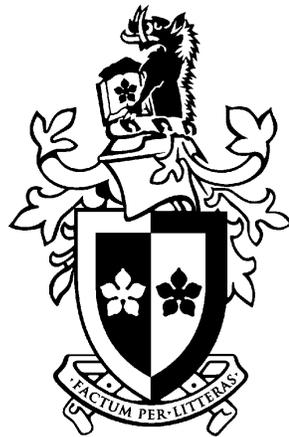
"I know nothing, except the fact of my ignorance."

Socrates, as cited by *Diogenes Laertius* in "The Lives and Opinions of Eminent Philosophers"

Abstract

This thesis presents the results from a long-term timing campaign on 20 millisecond pulsars (MSPs). The stability of these pulsars is analysed in order to allow assessment of gravitational wave (GW) detection efforts through pulsar timing. In addition, we present a new method of limiting the amplitude of a stochastic background of GWs and derive a strong limit from applying this method to our data.

GWs are a prediction of general relativity (GR) that has thus far only been confirmed indirectly. While a direct detection could give important evidence of GW properties and provide insight into the processes that are predicted to generate these waves, a detection that contradicts GR might herald a breakthrough in gravitational theory and fundamental science. Two types of projects are currently being undertaken to make the first direct detection of GWs. One of these uses ground-based interferometers to detect the GW-induced space-time curvature, the other uses pulsar timing. This thesis is concerned with the latter: the Pulsar Timing Arrays (PTAs).

The high stability of some MSPs, along with ever increasing levels of timing precision, has been predicted to enable detection of GW effects on the Earth. Specifically, it has been shown that if the timing precision on 20 MSPs can be maintained at levels of $\sim$100 ns during five years to a decade, a correlated effect owing to GWs from predicted cosmic origins, can be detected. However, no timing at a precision of 100 ns has been maintained for more than a few years - and only on a few pulsars.

After combining archival data and employing state-of-the-art calibration methods, we achieved 200 ns timing precision over 10 years on PSR J0437−4715 - which is a record at such time scales. This high stability in itself provides several interesting measurements, for example of the variation of Newton's gravitational constant and of the pulsar mass.

We also present long-term timing results on 19 other pulsars that constitute the Parkes PTA. Our results show that most pulsars in our sample are stable and dominated by receiver noise. The potential for sub-100 ns timing is demonstrated on two of our brightest sources. These timing results are used to estimate timescales for GW detection of potential PTAs worldwide and to limit the amplitude of GWs in the data. Our limit of $A < 1.0 \times 10^{-14}$ for a background with $\alpha = -2/3$ is slightly more stringent than the best limit published yet.

Acknowledgments

This thesis would not have been if Matthew and Dick hadn't trusted me to bring it to a good end. I'm not sure how I deserved that trust nearly four years ago, but I hope to have earned it by now, because both of my supervisors have provided me with just about anything a student could hope for. First and foremost, it was an honour and a pleasure to find myself steeped into a project as exciting and fascinating as P140 and the PPTA. At the outset I didn't know enough about pulsar timing to fully grasp it, but through the years I have continuously increased my appreciation of the project and collaborators I have been offered - and for which I may not have shown enough gratitude at the time. Beyond the greatness of the project, I should of course acknowledge the supervision and general support I have received throughout the past 42 months. The patient explanations, discussions that often went on for much longer than they needed to and the freedom to let me find my own way - all of it is very much appreciated. As my primary supervisor, I thank Matthew for frequently pulling away from the busy schedule he has, to provide the pearls of wisdom and daring guidance I needed to progress.

Academically speaking, the post-docs come after the professors. Invaluable to students like myself, they taught me all I needed to know with endless patience and have as such provided me with a great example of what I should aspire to become after graduation. In addition to a whole lot more scientific and less-than-scientific stuff, George (who doesn't believe in acknowledgements, so I'll be brief) taught me C in just about a day - it sounds like a miracle and I'm not sure how he managed it. Willem was never annoyed or irritated when I came up with yet another PSRCHIVE bug that turned out to be a typo on my behalf - or when I asked him the same question over and over again, fundamentally coming down to "explain me polarisation and don't use math". Ramesh's knowledge about the ISM turned out to be a boundless source of information which helped me understand the background to what I was actually doing. He would - like just about every pulsar astronomer I've come to know - take as much time as I could possibly ask for to get the final tiny misunderstandings I might have ironed out, no matter how boring or basic my problems may have seemed to him.

I only met Bill Coles halfway through my thesis but his influence is undeniable. It took me a while to get used to his engineering approach and his e-mails full of mathematical, spectral and statistical jargon generally took me three hours to read and three more hours to (mostly) understand, but they were always useful and

never dull. Rick Jenet, Simon Johnston, David Champion, Andrea Lommen, Barney Rickett, Russell Edwards, Dan Stinebring, Mark Walker and Steve Ord should also be mentioned in the category of great people who sadly live far away (at times) but are always willing to help a simple student wrap his mind around something finicky.

Another group of people that has been of vital importance to my thesis and my appreciation of pulsar astronomy in specific and radio astronomy in general, is the Parkes staff. I haven't calculated what percentage of "my" data was obtained by John Sarkissian, but it must be heaps. John was also almost always there when I was observing - sacrificing sleep and (more importantly) family time so that I could leave for lunch. John and I may disagree on a few worldly issues, but that doesn't deny the fact that I will longingly look back at the lively debates we had in the control room - and the great 3D pictures of just about any interesting place in the Solar System. In the past decade "Parkes" has nearly become synonymous with John Reynolds. The indefatigable attitude JR displayed in trying to fix anything that *might* negatively affect observations was astonishing and I, like all other observers, am utterly grateful. Beyond the two Johns, the entire Parkes staff has been more than helpful and accommodating in attempting to create a flawless scientific instrument and a home away from home. Thanks therefore to all of you: Andrew, Anne, Brett[2], Geoff, Gina, Janette, Julia, Mal, Shirley, Simon, Stacy and everyone I've forgotton to mention.

At Swinburne as in Sydney, work only goes so far in turning "survival" into "life". Luckily there were many friends along the way, some long gone, others just arrived, who provide some comic relief to give my brain the occasional rest. Thanks therefore to my housemates: Simon, Nadia, Meg, Paul, Elaine, Thomas and Lenneke for introducing me to the best TV series I know and for the discussions and insights in subjects as varied as sub-atomic physics, Australian culture and German cuisine (though mostly sub-atomic physics). Thanks also to my fellow students and office-mates (both in Swinburne and at the ATNF): Xiao Peng, Trevor, Tim, Sarah, Paul, Nick, Natasha, Meredith, Max[2], Lina, Lee, Kathryn, Jeremy, Haydon, Emily, Emil, Daniel, Chris, Caroline, Berkeley, Annie, Anneke, Andy, Alyson, Albert, Adrian and Adam for both encouraging and preventing procrastination, for lunch and dinner, for the Age Superquiz, for telling me more than I needed to hear about AFL and rugby. For poker, movies, music. For drinks and laughter. For taking me seriously, but not too seriously. For camping and hikes. For sleep-deprived comedy at 4am in the Parkes control room. And for pointing out the obvious. Apart from housemates and fellow students, the frisbee crowd provided me with an energy release that money cannot buy. Thanks for putting up with my galloping across your field, guys.

Last but not least, thanks to the people I've been neglecting most of all: my father, who predicted twenty years ago that I'll become a particle physicist; my mother, who keeps on defying the Universe in her claim that Australia is a long way from Belgium; and my siblings, Kathleen & Maarten, who are in their own way close while distant. It's the four of you - and the eighteen years I've lived with you in Belgium, that have provided me with the dauntless international vision that brought me to the other end of the world and with the scientific intrigue that made

me want to understand the Universe and, above all, gravity.

Declaration

This thesis contains no material that has been accepted for the award of any other degree or diploma. To the best of my knowledge, this thesis contains no material previously published or written by another author, except where due reference is made in the text of the thesis. All work presented is primarily that of the author. Chapters 3 and 4 have appeared in or been submitted to refereed journals. In each case, I authored the majority of the text, receiving limited assistance with the style and content of some sections. My supervisors, close colleagues and a number of anonymous referees helped to refine each manuscript. Appendix A is submitted to a refereed journal as appendix to the article containing Chapter 4. The mathematical derivation presented in this Appendix was constructed with guidance from William Coles. The research in Chapter 5 was performed in close collaboration with George Hobbs, William Coles and Andrea Lommen and most of its contents will be duplicated in a paper to be written by one of these three collaborators. Chapter 5 itself, though, is written independently and authored by myself alone.

This thesis analyses data recorded at the Parkes radio telescope during a 15 year period. The relevant observing proposals (P140 and P456) are both still ongoing. During my time at Swinburne, observations for these projects were made by a team of astronomers including mostly Matthew Bailes, Willem van Straten, Ramesh Bhat, Albert Teoh, Sarah Burke-Spolaor and myself from Swinburne University and Richard Manchester, George Hobbs, John Sarkissian, Russell Edwards, David Champion and Daniel Yardley from the Australia Telescope National Facility (ATNF). John Reynolds, Brett Dawson and Brett Preisig have assisted with telescope operations. Aidan Hotan and Steve Ord have supported the running of CPSR2 when required and provided occasional observing assistance.

Support with debugging and development of the PSRCHIVE software scheme was provided by Willem van Straten and assistance with the Tempo2 software was provided by George Hobbs.

Joris Paul Wim Verbiest, January 2009

Contents

List of Figures

List of Tables

Chapter 1

Introduction: On Pulsars and Gravity

With all reserve we advance the view that a super-nova represents the transition of an ordinary star into a *neutron star*, consisting mainly of neutrons.
Baade & Zwicky, "Cosmic Rays from Super-novae", Proceedings of the National Academy of Sciences, 1934

When Hewish et al. (1968) serendipitously discovered the first pulsar in 1967, they hypothesised these new objects might be related to neutron stars - dense remnants of supernova explosions, first proposed by Baade & Zwicky (1934). Gold (1968) and Pacini (1968) further investigated the properties of pulsar emission and first proposed the "lighthouse model" as an explanation for the regularity of the pulses. According to this model, the radio waves originate from near the magnetic poles, which are offset from the rotation axis of the neutron star - causing the emission to sweep through space like that generated by a lighthouse. While this model provides a geometric explanation to many characteristics, the actual mechanism that generates the pulsar radiation remained unexplained. Goldreich & Julian (1969) and Ruderman & Sutherland (1975) analysed several possibilities, leading to a simplified electrodynamic model of pulsar radiation. This allowed the now standard classification of pulsars according to characteristic age and surface magnetic field strength, based on the assumption of magnetic dipole radiation (Ostriker & Gunn 1969; Chen & Ruderman 1993).

Within a decade of the initial pulsar discovery, Hulse & Taylor (1975) identified the first pulsar in a binary system. This particular system, PSR B1913+16, consists of two neutron stars in close orbit around each other. It consequentially exhibits many gravitational effects that are predicted by general relativity but had thus far been impossible to measure (Smarr & Blandford 1976). One of these effects was the emission of gravitational radiation. Taylor & Weisberg (1982) used the

PSR B1913+16 binary to make the first indirect detection of gravitational waves caused by the centripetal acceleration in the binary system. Also in 1982, Backer et al. (1982) discovered yet another type of radio pulsar: the first millisecond pulsar PSR B1937+21, with a rotational frequency of well over 600 Hz. Since evolutionary scenarios for this highly "spun-up" type of pulsar required a binary system (Bhattacharya & van den Heuvel 1991), the fact that PSR B1937+21 is a single pulsar defies common theories. Potential alternatives were proposed by Henrichs & van den Heuvel (1983) and Ruderman & Shaham (1983), but are hard to verify. Yet another class of related objects was discovered a decade later by Duncan & Thompson (1992): the magnetars. These more slowly rotating objects (pulse periods up to 10 s or more) have higher magnetic field strengths than radio pulsars. Accepted models had suggested that radio wave production would not occur at such long periods and high magnetic field strengths, which was in agreement with the fact that magnetars were only observable in X-rays and γ-rays. Recently, though, Camilo et al. (2006) did detect radio pulses from magnetar AXP XTE J1810$-$197, in contradiction to models for radio pulsar emission mechanisms. Another few recent discoveries that demonstrate the complexity of the pulsar emission mechanism, are the intermittent pulsars (Kramer et al. 2006a) and the rotating radio transients (RRATs; McLaughlin et al. 2006), both of which behave like normal pulsars at some times, but are entirely undetectable at others.

This chapter will provide an introduction into pulsars, their basic characteristics and how they can be used to study, amongst other things, gravity. Section 1.1 gives an overview of the origins and typical characteristics of both common and millisecond pulsars. The technique of pulsar timing is described in Section 1.2, along with its application to measuring properties of pulsars, the interstellar medium and the Solar System alike. In Section 1.3, we will look more closely at the effect gravitational waves have on pulsar timing and how this effect may be detected. Finally, Section 1.4 provides the outline for the rest of the thesis.

1.1   Pulsars and Millisecond Pulsars

1.1.1   Birth of a Neutron Star

Most stars are in a state of hydrostatic equilibrium provided by the gravity of their own mass on one hand and nuclear synthesis on the other. A fundamental requirement for nuclear synthesis is that atoms come close enough together for the nuclear binding force (the *strong nuclear force*) to overtake the electromagnetic repulsive force. Since the nuclear charge of heavier atoms is higher, this condition requires more pressure and higher temperatures for fusion of heavier elements. Therefore, as ever heavier elements are fused, the core of the star is expected to gradually contract, allowing a pressure gradient to form, resulting in different stages of nuclear fusion at different distances from the centre of the star. If the star is massive enough ($\gtrsim 10\,\mathrm{M_\odot}$; Prialnik 2000), this chain reaction should eventually result in the

production of iron. Since iron is the element with the highest binding energy per nucleon, fusion beyond iron will require energy rather than release energy, meaning that the equilibrium cannot be sustained by further fusion. As a result, an iron core is predicted to grow at the centre of the star, sustained by electron degeneracy pressure (which is a quantum-mechanical pressure that follows from the Pauli exclusion principle). This pressure can, however, only sustain bodies of masses up to the Chandrasekhar mass ($\sim 1.4\,M_\odot$; Chandrasekhar 1931). Once the core grows beyond this mass, it collapses under its own weight, causing dramatic rises in temperature and pressure, which causes the iron to dissociate back into single nucleons - and after that, fusing protons and electrons into neutrons. According to present theories, this collapse either continues until a body of infinite density is created (a *black hole*) or until it is halted by neutron degeneracy pressure (which is similar in principle to electron degeneracy pressure, but exists at higher densities). In this latter case the implosion is suddenly halted, causing the mantle and outer layers of the star to be pushed outward in a giant shockwave. This cataclysmic collapse is known as a core-collapse supernova explosion; the material that is expelled in the shock wave evolves into a supernova remnant (a well-known example being the Crab nebula) and the core that stays behind, is a neutron star or - if observable - a pulsar (Baade & Zwicky 1934).

1.1.2   Discovery and Fundamental Properties

When Baade & Zwicky (1934) predicted the existence of neutron stars, observational evidence in support of this work was not expected because no mechanism to create radiation was known, besides blackbody radiation which would vanish quickly as the star cooled. However, the discovery of radio pulsations by Hewish et al. (1968), was soon linked to neutron stars by Gold (1968) and Pacini (1968). They argued that, given the short and extremely accurate periodicities of the observed radio pulsations, neutron stars were the only likely source of this radiation. Furthermore, they hypothesized that the radio emission would originate from compact regions within the pulsar magnetosphere which rotates with the pulsar, thus creating a rotating beam of radiation. If the radiation beam intersects our line of sight at any point of the pulsar's rotation, we will see periodic pulses. Proposed in 1968, this model (known as the lighthouse model) still lies at the basis of our understanding of pulsars, but fails to explain the physical process that generates the radiation. Many attempts have been made to identify the mechanism that creates the radiation (see e.g. Goldreich & Julian 1969; Ruderman & Sutherland 1975), or to pin down the precise region from which the radiation emanates, but no conclusive argument has been presented (Melrose 2004). The main difficulties for any comprehensive explanation of pulsar emission are the similarity of emission characteristics for wide ranges of pulse period and magnetic field strength - as evidenced by the largely comparable pulse profiles and polarisation properties of most pulsars. Other problems are the coherency of the radio emission and the broad spectrum of the emission - with coherent radio

emission at frequencies as low as several hundred MHz (or lower) and up to $10\,\text{GHz}$ or higher. Non-standard behaviour seen in many of the slower and some of the fast pulsars, such as drifting subpulses, periodic nulling, giant pulses or sudden spin-ups, introduce further constraints on this complicated analysis.

Gold also predicted that a slight decrease in spin frequency would be detected as a consequence of energy loss. Pulsars do indeed lose energy due to magnetic dipole radiation (caused by the rotation of the pulsar's magnetic field) and classical electromagnetic theory can therefore relate the loss of angular momentum to the strength of the pulsar's magnetic field, as derived in Manchester & Taylor (1977) after Goldreich & Julian (1969):

$$B_0 \approx \sqrt{\frac{3Ic^3P\dot{P}}{8\pi^2R^6}}, \tag{1.1}$$

where B_0 is the characteristic magnetic field strength at the pulsar surface (in Gauss), I is the moment of inertia for the pulsar, $c = 3 \times 10^8\,\text{m/s}$ is the speed of light in vacuum, R is the radius of the pulsar and P and $\dot{P}$ are the pulsar spin period and period derivative, respectively. With all pulsar masses determined to date varying between one and two solar masses and since the radius of a pulsar is expected to be around $10\,\text{km}$ (as derived from equations of state for dense nuclear matter), we can calculate the moment of inertia, assuming the pulsar approximates a solid sphere:

$$I \approx 0.4MR^2 \approx 10^{45}\,\text{g cm}^2.$$

This can be substituted in turn, reducing Equation 1.1 to:

$$B_0 \approx 3.2 \times 10^{19}\sqrt{P\dot{P}} \tag{1.2}$$

with B_0 in Gauss.

An alternative means of using the spindown is to analyse the energy loss due to magnetic dipole radiation. Equating the loss of rotational energy as observed through the spin period derivative to the energy loss predicted from magnetic dipole radiation, provides a relationship between the spin period and its first time derivative (Lorimer & Kramer 2005):

$$\dot{P} = \frac{2(2\pi)^{n-1}\,m\,sin^2\alpha}{3Ic^3}P^{2-n}, \tag{1.3}$$

with m the magnetic dipole moment, α the angle between the magnetic and rotation axes and n the braking index; $n = 3$ for pure magnetic dipole emission. Differentiating this Equation again and replacing the constant fraction with $\dot{P}P^{n-2}$ allows solving for n:

$$n = 2 - \frac{P\ddot{P}}{\dot{P}^2} = \frac{\nu\ddot{\nu}}{\dot{\nu}^2} \tag{1.4}$$

in which $\nu = 1/P$ is the spin frequency and $\dot{\nu}$, $\ddot{\nu}$ are its first and second time-derivatives. This Equation allows n to be determined, as has been done for six pulsars to date, with values ranging from 2.14 for PSR B0540−69 (Livingstone et al. 2007) to 2.91 for PSR J1119−6127 (Camilo et al. 2000). This suggests a spindown mechanism other than pure magnetic dipole radiation is at work, though this could be due to the small number statistics. Johnston & Galloway (1999) performed a different analysis which was applicable to many more pulsars and found a large variation in braking indices. However, timing irregularities in the pulsars of their sample may have corrupted their results.

Equation 1.3 can be integrated to give:

$$\text{Age} = \frac{P^{n-1} - P_0^{n-1}}{(n-1)K}, \tag{1.5}$$

where P_0 is the initial spin period and K is the constant fraction in Equation 1.3, which can therefore be replaced by $K = \dot{P}P^{n-2}$. Rewriting provides:

$$\text{Age} = \frac{P}{\dot{P}(n-1)} \left(1 - \left(\frac{P_0}{P} \right)^{n-1} \right). \tag{1.6}$$

Assuming $P_0 \ll P$ and $n = 3$, results in the simple relation

$$\text{Age} = \tau_c = \frac{P}{2\dot{P}} \tag{1.7}$$

(a more rigorous derivation of which is presented by Ostriker & Gunn 1969). While this value is easily derived from observations, the assumptions that entered into its derivation must be noted, as well as the fact that much of the pulsar emission mechanism is still badly understood.

1.1.3 The $P - \dot{P}$ diagram

Since period (P) and spindown ($\dot{P}$) are amongst the most readily determined parameters pertaining to pulsars, a straightforward tool to compare and analyse pulsar properties is the $P - \dot{P}$ diagram (Figure 1.1). The clearest feature in this plot is the "island" where most pulsars reside, with spin periods between 0.1 and a few seconds and magnetic field strengths of typically 10^{11} to 10^{13} Gauss. These pulsars are generally called *normal pulsars*. Also, while the diagram is reasonably well filled, the right-hand edge is remarkably empty, even at characteristic ages well below a Hubble time. This is because as pulsars spin down, they eventually have too little energy left to produce radio waves, causing them to "turn off" at longer periods. The virtual line across which this happens, is called the *death line* - while there are still neutron stars beyond this line, they can no longer produce radio waves and are therefore invisible to us. The few pulsars that do show up beyond the death line show that this phenomenon is not strictly a function of the surface magnetic field
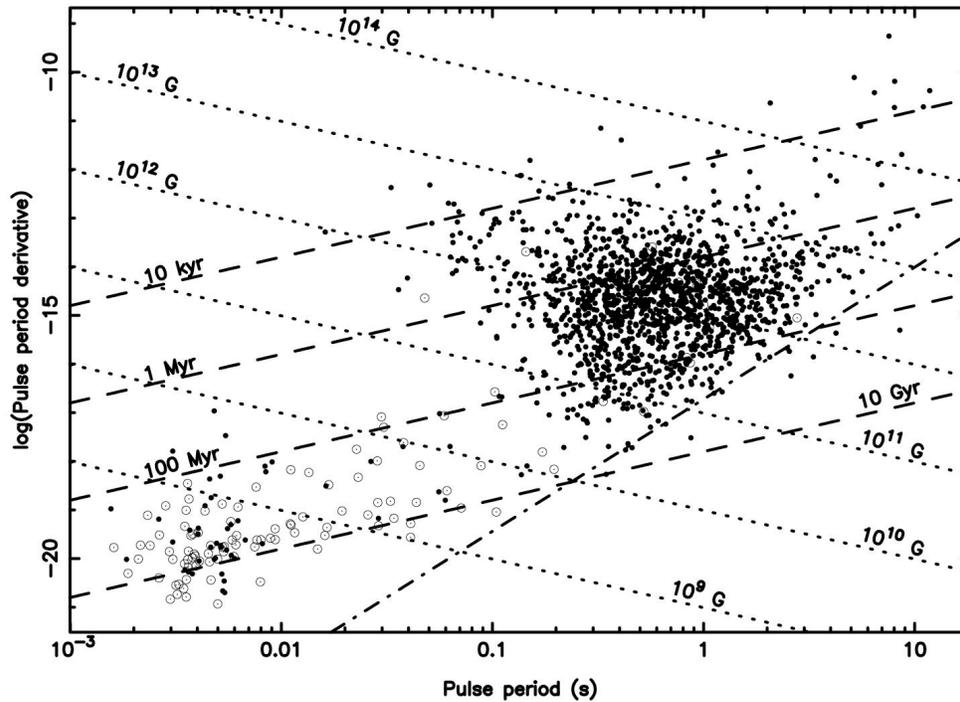
Figure 1.1: $P - \dot{P}$ diagram of all pulsars currently available in the ATNF pulsar catalogue. Inclined dashed lines show the characteristic age ($\tau_{\rm c}$) of the pulsars, the dotted lines give the surface magnetic field strength (B_0) and the dash-dotted line is a death line proposed by Chen & Ruderman (1993). Dots represent single pulsars; circled dots represent pulsars in binary systems.

strength and pulse period, but also depends on the more general geometry of the magnetic field, as more fully described by Chen & Ruderman (1993).

Besides the normal pulsars, there are two categories with somewhat different characteristics. One fairly small group is positioned in the top right-hand corner, with extremely high magnetic fields and long pulse periods. These sources are called magnetars (Duncan & Thompson 1992), given their strong magnetic fields. Observationally, these are either seen in X-rays - in which case they are called "anomalous X-ray pulsars" or AXPs - or in soft γ-rays as so-called "soft gamma repeaters" or SGRs. Radio emission from magnetars was expected to be absent because the magnetic fields are too strong to allow standard scenarios of radio wave creation, but this view was recently compromised with the discovery of pulsed radio emission from the AXP XTE J1810$-$197 (Camilo et al. 2006).

1.1.4 Binary and Millisecond Pulsars

Finally, in the bottom left-hand corner of the $P - \dot{P}$ diagram, there is a second island of pulsars, composed of the millisecond pulsars (MSPs). These pulsars, with higher spin periods, slower spindowns and far weaker magnetic fields ($B_0 = 10^8$ to 10^{10} Gauss), were first discovered in 1982 (Backer et al. 1982). As Figure 1.1 shows, this class of pulsar is found in binary systems much more often than any other class of pulsar. Current theory suggests this is a side-effect of the evolutionary cycle of MSPs, since they are predicted to originate from the heavier star in a binary system, as outlined below.

At the start of this chapter, we have described the evolution of a star based on the progression of nuclear fusion in its core: nuclei get fused into heavier elements until iron is formed. The speed of this process is proportional to the mass of the star cubed: heavier stars undergo greater gravitational forces and therefore incite faster nuclear fusion to provide a greater pressure, resulting in hydrostatic equilibrium. This implies that the stages of a star's life cycle are shorter for heavier stars. A consequence of this is that the heaviest star of a binary system is the first one to evolve and - if it is sufficiently heavy - become a neutron star. When subsequently the companion star evolves into a red giant, its outer shells can grow beyond the equipotential surface of the two stars and hence matter will transfer onto the neutron star. Conservation of angular momentum of this matter (which falls off the outer shells of the giant and onto the far smaller core of the neutron star), causes the neutron star to increase its rotational frequency by orders of magnitude (Bhattacharya & van den Heuvel 1991). During this spin-up phase, the binary system is observed as an X-ray binary, as the accreting matter emits strongly in X-rays (Bhattacharya & van den Heuvel 1991).

At this point, there are again two distinct possibilities: either the companion is not very massive, which means its evolution will go slowly and it will eventually become a white dwarf. In that case the matter transfer will continue for a long while and the neutron star will be spun up to periods of milliseconds - as is clearly

the case for the first MSP discovered (PSR B1937+21, $P = 1.558$ ms) and for all MSPs in the bottom-left corner of the $P - \dot{P}$ diagram. The alternate possibility is that the companion star is heavy enough to become a neutron star itself. In that case its evolution will go more rapidly and the spin-up period will not last as long. This results in a double neutron star system, of which one star resides in the main $P - \dot{P}$ island with the normal pulsars and the other on the "bridge" linking the normal pulsars with the MSPs - with a pulse period of the order of tens to hundreds of milliseconds. As derived in detail by Smarr & Blandford (1976), this is how the first binary pulsar to be discovered evolved: PSR B1913+16 with a pulse period of $P = 59$ ms (Hulse & Taylor 1975).

There are currently 111 MSPs known[1] of which 49 reside in globular clusters (GCs). There are two main reasons why such a large fraction of known MSPs reside in GCs. Firstly, the high stellar density of GCs allows formation of binary star systems through capture in close encounters. This results in a larger density of X-ray binary sources, which in turn generates a relatively larger amount of MSPs (Verbunt, Lewin & van Paradijs 1989). The second reason is that GCs are easy targets for surveys, while surveys for non-globular MSPs require vastly larger amounts of observing time due to the inherently larger sky coverage. The stellar density of GCs has a two-fold effect on pulsar timing. Firstly, it causes acceleration terms that affect timing stability over long time spans (years to decades; see Chapter 4). Secondly, it drastically increases the likelihood of binary systems being disrupted. Because of this, only about half of the GC MSPs are part of a binary system. For the non-globular (or field) MSPs, close to 75% are binaries. The origin of the 17 single field MSPs has been an item of some debate. While supernovae of either star in a binary can - and do - increase the spatial velocity and orbital eccentricity of the system, in the case of a neutron star with a less massive companion, this effect should not nearly be large enough to disrupt the system. This has led to various scenarios for the formation of single MSPs, including neutron star mergers (Henrichs & van den Heuvel 1983) and the disruption of the low-mass companion star into either a debris disk or a planet-sized object (Ruderman & Shaham 1983).

1.2   Pulsar Timing

1.2.1   Pulsar Timing Basics

The lighthouse model suggests that the pulses of radio emission we receive from pulsars always come from the same phase in the pulsar's rotation. If this is true and the region from which the emission comes is stable, then the times-of-arrival (TOAs) of the pulses can be determined and compared to a timing model. In practice this is indeed possible, though there are two reasons why pulses are generally not

---

[1]According to the ATNF Pulsar catalogue: http://www.atnf.csiro.au/research/pulsar/psrcat; Manchester et al. (2005) and following the definition of $P < 20$ ms and $\dot{P} < 10^{-16}$.
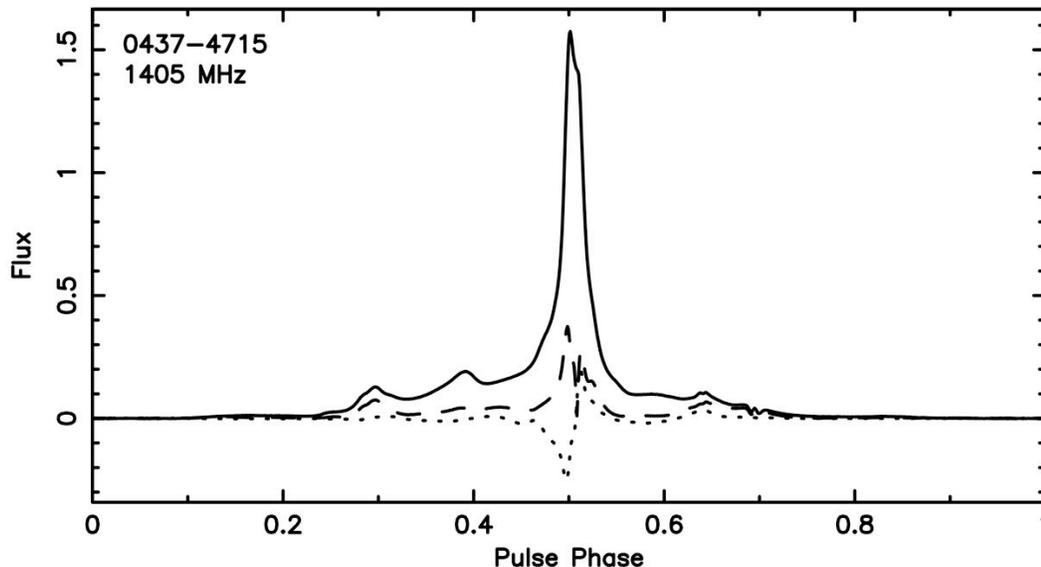
Figure 1.2: Pulse profile of PSR J0437−4715 at an observing frequency of 1405 MHz, showing the linear (dashed) and circular (dotted) Stokes parameters as a function of pulse phase.

timed individually. Firstly, it has been shown that the emission is not perfectly stable: the shape of single pulses varies considerably (Helfand, Manchester & Taylor 1975). Averaging a train of consecutive pulses does, generally, result in a stable *average profile*, which can be timed to high precision. The second reason for adding consecutive pulses is to reduce the radiometer noise: application of elementary radio astronomy theory to pulsed emission (as e.g. in Lorimer & Kramer 2005) shows that the strength of the emission (*signal*) relates to the noise introduced by the system temperature (*noise*) as follows:

$$\mathrm{SNR} = \sqrt{N_\mathrm{p} B t} \left(\frac{G S_\mathrm{peak}}{T_\mathrm{sys}} \right) \sqrt{\frac{P - W}{W}}, \tag{1.8}$$

with SNR the signal-to-noise ratio, N_p the number of polarisations measured, B the bandwidth, t the integration time of the profile, S_peak the peak brightness of the pulsar, T_sys the system noise temperature, W the on-pulse width, P the pulse period and $G = \eta_\mathrm{A} A/(2k_\mathrm{B})$ is the telescope gain based on the aperture efficiency η_A, the telescope aperture A and Boltzmann's constant k_B.

The main complexity of determining TOAs lies in the complicated shape many pulse profiles have. As an example, the average pulse profile of PSR J0437−4715 (which will be described in much more detail in Chapter 3) is presented in Figure 1.2. Clearly, the peak in itself could be used for timing, but much more precise measurements can be achieved by using the entire pulse profile. Practically, therefore, timing works as follows: during observations, the period of the pulse is derived from a timing model derived from previous observations. Given that period, the

data are *folded* in real time - i.e. data samples with the same phase (time modulo pulse period) are averaged. After storing the times when the observation started and finished, based on the observatory atomic clock, the folded observation is stored with a timestamp denoting its centre. At this point the actual position of the pulse is still not yet defined, so the timestamp in itself only provides the time of the observation, not the time the "average" pulse arrived. For that information to be derived, the observation is cross-correlated with a template profile. These templates can fundamentally be any non-constant function, but in order to take full advantage of the pulse shape, it is made to resemble the average pulse as closely as possible. Throughout the analysis done for this thesis, the standard profiles are constructed through addition of the brightest observations available. An alternative method that is gaining popularity, is to construct an analytic template, based on fitting of standard analytic functions to a high SNR observation. This method has the advantage of having a noiseless baseline.

From the cross-correlation of the observation and the standard profile, one can derive the phase offset between the two profiles, which can be added to the time stamp to provide a site-arrival-time (SAT). It must be noted that these times are not absolute in the sense that they depend on the pulse phase of the template profile. However, if the same template is used for all observations, this constant offset will be the same in all SATs and is therefore irrelevant, since absolute phase is practically inachievable.

The next step in the analysis is to transfer the SAT to an inertial reference frame: the Earth's rotation around the Sun causes the SATs to be strongly influenced by the position of the Earth throughout the year. To translate the SATs to barycentric-arrival-times or BATs (in this context, the barycentre is the centre of mass of the Solar System), one needs accurate predictions of the masses and positions of all the major Solar System objects at any point in time. These predictions - so-called Solar System ephemerides (SSE) - are provided by several organisations worldwide. For the work presented in this thesis, the DE200 and DE405 JPL SSE were used (Standish 2004). Alternatives are the INPOP06 from the Observatoire de Paris (Fienga et al. 2008) and the EPM2004 from the Russian Academy of Sciences (Pitjeva 2005). This variety demonstrates that, while these ephemerides are all up to very high standards, they do contain uncertainties and errors, which are not taken into account in the conversion from SAT to BAT - and are therefore a cause of unaccounted timing irregularities, as we will show in more detail in §3.3.3.

Finally, the BATs are subtracted from arrival times predicted by a timing model of the pulsar. The difference between these two quantities (the *timing residuals*) are the real tools of pulsar timing: initially they are used to improve the estimates of timing model parameters, but since all unmodelled physics is contained within them, it is the analysis of these timing residuals that will allow measurement of new effects, determination of new parameters and provide limits on the influence of predicted effects, such as gravitational wave backgrounds. In the remainder of this section, we will provide an insight into the potential components and complexities

of pulsar timing models.

1.2.2 Spin and Astrometric Parameters

Every timing model starts out with the most fundamental parameters, which are determined at the discovery of the pulsar: spin frequency (ν), position in right ascension and declination (α and δ, respectively) and dispersion measure (DM, discussed in the next section). After about a year, the frequency derivative ($\dot{\nu}$) can also be determined. These five parameters constitute a simple timing model and their effect on timing residuals can relatively easily be understood. An incorrect pulse frequency in the timing model will cause the predicted arrival time of a pulse to become incrementally wrong with time, resulting in a linear trend in the residuals (Figure 1.3 a). A significant error in $\dot{\nu}$ causes the frequency to be increasingly off and therefore results in a steepening residual trend - seen as a quadratic signature in the timing residuals (Figure 1.3 b). An incorrect position corrupts the transfer from SAT to BAT and thus introduces a sine wave with a period of a year (Figure 1.3 c). After a while, the proper motion (μ) may also be detected. Its effect is also a sine wave, but with an amplitude that increases linearly with time, as shown in Figure 1.3 d.

A final astrometric parameter that can be determined in some cases, though not all, is parallax. In all astronomy short of pulsar timing, parallax is the apparent yearly wandering of a nearby star with respect to a background source such as a galaxy (see Figure 1.4 a). This changing of the relative position between the star and background object is caused by the fact that the Earth moves so that we look at the object from a slightly different angle. In pulsar timing, the relative position of the pulsar with respect to a background object is not measurable, since only the pulsar is timed. However, the closer the pulsar is, the stronger the wave front is curved - this induces a delay that is maximal when the pulsar is at a right angle to the Earth-Sun line (see Figure 1.4 b). As opposed to the geometric parallax, though, pulsar timing parallax signatures are practically unmeasurable when the pulsar is far away from the ecliptic plane - since the same part of the wavefront hits the Earth at all positions in its orbit. (This is particularly true because the Earth's orbit is nearly circular.)

Mathematically, these astrometric delays can be derived from the relative positions of the pulsar and Earth. Let $\vec{p}$ be the vector pointing from the telescope to the pulsar, $\vec{r}(t)$ the vector from the telescope to the Solar System barycentre (SSB) and $\vec{d}$ the vector from the SSB to the pulsar. Now also introduce the pulsar's velocity vector $\vec{v}$ so that $\vec{p} = \vec{r} + \vec{d} + (t - t_0)\vec{v}$. Following the analysis by Edwards, Hobbs & Manchester (2006), the travel time between the pulsar and the telescope becomes (ignoring binary effects and effects due to the interstellar medium):

$$|\vec{p}| = |\vec{d}| + |\vec{v}_{\parallel}|(t - t_0) + |\vec{r}_{\parallel}| + \frac{1}{|\vec{d}|}\left(\frac{|\vec{v}_{\perp}|^2}{2}(t - t_0)^2 + \vec{v}_{\perp} \cdot \vec{r}_{\perp}(t - t_0) + \frac{|\vec{r}_{\perp}|^2}{2}\right), \quad (1.9)$$
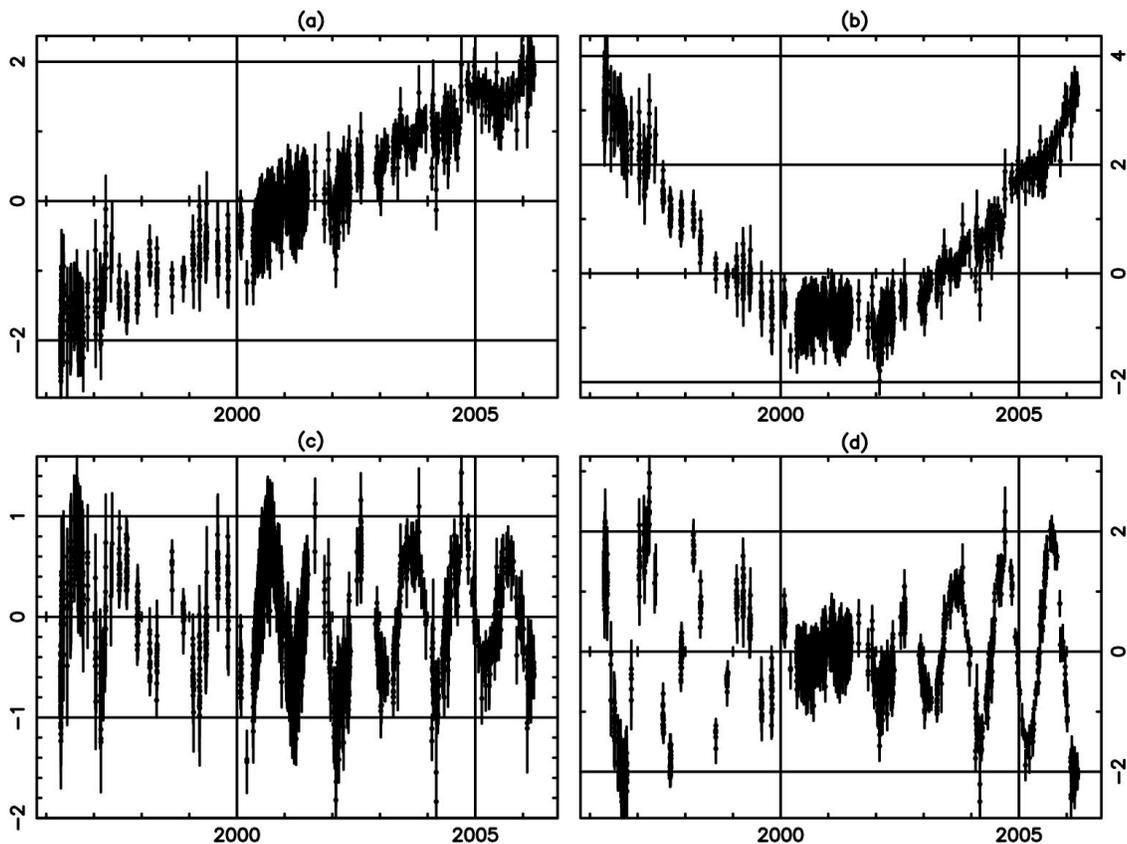
Figure 1.3: Residual signatures of basic timing parameters. Year is displayed on the x-axis; the residuals in microseconds are displayed on the y-axis. (a) Linear trend due to error in ν; (b) quadratic signature of $\dot{\nu}$; (c) sine wave with yearly periodicity due to erroneous pulsar position; (d) growing sine wave due to wrong proper motion. All four examples are based on the PSR J0437$-$4715 data set which will be fully described and analysed in Chapter 3.
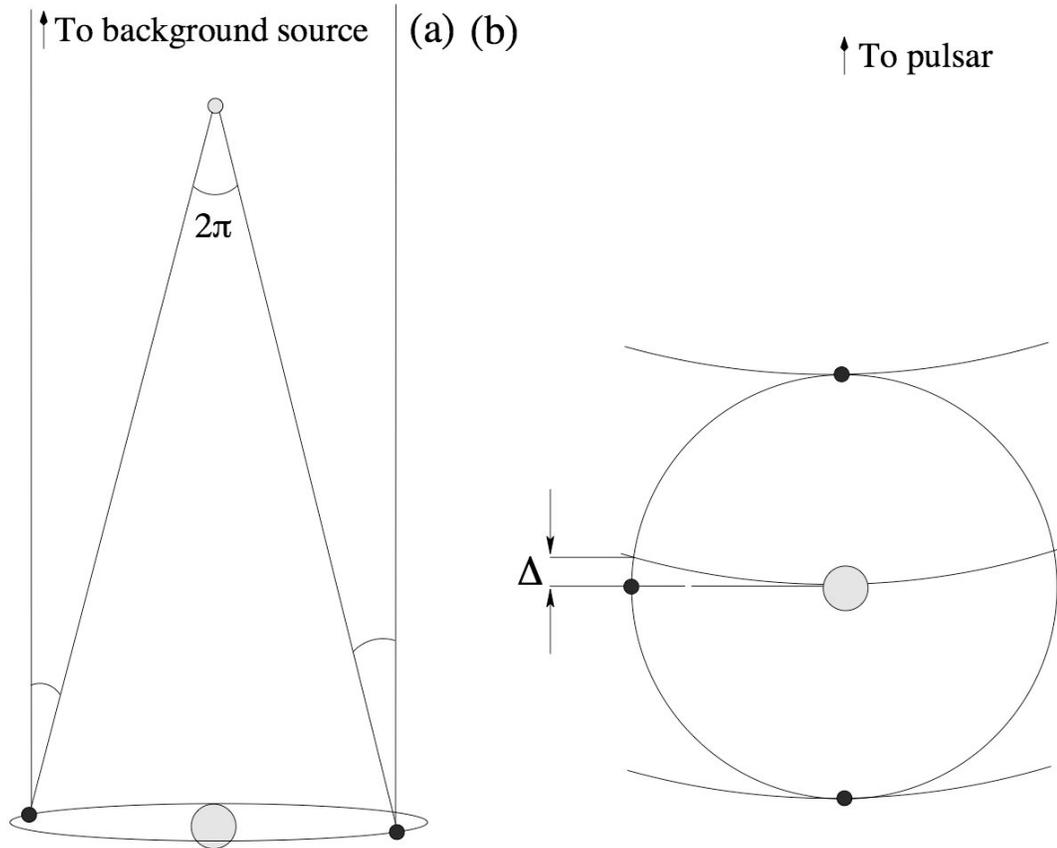
Figure 1.4: (a) Traditionally, distances are calculated based on the yearly change in position of a nearby source with respect to a background source. (b) In pulsar timing, the background source is not observed, but the curvature of the wavefront originating at the pulsar is also inversely proportional to the distance to the pulsar and this curvature can be measured by means of the half-yearly delay Δ indicated in the figure.

where $\parallel$ denotes projections onto the line of sight and $\perp$ projections perpendicular to the line of sight.

Adopting the notation $d = |\vec{d}|$, introducing the proper motion $\vec{\mu} = \vec{v}_\perp$ and translating into a timing delay, we obtain:

$$\Delta_{\mathrm{geom}} = (p - d)/c = \frac{v_r}{c}(t - t_0) + \frac{r_\parallel}{c} + \frac{v_T^2(t - t_0)^2}{2cd} + \frac{\vec{\mu} \cdot \vec{r}_\perp}{cd}(t - t_0) + \frac{r_\perp^2}{2cd} \quad (1.10)$$

The different terms can be distinguished as follows. The first term is a secular increase in distance due to the radial velocity of the pulsar. Since this introduces a linearly time-varying delay, it is indistinguishable from the spin period of the pulsar and can therefore not be individually measured. The second term describes the varying distance between the Earth and the pulsar caused by the orbital motion of the Earth - which brings it closer or further depending on the time of year. This type of delay - the varying light-travel time across an orbit - is called a "Roemer delay"[2]. The third term, which grows quadratically with time, is the Shklovskii effect, first identified by Shklovskii (1970) and is due to the apparent acceleration away from us as the pulsar travels in a straight line tangent to the plane of the sky. This effect is easily derived by considering the distance between the pulsar and Earth (d) and the tangential velocity (v_T), perpendicular to the line of sight. Designating the initial distance d_0, we get the relationship: $d = \sqrt{d_0^2 + v_T^2 t^2}$. Differentiating twice results in $\mathrm{d}^2 d/\mathrm{d}t^2 = d_0^2 v_T^2/\sqrt{(d_0^2 + v_T^2 t^2)^3}$. Approximating $d_0 \approx d = \sqrt{d_0^2 + v_T^2 t^2}$ now results in $\mathrm{d}^2 d/\mathrm{d}t^2 \approx v_T^2/d$ - which is the apparent radial acceleration. The second-last term of Equation 1.10 is the actual proper motion term. It has a yearly signature (as shown by $\vec{r}_\perp$) and the size of the signature grows linearly in time, as described before and shown in Figure 1.3 d. Finally, the delay proportional to $r_\perp^2$, is the timing parallax signature which, due to the square, has a half-yearly signature as shown in Figure 3.3.

The above description of the geometric timing delays ignored some of the more subtle effects, as a careful read of Edwards, Hobbs & Manchester (2006) will show. Most specifically, we have in this analysis ignored several higher order terms, mainly for purposes of clarity. Also the Einstein and aberration delays were ignored. The aberration delay is caused by the relative motion of the pulsar and the observer. The Einstein delay arises because of the general relativistic time dilation experienced in fields with different gravitational strength. Through the motion of the planets in our Solar System, the gravitational strength (and therefore, the relative speed of time) changes as a function of space and time. A full treatment (Irwin & Fukushima 1999) of the integrated effect of these delays on pulsar timing, shows that correction is needed to achieve timing at the precisions we have today.

---

[2]The Roemer delay is named after the Danish astronomer who first used it to measure the speed of light based on the orbits of the Galilean moons.
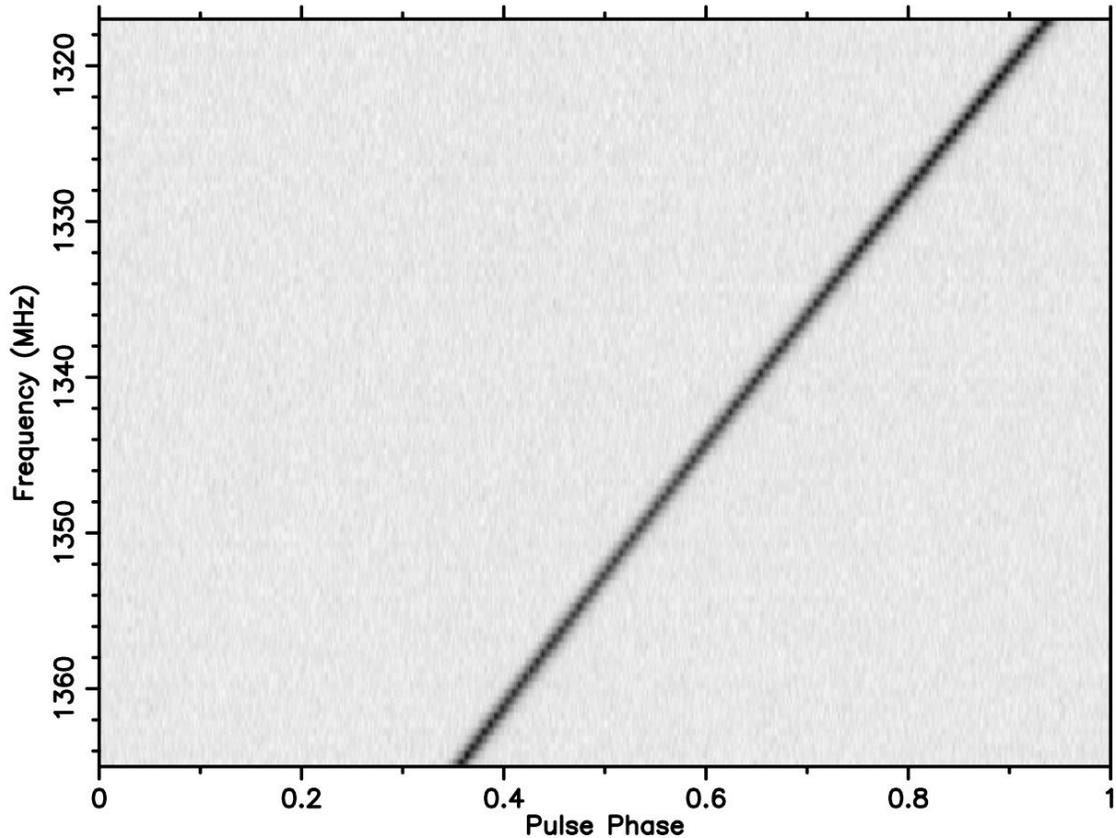
Figure 1.5: Frequency-phase plot of a pulse profile of PSR J1909−3744, uncorrected for interstellar dispersion. The pixellation in y-direction is due to the limited number of frequency channels in the observational setup (see Chapter 2 for more information). While the dispersion delay is dependent on the square of the observing frequency, the low DM and small bandwidth of this observation allow only a very weak quadratic trend to be seen.

1.2.3 Effects of the Interstellar Medium

Ever since the exposition of special relativity (Einstein 1905), it has been understood that the speed of light is constant and independent of the reference frame of the observer. However, this is only true in a vacuum: in all other media, the speed of light is determined by the refractive index n of the medium: $c = c_0/n$ (with c_0 the speed of light in vacuum). Since $n \neq 1$ for the ionised interstellar medium and since n varies strongly with the frequency of the light, the travel time of a given wave changes with observing frequency. In the case of pulsar timing, this effect causes the same pulse to be observed first at higher observational frequencies and later at lower frequencies. This is clearly illustrated in Figure 1.5.

This dispersive effect needs to be remedied at two different points. Firstly, it needs to be countered when integrating over frequency - otherwise the pulse profiles will be dramatically smeared out, which will worsen any achievable timing

precision. Secondly it needs to be corrected in the actual timing, in case observations at different observing frequencies are included in the same data set. Lorimer & Kramer (2005) derive the time delay as a function of observing frequency to be:

$$\Delta_{\text{ISM}} = \frac{D}{f^2} \int_0^d n_{\text{e}} \mathrm{d}l, \tag{1.11}$$

with n_{e} the electron density per cm^3 and the dispersion constant:

$$D = \frac{e^2}{2\pi m_{\text{e}} c} \approx 4.15 \times 10^3 \, \text{MHz}^2 \text{pc}^{-1} \text{cm}^3 \text{s}. \tag{1.12}$$

Notice that the observation of a single pulse across a broad enough bandwidth can be used to calculate the integrated electron density between us and the pulsar. This quantity is called the *dispersion measure*, DM:

$$DM = \int_0^d n_{\text{e}} \mathrm{d}l. \tag{1.13}$$

Given this definition, a measurement of the DM can be combined with a measure of distance (either from timing or VLBI) to provide a precise value for the average electron density towards the pulsar. This in turn provides an input to models of the Galactic electron density, as presented by Cordes & Lazio (2002). Inversely, such models can be used to make first-order estimates of the distance to a pulsar, based on its measured DM.

By means of illustration, Figure 1.5 shows a delay of 0.58 pulse periods between the frequencies of 1317 MHz and 1365 MHz. Given the period of PSR J1909−3744 to be 2.947 ms and rewriting Equation 1.11 to calculate the difference between two bands:

$$t_2 - t_1 = D \times DM \times \left(f_2^{-2} - f_1^{-2} \right), \tag{1.14}$$

we obtain $DM \approx 10.34 \, \text{cm}^{-3} \text{pc}$, which compares well with the catalogue value of $10.3940 \, \text{cm}^{-3} \text{pc}$.

It is important to notice that the electron density is not necessarily constant throughout space. Since the pulsar, the Solar System and the interstellar medium in between are all in motion, the electron density along the line of sight is therefore expected to change as a function of time, which will change the DM, too. The density of ionised particles contained within the Solar wind also varies strongly - especially as the lines of sight for some pulsars travel closely to the Sun at some times during the year. Detailed analyses of both of these effects are presented by You et al. (2007a, 2007b) and Ord, Johnston & Sarkissian (2007). At a much lower level, the ISM also causes scattering and scintillation, as reviewed in, for example, Rickett (1990). While proper mitigation strategies for these effects will become increasingly important in high-precision timing, they are not significant for the work presented in this thesis (see §4.6.3).

1.2.4 Geometric Effects of a Binary System

In standard Newtonian mechanics, the orbit of any body around another can be determined based on the following parameters:

Binary period, P_{b}, measured in days.

Semi-major axis, a, measured in light-seconds.

Orbital eccentricity, e, between 0 (circular) and 1 (parabola).

Inclination angle, i, defined as the angle between the angular momentum vector of the binary orbit and the line of sight. Away from the observer (clockwise rotation) is $0°$, towards the observer (counterclockwise rotation) is $180°$.

Longitude of the ascending node, Ω, measured from North through East, towards the ascending node. The ascending node is the point in the orbit where the pulsar crosses the plane of the sky, moving away from the observer.

Angle of periastron, ω, measured from the ascending node along with the binary rotation.

Time of periastron passage, T_0, given as MJD.

Note that a and i are not generally measured independently, but rather in combination through the projected semi-major axis, $x = a \sin i$.

Given these definitions, we can expand Equation 1.9 to include geometric effects of the binary system. Introducing vector $\vec{b}$ from the barycentre of the binary system (BB) to the pulsar and redefining $\vec{d}$ to point from the SSB to the BB, Equation 1.10 can (to first order) be expanded with the following parameters (as in Edwards, Hobbs & Manchester 2006):

$$\Delta_{\mathrm{Bin}} = \frac{b_{\parallel}}{c} + \frac{1}{cd}\left((t - t_0)\vec{v}_{\perp} \cdot \vec{b}_{\perp} + \vec{r}_{\perp} \cdot \vec{b}_{\perp} + \frac{b_{\perp}^2}{2}\right). \tag{1.15}$$

(Notice various deformations due to general relativity (GR) are also needed in this treatment, as well as derivatives of parameters such as $\omega = \omega_0 + \dot{\omega}(t - t_0)$, for example. For a full relativistic treatment, see Damour & Deruelle (1986) and Edwards, Hobbs & Manchester (2006).

In Equation 1.15, $b_{\parallel}$ is the Roemer delay of the binary system (equivalent to $r_{\parallel}$ in the single pulsar case) and can be expanded in terms of the binary parameters as follows (after Damour & Deruelle 1986):

$$\Delta_{\mathrm{R}} = \frac{b_{\parallel}}{c} = \frac{a \sin i}{c}\left(\sin\omega(\cos u - e) + \sqrt{1 - e^2}\cos\omega\sin u\right), \tag{1.16}$$

with u the eccentric anomaly defined from $n(t - T_0) = u - e \sin u$ (and n an integer).

The second term, $\vec{v}_\perp \cdot \vec{b}_\perp$, demonstrates the effect the proper motion has on the orbital parameters. As the binary system moves across the sky, we observe it from an ever-changing angle, which observationally results in a secular change in the projected semi-major axis x and angle of periastron ω, as first described by Kopeikin (1996). The third term, $\vec{r}_\perp \cdot \vec{b}_\perp$ is a combined effect of the orbital motions of the Earth and pulsar, which causes additional delays of a similar type to those of the timing parallax. This effect, which was first described by Kopeikin (1995) is therefore named the "annual-orbital parallax" (AOP). Both the proper motion effect and the AOP were first measured in the J0437$-$4715 binary system (respectively by Sandhu et al. (1997) and van Straten et al. (2001)). The final term, $b_\perp^2$ is comparable to the earlier $r_\perp^2$ and is effectively the parallax effect due to the binary motion of the pulsar - therefore named "orbital parallax". It was first derived in parallel with the AOP effect by Kopeikin (1995) but has not been measured to date.

From Kopeikin (1996), we can obtain the full expansion of the proper motion effect in terms of the binary parameters:

$$
\begin{aligned}
\Delta_{\text{Bin,PM}} &= \frac{(t - t_0)\vec{\mu} \cdot \vec{b}_\perp}{c} \\
&= \frac{x(1 - e \cos u) \cos(\omega + A_\text{e})}{\sin i}(\mu_\alpha \cos \Omega + \mu_\delta \sin \Omega) \\
&\quad + x \cot i (1 - e \cos u) \sin(\omega + A_\text{e})(-\mu_\alpha \sin \Omega + \mu_\delta \cos \Omega), \quad (1.17)
\end{aligned}
$$

where the true anomaly, A_e, is defined as:

$$
A_\text{e} = 2 \arctan\left(\sqrt{\frac{1+e}{1-e}} \tan \frac{u}{2} \right)
$$

Likewise, the AOP effect can be written out as follows, from Kopeikin (1995):

$$
\Delta_{\text{Bin,AOP}} = \frac{\vec{r}_\perp \cdot \vec{b}_\perp}{cd} = \frac{x}{d} \Bigg[(\Delta_{I_0} \sin \Omega - \delta_{J_0} \cos \Omega) R \cot i
$$
$$
- (\Delta_{I_0} \cos \Omega + \Delta_{J_0} \sin \Omega) Q \csc i \Bigg], \quad (1.18)
$$

with $\Delta_{I_0} = -\vec{r} \cdot \vec{I}_0$ and $\Delta_{J_0} = -\vec{r} \cdot \vec{J}_0$ the X and Y components of the Sun-Earth vector on the plane of the sky. ($\vec{I}_0$ and $\vec{J}_0$ are unit vectors connected to the BB and pointing North and East respectively.) R and Q are functions defined as follows:

$$
R = \sin \omega (\cos u - e) + \sqrt{1 - e^2} \cos \omega \sin u \quad (1.19)
$$
$$
Q = \cos \omega (\cos u - e) - \sqrt{1 - e^2} \sin \omega \sin u. \quad (1.20)
$$

The important point to note about these terms, is their dependence on the orbital inclination, i, and the longitude of the ascending node, Ω. Without these so-called "Kopeikin terms", the measurement of Ω would be impossible. In the next

section we will show that i can be measured due to general relativistic effects, so the independent determination of the inclination angle through the Kopeikin terms provides a test of these general relativistic predictions - as described in van Straten et al. (2001). Alternatively, the GR and Kopeikin effects can be combined to provide a more precise measurement - this approach will be used in Chapter 3.

1.2.5 Relativistic Effects in Binary Systems

The timing formulae described in the preceding sections have ignored any effects due to general relativity (GR). Now, we will highlight the most important general relativistic additions to that timing model. While the focus will be on the binary system of the pulsar, it must be noted that these effects play in the Solar System as well, albeit at a lower level.

One of the problems of Keplerian dynamics that was solved by the introduction of GR, was the perihelion advance of Mercury. This same effect has been readily observed in several binary pulsar systems and is predicted to be (as in Taylor & Weisberg 1982):

$$
\begin{aligned}
\dot{\omega} &= 3 \left(\frac{2\pi}{P_{\rm b}} \right)^{5/3} \left(\frac{GM}{c^3} \right)^{2/3} \frac{1}{1 - e^2} \\
&\approx 0.19738 \left(\frac{M}{M_\odot} \right)^{2/3} \left(\frac{P_{\rm b}}{1\,{\rm day}} \right)^{-5/3} \frac{1}{1 - e^2},
\end{aligned}
\tag{1.21}
$$

with $M = M_{\rm psr} + M_{\rm c}$ the total system mass, $M_\odot$ the mass of the Sun and $\dot{\omega}$ in units of degrees per year.

The next two post-Keplerian parameters are measured through what is now known as the *Shapiro Delay*, after the scientist who first proposed this test of GR (Shapiro 1964). The effect in question is the time delay introduced by a gravitational potential along the line of sight. While Shapiro originally envisaged this test to take place in the Solar System through transmission of radio waves past the edge of the Sun, it can be readily observed in binary pulsar systems that have a nearly edge-on orbit ($i \approx 90°$). Clearly, the amplitude of the effect (the *range*, r) is dependent on the companion mass, while its evolution as a function of binary phase (the *shape*, s) is determined by how closely the rays pass by the companion star - and therefore depends on the inclination angle of the system. More precisely, the two relativistic parameters are predicted to be (see, e.g. Stairs 2003):

$$
r = \frac{GM_2}{c^3} = 4.9255 \times 10^{-6} s \left(\frac{M_{\rm c}}{M_\odot} \right)
\tag{1.22}
$$

$$
\begin{aligned}
s &= \frac{cxG^{-1/3}}{M_{\rm c}} \left(\frac{2\pi M}{P_{\rm b}} \right)^{2/3} \\
&= 0.1024 \left(\frac{P_{\rm b}}{1\,{\rm day}} \right)^{-2/3} \left(\frac{M}{M_\odot} \right)^{2/3} \left(\frac{M_{\rm c}}{M_\odot} \right)^{-1} \left(\frac{a \sin i}{c} \right)
\end{aligned}
\tag{1.23}
$$

and in GR, $s = \sin i$.

The fourth relativistic effect is the orbital decay due to gravitational wave emission. First measured in the original binary pulsar system PSR B1913+16 (Taylor & Weisberg 1982), this parameter has provided the first indirect detection of gravitational waves. The predicted size of this effect is, as presented by Taylor & Weisberg (1982):

$$
\begin{aligned}
\dot{P}_{\mathrm{b}} &= -\frac{192\pi}{5c^5}\left(\frac{2\pi G}{P_{\mathrm{b}}}\right)^{5/3}\frac{1+\frac{73}{24}e^2+\frac{37}{96}e^4}{(1-e^2)^{7/2}}\frac{M_{\mathrm{psr}}M_{\mathrm{c}}}{M^{1/3}} \\
&= -2.1719\times 10^{-14}\frac{1+\frac{73}{24}e^2+\frac{37}{96}e^4}{(1-e^2)^{7/2}}\left(\frac{P_{\mathrm{b}}}{1\mathrm{day}}\right)^{-5/3}\left(\frac{M_{\mathrm{psr}}M_{\mathrm{c}}}{M_\odot^2}\right)\left(\frac{M}{M_\odot}\right)^{-1/3}(1.24)
\end{aligned}
$$

(where $\dot{P}_{\mathrm{b}}$ is unitless). Notice, however, that this is not the only contribution to the observed orbital period derivative. As will be explained in more detail in §3.4, the Shklovskii effect discussed earlier, as well as some accelerations caused by the mass distribution in the Galaxy, both influence the effective value of $\dot{P}_{\mathrm{b}}$.

The fifth and final relativistic effect that can be measured through pulsar timing, is the transverse doppler and gravitational redshift parameter, γ. It is caused by the fact that the progress of time is strongly affected by the strength of the gravitational potential. As a pulsar in an eccentric orbit moves closer or further away from its companion star, the gravitational potential varies and, consequentially, so does the clock rate. The theoretical prediction for this parameter is (from Taylor & Weisberg 1982):

$$
\begin{aligned}
\gamma &= \frac{G^{2/3}e}{c^2}\left(\frac{P_{\mathrm{b}}}{2\pi}\right)^{1/3}\frac{M_{\mathrm{c}}(M+M_{\mathrm{c}})}{M^{4/3}} \\
&= 6.926\times 10^{-3}s\left(\frac{P_{\mathrm{b}}}{1\mathrm{day}}\right)^{1/3}e\frac{M_{\mathrm{c}}(M+M_{\mathrm{c}})}{M_\odot^2}\left(\frac{M}{M_\odot}\right)^{-4/3} \qquad (1.25)
\end{aligned}
$$

One point of note is that all of the relativistic effects presented here (equations 1.21 through to 1.25) are only dependent on the Keplerian parameters presented in the previous section and the masses of the binary system: M_{psr} and M_{c}. This implies that, as soon as two GR effects are measured in addition to the Keplerian parameters, the magnitude of all other effects can be predicted. The overdetermined character of these equations has allowed the most stringent tests of GR to date (Kramer et al. 2006b).

1.3   Gravitational Waves and Pulsar Timing Arrays

The interaction of the gravitational force with matter is described by the Einstein field equations which are, like Maxwell's equations for the electromagnetic force,

wave equations (see, e.g. Schutz 1993). The concept that acceleration of masses creates a gravitational wave (GW) like the acceleration of electric charge generates an electromagnetic wave, was one of the main relativistic predictions that remained untested for more than half a century. As mentioned in the previous section, Taylor & Weisberg (1982) finally proved the veracity of this prediction by accurately demonstrating that the energy loss from the binary pulsar system B1913+16 equated the predicted energy loss due to gravitational wave emission. Until today, however, no direct detection of gravitational waves has been made so all characteristics of these waves (such as, for example, polarisation and velocity) remain untested.

In this section, the case for direct detection of GWs through pulsar timing will be outlined. First some initial experiments and concepts will be described in §1.3.1. Next, §1.3.2 will discuss the recent history of limits on the gravitational wave background (GWB). In §1.3.3 we will outline the potential sources of GWs that might be detected by pulsar timing arrays (PTAs) and §1.3.4 will provide predictions for GW sensitivity of those PTAs.

1.3.1 Initial Pulsar - GW Experiments

In §1.2.5, we saw that the gravitational field of a companion star delays pulsar radiation when it passes close to the star. When GWs travel past the line of sight, the changing gravitational potential this entails has a similar effect, even though the details differ. This idea was first explored by Sazhin (1978), who analysed the effect GWs from stellar binaries would have on timing, if the binary was situated close to the line of sight between the pulsar and the Earth. His work showed that a close enough alignment is rather unlikely and that, even if such an alignment existed, it could prove impossible to distinguish the GW-induced sinusoid from a planet orbiting the pulsar, since the effect would only be seen in a single pulsar. However, the potential to detect the influence of GWs from a supermassive black hole (SMBH) binary system, proved more promising. Because of the extreme gravitational character of these systems, their effect is predicted to be significant over cosmological distances - which implies it would affect the timing of all pulsars, not just one. This idea was further explored by Detweiler (1979) who first used pulsar timing residuals to place a limit on the energy density of a stochastic background of such cosmological GW sources. A few years later, Hellings & Downs (1983) first used the fact that the effect of this gravitational wave background (GWB) must be correlated between different pulsars. To understand why, considering a single gravitational wave is a helpful stepping stone. As with electromagnetic waves, gravitational waves act perpendicularly to their direction of propagation. However, unlike electromagnetic waves, they have a quadrupolar signature. This means that, perpendicular to the GW's direction of travel, pulsars in opposite parts of the sky undergo identical effects (positive correlation) and pulsars offset by 90° undergo opposed effects (negative correlation), while there is no impact on pulsars along the direction of propagation. This quadrupolar effect - as shown in Figure 1.6 - turns out to be characteristic for a gravitational
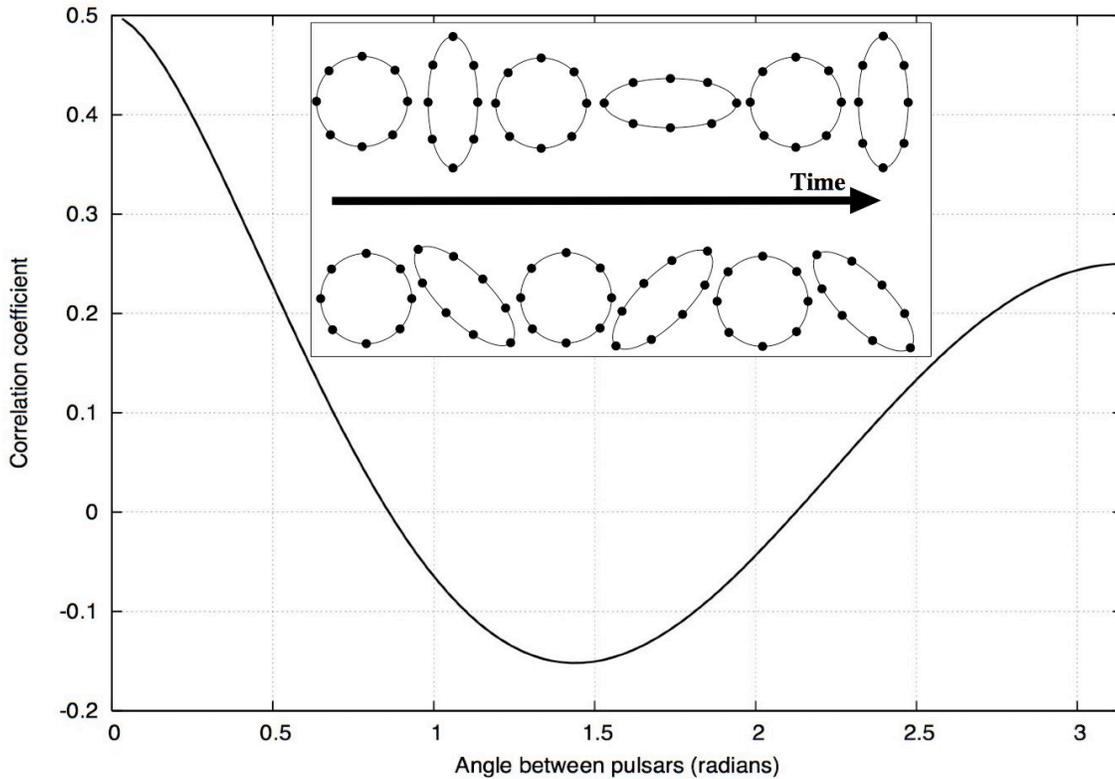
Figure 1.6: Hellings & Downs curve as a function of angular separation between pulsars. Notice the correlation only rises up to 0.5. This is because the GW effect on the Earth is correlated between pulsars, but the equally large effect on the pulsar itself is uncorrelated. The inset shows the effect of a gravitational wave on a ring of test particles. The direction of propagation of the wave is perpendicular to the page and the images show the evolution as a function of time, progressing horizontally. Top row: +-polarised GW; bottom row: ×-polarised GW.

wave background (GWB) as well, as demonstrated by Hellings & Downs (1983). Mathematically, it is described as follows (as given by Jenet et al. 2005):

$$\zeta(\theta) = \frac{3}{2} x \log x - \frac{x}{4} + \frac{1}{2} \tag{1.26}$$

with $x = 0.5\,(1 - \cos\theta)$ and θ the angular separation of the pulsars on the sky. This expected correlation as a function of angle between the pulsars is commonly referred to as the "Hellings & Downs curve".

With the first MSP discovered in 1982, by the end of the 1980s the superior timing stability of these more rapidly rotating neutron stars was acknowledged and the concept of a pulsar timing array (PTA) was proposed (in short succession by Romani 1989 and Foster & Backer 1990). The fundamental idea behind a PTA is to time a group of highly stable MSPs and analyse the correlations between their timing residuals in order to optimise sensitivity to several corrupting effects. Three sources of correlations are expected to exist in the timing residuals of MSPs. The first source consists of errors in the observatory clocks. This would affect all pulsars in the same way at the same time: the correlation coefficient will be positive and equal for all pulsar pairs - this is a monopole correlation. The second source of correlations are inaccuracies in the SSE. At any point in time, an error in the SSE will correspond to an artificial offset in the calculation of the SSB. This will imply that pulses from pulsars in the direction of the artificial offset will be seen to arrive late; pulsars in the opposing hemisphere will be considered early and pulsars at right angles with the offset will be unperturbed. This correlation signature is therefore a dipole defined by the error in the SSE. Finally, correlations due to a GWB would induce correlations as outlined in the previous paragraph and shown in Figure 1.6. This effect is quadrupolar and therefore fundamentally different - and easily distinguishable - from both clock errors and errors in the SSE.

1.3.2 Limits on the Power in the GWB

In the decade that followed the proposal to construct timing arrays, most efforts focussed on using pulsar timing to limit the potential power in the GWB. The main reason for this was that too few stable pulsars to attempt a detection were known. Following the summary of Jenet et al. (2006), the spectral power induced by a GWB in pulsar timing residuals, is:

$$P(f) = \frac{h_c(f)^2}{12\pi^2 f^3} = \frac{A^2}{12\pi^2} \frac{f^{2\alpha-3}}{f_0^{2\alpha}}, \tag{1.27}$$

where $h_c(f)$ is the characteristic strain spectrum, defined through:

$$h_c(f) = A \left(\frac{f}{f_0}\right)^\alpha \tag{1.28}$$

with A the amplitude of the GWB, f the frequency in units of yr^{-1} and $f_0 = 1\,\mathrm{yr}^{-1}$. α is the spectral index of the GWB, which depends on the type of GWB considered, as detailed in §1.3.3. Since $\alpha < 0$ for all predicted backgrounds (see §1.3.3), the spectral index of the effect on the residuals is highly negative and therefore strongly dominated by low frequencies - implying a strong correlation between GWB sensitivity and data span. Note the effect on the timing residuals is not only dependent on the GWB amplitude A, but also on the spectral index of the GWB, α. This implies that any limit on A derived from pulsar timing residuals will have to specify the spectral index under consideration as well, resulting in different limits on A for different GWBs, as will follow.

The first limit on the strength of the GWB derived from MSP timing, was presented by Stinebring et al. (1990), who used seven years of Arecibo data on PSRs J1939+2134 and J1857+0943[3] and assumed a spectral index $\alpha = -1$. At 95% confidence, they limited the energy density of the GWB per unit logarithmic frequency interval to $\Omega_{\mathrm{g}}h^2 < 4 \times 10^{-7}$. This can be converted into the amplitude used above, through Equation 3 of Jenet et al. (2006):

$$\Omega_{\mathrm{gw}}(f) = \frac{2}{3}\frac{\pi^2}{H_0^2}f^2 h_{\mathrm{c}}(f)^2 \qquad (1.29)$$

and hence:

$$\Omega_{\mathrm{gw}}(f)h^2 = \frac{2\pi^2}{3 \times 10^4}\left(\frac{F_1}{F_2}\right)^2 \frac{f^{2\alpha+2}}{f_0^{2\alpha}}A^2, \qquad (1.30)$$

where we defined the Hubble constant as $H_0 = 100h\,\mathrm{km/s/Mpc}$ and introduced the normalisation factors $F_1 = 3.0856 \times 10^{19}\,\mathrm{km/Mpc}$ and $F_2 = 3.15576 \times 10^7\,\mathrm{s/yr}$ to convert units properly. Numerically, this approximates as:

$$\Omega_{\mathrm{gw}}(f)h^2 \approx 6.29 \times 10^{20} A^2 f^{2\alpha+2}. \qquad (1.31)$$

The limit of $\Omega_{\mathrm{g}}h^2 < 4 \times 10^{-7}$ for $\alpha = -1$ can therefore be converted to $A < 3 \times 10^{-14}$.

The analysis performed by Stinebring et al. (1990) was based on a type of power spectrum constructed from Gram-Schmidt orthonormal polynomials that were fitted to increasingly short subsets of the timing residuals to provide a measure of power at increasingly high frequencies. While these "Gram-Schmidt spectra" are very powerful tools for investigations of very steep power spectra (Deeter & Boynton 1982; Deeter 1984), their translation into traditional power spectra and Fourier transforms is unclear and the interpretation of any feature of these spectra is therefore difficult. They can, however, be used to determine limits by comparing the power levels obtained from actual data to levels calculated for a supposed GWB amplitude.

This analysis, which was reproduced with longer data sets by Kaspi, Taylor & Ryba (1994) and Lommen (2002), was fundamentally sound, though the final

---

[3]The original names for these pulsars are PSRs B1937+21 and B1855+09. Throughout this thesis the more recent J2000 names are used.

calculation of certainty levels was flawed with the potential to obtain probabilities in excess of unity, as pointed out by Thorsett & Dewey (1996). These last authors proposed an alternative approach to the problem and applied the Neyman-Pearson statistical test, resulting in a 95% confidence limit of $\Omega_g h^2 < 1.0 \times 10^{-8}$ (equivalent to $A < 4 \times 10^{-15}$). Their approach compares the likelihood of a "zero hypothesis", H_0, which states that all timing residuals are purely due to statistically white noise (i.e. radiometer noise) to the likelihood of an alternative hypothesis, H_1, which states the timing residuals are a combination of white noise and GWB. This analysis was invalidated in turn by McHugh et al. (1996), who pointed out it didn't properly account for errors of the first and second kinds, which quantify the probabilities of incorrect assessment of hypotheses. McHugh et al. (1996) subsequently proposed a Bayesian approach, which resulted in the weaker limit of $\Omega_g h^2 < 9.3 \times 10^{-8}$ at 95% confidence ($A < 1 \times 10^{-14}$).

More recently, Jenet et al. (2006) developed a Monte-Carlo based method of limiting the GWB amplitude. Their method uses newly developed software that enables simulation of GWB effects on timing residuals in a way that allows a direct comparison of real data with GW-affected, simulated, data (Hobbs et al. 2009). This has the advantage of allowing a more rigorous statistical analysis, though the Jenet et al. (2006) method implicitly requires the pulsar timing data to be 100% statistically white, which is a problematic requirement, especially for data sets with long time spans. Notwithstanding this restriction, they obtained the most stringent limits to date: $\Omega_g h^2 < 2.0 \times 10^{-8}$ (or $A < 6 \times 10^{-15}$) at 95% confidence for a background with $\alpha = -1$ and $A < 1.1 \times 10^{-14}$ at 95% confidence for a background with $\alpha = -2/3$. (Note the limit on $\Omega_g h^2$ is dependent on the gravitational wave frequency, as shown in Equation 1.31. So unless $\alpha = -1$, one should always specify the GW frequency connected to the $\Omega_g h^2$ limit. For ease of use we provide limits on A instead, except when quoting from literature. These limits can easily be converted using Equation 1.31.) Based on the same simulation software, van Haasteren et al. (2008) have proposed a Bayesian technique to both detect and limit the GWB in PTA data sets, but this technique has not yet been applied to actual data.

1.3.3   PTA-detectable GW sources

There is a large variety of sources to which pulsar timing arrays could be sensitive, including both single sources and backgrounds. Single sources, such as binary SMBHs, are possibly non-existent in the Milky Way. Lommen & Backer (2001) analysed the effect of a potential black hole binary with total mass $5 \times 10^6 \, \mathrm{M_\odot}$ in the centre of the Milky Way. They concluded that the induced timing residuals would be at or below the $10 \, \mathrm{ns}$ level - which is far below current timing sensitivity. In the case of gravitational wave *backgrounds* (GWBs), however, stronger signals might be expected.

As shown in the overview by Maggiore (2000), there are several predicted origins for GWBs that would be detectable through PTA research. The most important one

of these is a background of binary SMBHs in the relatively nearby (redshift $z \approx$ 1-2) Universe. Based on the premise of hierarchical galaxy formation, simulations such as those of Rajagopal & Romani (1995), Jaffe & Backer (2003), Wyithe & Loeb (2003) and Enoki et al. (2004), have shown that as galaxies merge, the black holes at their centres initially become a binary pair and eventually merge. This would give rise to both SMBHs and a large number of black hole (and SMBH) binaries and mergers - which generate gravitational waves as they spiral in as well as during and after the merging event. The ensemble of a large number of these creates a background with a spectral index of $-2/3$ and amplitudes predicted to lie between 10^{-15} and 10^{-14}. As a point of comparison, the most stringent limit from pulsar timing to date places a bound on this background of $A \leq 1.1 \times 10^{-14}$ (Jenet et al. 2006).

There are, however, some potential problems with these models. Firstly, it is unclear whether there is sufficient orbital momentum loss for the SMBH binary to merge within a Hubble time. At the initial stages the black holes are surrounded by accretion disks which cause orbital energy loss through friction and AGN activity. However, it is possible that all the stellar material and dust surrounding the black holes will be discarded long before a merger event. This would leave gravitational radiation as the only means to lose energy, but this radiation is far less powerful than that generated in a merger event and it releases too little energy to cause a collapse within a Hubble time. Another major issue lies in simplifications within the models and large uncertainties in input parameters to the simulations. A recent analysis by Sesana, Vecchio & Colacino (2008) shows that the spectral index of $\alpha = -2/3$ strongly depends on the merging history of galaxies and is probably underestimated. Furthermore, they demonstrate (as did Rajagopal & Romani 1995) that at higher frequencies, the GWB would be dominated by a few bright sources at smaller distance. While this means that the results of the simulations - and the predictions following from them - are far less secure than one would hope for, it also provides additional value to a potential detection, as this will uncover significant (and currently inaccessible) information about galaxy formation history.

A second potential GWB in the PTA sensitivity range originates from cosmic strings (Caldwell, Battye & Shellard 1996; Damour & Vilenkin 2005). The background generated by these would have a steeper power spectrum (spectral index $\alpha = -7/6$) than the GWB from SMBH mergers and is therefore more easily detectable over longer lengths of time. The main problems with these backgrounds are the very limited knowledge of input parameters to the models and the potential non-existence of the cosmic strings altogether. Currently predicted amplitudes for this background lie between 10^{-16} and 10^{-14}, but current limits already place a bound at 3.9×10^{-15} (Jenet et al. 2006).

The third potential background is the gravitational wave equivalent to the cosmic microwave background: it is composed of gravitational waves created in the Big Bang (Grishchuk 2005; Boyle & Buonanno 2008). Spectrally speaking this background lies between the previous two, with a spectral index expected around -0.8 or -1.0. The amplitudes predicted by Grishchuk (2005) for this background are between 10^{-17}

and 10^{-15}, making it the weakest of the three backgrounds and therefore the least likely one to be detected any time soon. Other authors (such as Boyle & Buonanno 2008) predict even lower amplitudes for this GWB.

Given the amplitudes, spectral indices and caveats concerning the backgrounds discussed above, the remainder of this thesis will focus on the GWB due to SMBH coalescence, assuming for ease of use a spectral index of $\alpha = -2/3$ and amplitude range of $10^{-15} - 10^{-14}$. We notice that the analysis by Sesana, Vecchio & Colacino (2008) warrants a more complex analysis in order to make detailed assessment of actual detection or exclusion of astrophysical models based on limits, but given the large uncertainties in any of these models, we take these values to provide a decent first order approximation.

1.3.4   Pulsar Timing Arrays

With the large number of pulsar discoveries in surveys after 1990 (Manchester et al. 1996; Camilo et al. 1996; Edwards et al. 2001; Manchester et al. 2001), the feasibility of PTA-type projects has improved, inspiring a new assessment of the PTA concept by Jenet et al. (2005). They presented for the first time a thorough analysis of the timing precision required for detection of a GWB. In the case of a homogeneous timing array (i.e. a timing array in which every pulsar has an identical timing residual RMS), they derived the following sensitivity curve:

$$S = \sqrt{\frac{M\left(M-1\right)/2}{1 + \left[\chi\left(1 + \bar{\zeta}^2\right) + 2\left(\sigma_{\mathrm{n}}/\sigma_{\mathrm{g}}\right)^2 + \left(\sigma_{\mathrm{n}}/\sigma_{\mathrm{g}}\right)^4\right]/\left(N\sigma_\zeta^2\right)}}, \qquad (1.32)$$

where M is the number of pulsars in the PTA, N is the number of observations for each of these pulsars, ζ is the Hellings & Downs correlation between two pulsars, σ_{n} is the RMS of the non-GW noise, σ_{g} is the residual RMS caused by the GWB and

$$\chi = \frac{1}{N\sigma_{\mathrm{g}}^4}\sum_{i=0}^{N-1}\sum_{j=0}^{N-1}c_{\mathrm{ij}}^2$$

with c the GW-induced correlation between the pulsar residuals. One consequence of Equation 1.32 is that the sensitivity saturates: for very strong GWBs, $\sigma_{\mathrm{g}} \gg \sigma_{\mathrm{n}}$ and therefore the equation reduces to $S \approx 0.16\sqrt{M\left(M-1\right)}$, only dependent on the number of pulsars. However, as also described by Jenet et al. (2005), prewhitening schemes could reduce this self-noise and assure increased sensitivity to well beyond this threshold.

Another way of rewriting Equation 1.32 is to evaluate the GWB amplitude at which such saturation becomes significant - effectively the lowest amplitude to which the PTA is sensitive. This amplitude is approached as $N\sigma_{\mathrm{g}}^2$ becomes much larger than σ_{n}^2. Using $13\sigma_{\mathrm{n}}^2 = N\sigma_{\mathrm{g}}^2$ as a threshold (the factor of 13 was derived to achieve

the 3σ detection level in the case of a timing array with 20 pulsars) and using Equation 8 from Jenet et al. (2005):

$$N\sigma_{\mathrm{g}}^2 = \frac{NA^2}{12\pi^2\left(2-2\alpha\right)}\frac{\left(f_{\mathrm{l}}^{2\alpha-2} - f_{\mathrm{h}}^{2\alpha-2}\right)}{f_0^{2\alpha}} \tag{1.33}$$

where A is the amplitude of the GWB, α the spectral index of the GWB, f_{l} is the lowest spectral frequency the pulsar data set is sensitive to and f_{h} is the high-frequency cutoff. (Notice the factor of 12 based on the more recent definition of A as given in Jenet et al. 2006). Following Jenet et al. (2005), we use $f_{\mathrm{l}} = T^{-1}$ and $f_{\mathrm{h}} = 4T^{-1}$ where T is the length of the data set. Rewriting Equation 1.32, we derive the lowest amplitude at which a 3σ detection can be made (for an array with 20 MSPs):

$$A_{\mathrm{S}=3} \approx 2.3 \times 10^{-12}\frac{\sigma_{\mathrm{n}}}{T^{5/3}\sqrt{N}} \tag{1.34}$$

for a background with spectral index $\alpha = -2/3$ (see §1.3.3). Notice the units for Equation 1.34 are μs for σ_{n} and years for T. This relation determines the fundamental trade-off any PTA will be determined by, showing the strong dependence on the length of the observational campaign, T, as well as on the timing precision, σ_{n}. As a baseline scenario for future PTA efforts, Jenet et al. (2005) proposed a PTA based on weekly observations of 20 MSPs, timed at 100 ns residual RMS for 5 years (i.e. $N = 250$, $M = 20$, $\sigma_{\mathrm{n}} = 0.1\,\mu$s, $T = 5\,$years). Such an array would be sensitive at the 3σ level to backgrounds with amplitudes larger than 10^{-15} (see §1.3.3).

1.4   Thesis Structure

The remainder of this thesis is structured as follows. In Chapter 2, the hardware used in our observations will be described, along with some fundamentals of radio astronomy required for this description. As the baseline scenario for PTAs presented above shows, pulsar timing needs to achieve high levels of timing precision ($\sim 100\,$ns) and maintain this timing precision over many years ($T > 5\,$yrs). Chapters 3 and 4 address these requirements. Specifically, Chapter 3 presents the highest-precision pulsar timing data set that has a time span of a decade. Such data sets enable several interesting investigations into the pulsar astrometric and binary parameters, which are also presented. Chapter 4 contains the first large sample of MSPs to be timed over substantial timescales (12 yrs on average) and presents an analysis of MSP stability and the predictions for PTA sensitivity following from that. The sensitivity analysis we use goes beyond the simple homogeneous PTA presented in §1.3.4 and uses the analysis presented in Appendix A. Having presented some of the longest MSP timing data sets at high timing precision, Chapter 5 presents a straightforward method of limiting the strength of the GWB based on these data sets and derives a new limit on that background, from our data. The results are interpreted and summarised in Chapter 6. The various abbreviations and symbols used throughout this thesis are listed for easy reference in Appendix B.

Chapter 2

Radio Astronomy Fundamentals and Observing Hardware

It is a riddle wrapped in a mystery inside an enigma
Winston Churchill, 1939

2.1 Abstract

In this chapter a brief overview is given of the hardware with which the data analysed in subsequent chapters were acquired. Since this thesis reports on ten years of pulsar timing, the variety of backends is large and almost provides a full overview of historic pulsar timing observing systems. Given the increasing complexity of these systems over the years, we have chosen to adopt a chronological approach in our discussion (Section 2.3), describing the oldest backends - the analogue filterbanks - first in §2.3.2, followed by the autocorrelation spectrometers in §2.3.3 and, finally, the coherent dedispersion baseband systems in §2.3.4. The actual instruments used, are listed in §2.3.5. First, some fundamental principles of radio astronomy will be outlined in Section 2.2.

2.2 Fundamentals of Radio Astronomy

2.2.1 Blackbody Radiation and Brightness Temperature

Macroscopic bodies of finite temperature emit radiation. In most cases, the spectrum of this radiation is reasonably well approximated by that of blackbody radiation. A blackbody is a hypothetical object with perfect absorption and emission properties.

29
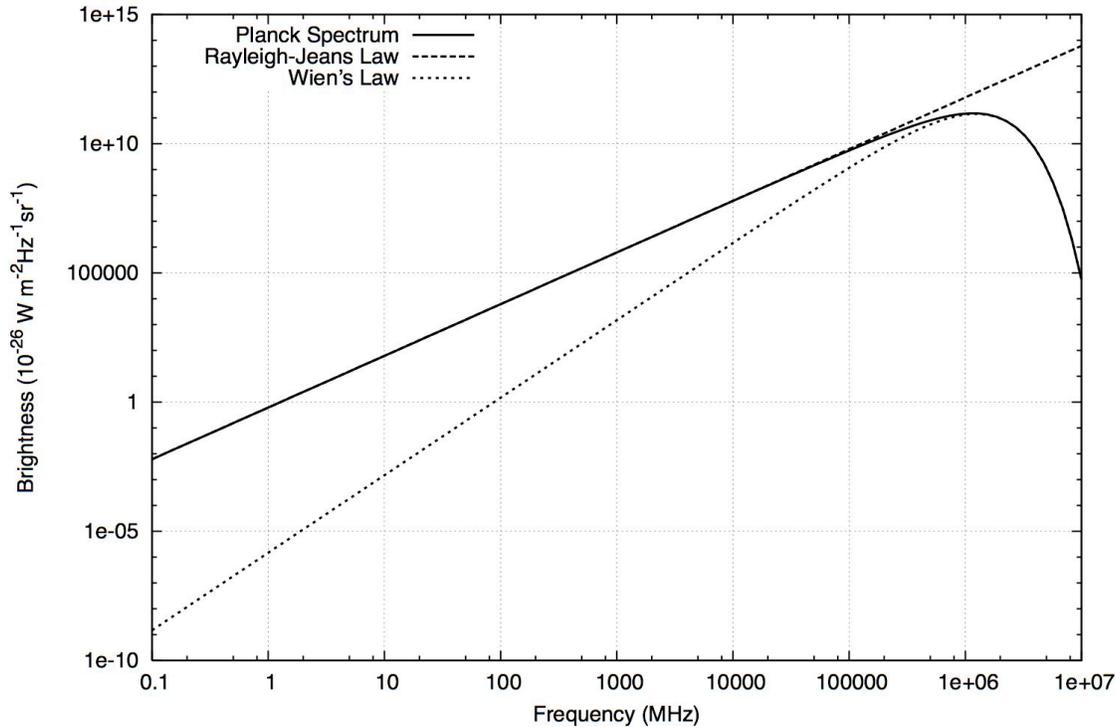
Figure 2.1: Planck spectrum for a blackbody at 20 K (full line). Also shown are the Rayleigh-Jeans approximation (dashed line) and Wien's law (dotted line), demonstrating the different regimes in which these laws approximate the Planck spectrum.

The spectrum of its heat-induced emission is defined by Planck's law:

$$B(\nu, T) = \frac{2h\nu^3}{c^2} \frac{1}{e^{h\nu/kT} - 1}, \tag{2.1}$$

with B the brightness in W m^{-2} Hz^{-1} sr^{-1}, ν the frequency of the emission, T the temperature of the body, h Planck's constant, c the speed of light and k Boltzmann's constant. Figure 2.1 shows the Planck spectrum for a blackbody of temperature 20 K, along with two approximations. The first one of these is the Rayleigh-Jeans law, which approximates a Planck spectrum at the low frequency end:

$$B(\nu, T) = \frac{2\nu^2}{c^2} kT. \tag{2.2}$$

The second approximation, Wien's law, approximates at the high-frequency end:

$$B(\nu, T) = \frac{2h\nu^3}{c^2} e^{-h\nu/kT}. \tag{2.3}$$

From Figure 2.1, it is quite clear that, at radio frequencies, the Rayleigh-Jeans law is a simple but precise approximation that can easily be used, at least for the 20 K body shown in the Figure. Equation 2.1 shows that the peak of a blackbody

spectrum increases to higher frequencies as the temperature of the body increases. More precisely, Wien's displacement law predicts the peak frequency to be:

$$\frac{\nu_{\max}}{\text{GHz}} = 48.8 \frac{T}{\text{K}} \tag{2.4}$$

(after Rohlfs & Wilson 2000). This implies that the Rayleigh-Jeans law will be a useful approximation for all practical radio astronomy purposes.

Based on these formulae, it is possible to prove that pulsar radiation is not thermal in character. Consider the Crab pulsar, B0531+21, as an example. Its average flux is $14\,\text{mJy}$ ($= 14 \times 10^{-29}\,\text{W m}^{-2}\text{Hz}^{-1}$) at an observing frequency of $1.4\,\text{GHz}$ (Lorimer et al. 1995b). Also, based on its DM of $56.791\,\text{cm}^{-3}\text{pc}$ (Counselman & Rankin 1971), its distance is estimated to be $2.49\,\text{kpc}$ (as described in §1.2.3, based on the Galactic ISM model of Taylor & Cordes 1993). Assuming an emission region of $10\,\text{km}$ radius, the solid angle of this emission would be: $\pi(10\,\text{km}/2490\,\text{pc})^2 = 5.3 \times 10^{-32}\,\text{sr}$ and the pulsar therefore has a brightness of $2.6 \times 10^3\,\text{W m}^{-2}\text{Hz}^{-1}\text{sr}^{-1}$. Inserting this into Equation 2.2 results in a blackbody temperature of $T_{\text{b}} = 4 \times 10^{24}\,\text{K}$. Given Equation 2.4, such a brightness temperature would be expected to have the peak of its emission at frequencies around $20 \times 10^{25}\,\text{GHz}$, which is well beyond the gamma ray part of the spectrum. If pulsar emission were thermal in origin, therefore, it should be easily visible across all bands[1]. This argument is taken one step further by Manchester & Taylor (1977), in relating the particle energy required for incoherent radiation. In the case of thermal emission, the required energy of the particles involved is bounded as $kT_{\text{b}} < \epsilon$, with k the Boltzmann constant and T_{b} the brightness temperature. This would imply particle energies of $\epsilon > 3.4 \times 10^{20}\text{eV}$. Such high particle energies cannot be produced by any known processes and as a consequence coherent emission must lie at the basis of the pulsar emission at radio wavelengths. Finally, as seen in Figure 2.1, the spectral index of thermal radiation at radio wavelengths would be expected to be positive. For pulsars the spectral index is generally negative (Lorimer et al. 1995b).

2.2.2 Noise and Amplification in the Signal Chain

A simple consequence of the theory of blackbody radiation is that all systems in the signal chain radiate energy and hence contribute to the noise in the signal. Now consider a system chain with N elements, each with noise temperature T_{i} and gain G_{i} ($G > 1$ for amplifiers, $G < 1$ for all other elements). The input power or astronomical signal is: $P_0 = kT_{\text{A}}$. After the first element, the power becomes:

$$P_1 = k(T_{\text{A}} + T_1)G_1.$$

---

[1]While some pulsars - like the Crab pulsar B0531+21 are indeed seen across the spectrum, their spectral index at radio frequencies is still negative - implying an inversion with respect to the Planck spectrum

For a system chain with N elements, the power at the end will therefore be:

$$P_N = k(T_\mathrm{A} + T_\mathrm{X}) \prod_{i=1}^{N} G_\mathrm{i}$$

with the additional noise temperature:

$$T_\mathrm{X} = T_1 + \frac{T_2}{G_1} + \frac{T_3}{G_1 G_2} + \ldots + \frac{T_N}{G_1 G_2 \ldots G_{N-1}} = T_1 + \sum_{i=2}^{N} \frac{T_i}{\prod_{j=1}^{i-1} G_j}. \qquad (2.5)$$

This clearly demonstrates the importance of the first element in the system: its noise temperature is the most prominent addition to the system-induced noise and its gain reduces all other contributions. This is the reason why the receiving systems are generally cooled to temperatures of several tens of Kelvin and why the first element after the receiver is a low-noise amplifier (as depicted in Figure 2.2).

2.2.3   Polarisation

Electromagnetic radiation manifests itself as a transverse wave with perpendicular magnetic and electric fields. A monochromatic electric wave can therefore be represented as a vector perpendicular to the direction of propagation:

$$\begin{aligned}
e_\mathrm{x} &= a_\mathrm{x} \cos\left(2\pi(z/\lambda - \nu t) + \phi_1\right) \\
e_\mathrm{y} &= a_\mathrm{y} \cos\left(2\pi(z/\lambda - \nu t) + \phi_2\right) \\
e_\mathrm{z} &= 0,
\end{aligned} \qquad (2.6)$$

in which a_x and a_y are the amplitudes in x and y directions and $\phi_1 - \phi_2$ is the phase offset between the two wave components. Traditionally, the characteristics of an electric wave are expressed through the Stokes parameters, which are defined as follows:

$$\begin{aligned}
S_0 &= I &&= a_\mathrm{x}^2 + a_\mathrm{y}^2 \\
S_1 &= Q &&= a_\mathrm{x}^2 - a_\mathrm{y}^2 \\
S_2 &= U &&= 2a_\mathrm{x} a_\mathrm{y} \cos(\phi_1 - \phi_2) \\
S_3 &= V &&= 2a_\mathrm{x} a_\mathrm{y} \sin(\phi_1 - \phi_2).
\end{aligned} \qquad (2.7)$$

In simple terms, I can be though of as the total power of the wave, Q as a measure of ellipticity along the axes, U is a measure of ellipticity at 45° to the axes and V is a measure of circular polarisation. However, this image only applies to waves with an infinitessimal bandwidth. For practical applications, we will now rederive these relationships for a signal with finite bandwidth. For such a signal, Equation 2.6

becomes:

$$e_x^r = \int_0^\infty b_x(\nu) \cos\left(\phi(\nu) - 2\pi\nu t\right) d\nu$$

$$e_y^r = \int_0^\infty b_y(\nu) \cos\left(\phi(\nu) - 2\pi\nu t\right) d\nu \tag{2.8}$$

Where $b(\nu)$ is the amplitude as a function of observing frequency, otherwise known as the bandpass of the signal. This definition can logically be expanded into a Fourier transform:

$$e_x = e_x^r + i \int_0^\infty b_x(\nu) \sin\left(\phi(\nu) - 2\pi\nu t\right) d\nu, \tag{2.9}$$

and similarly for the y-component. This extended definition of the electric field is known as the *analytic signal*. An alternative but equivalent way to consider this is as the expansion of the components of the electric vector as follows:

$$e(t) = e^r(t) + ie^r(t) * h(t), \tag{2.10}$$

where $*$ denotes convolution and $h(t) = (\pi t)^{-1}$. The convolution $x(t) * h(t)$ is the Hilbert transform and it can be more readily analysed in the Fourier domain, since the convolution theorem states that convolution in the time domain is equivalent to multiplication in the Fourier domain. Hence, given the Fourier transform of $h(t)$ to be:

$$H(\nu) = \begin{cases} -i & \text{if } \nu > 0 \\ i & \text{if } \nu < 0 \end{cases} \tag{2.11}$$

and therefore:

$$\begin{aligned} E(\nu) &= FT(e(t)) = E(\nu) + iE(\nu)H(\nu) \\ &= \begin{cases} 2E(\nu) & \text{if } \nu > 0 \\ 0 & \text{if } \nu < 0 \end{cases} \end{aligned} \tag{2.12}$$

with $E^r(\nu)$ the Fourier transform of the signal $e^r(t)$ and $E(\nu)$ the Fourier transform of the analytic signal.

We have defined the analytic signal as:

$$\vec{e}(t) = \begin{pmatrix} e_x(t) \\ e_y(t) \end{pmatrix} = \begin{pmatrix} a_x e^{i(\phi_x(t) - 2\pi\nu_0 t)} \\ a_y e^{i(\phi_y(t) - 2\pi\nu_0 t)} \end{pmatrix}. \tag{2.13}$$

The coherency matrix $\bar{\rho}$ of this vector can be related to the Stokes parameters as outlined by Britton (2000):

$$\bar{\rho} = \begin{pmatrix} \langle |e_x|^2 \rangle & \langle e_x e_y^* \rangle \\ \langle e_y e_x^* \rangle & \langle |e_y|^2 \rangle \end{pmatrix} = \frac{1}{2} \begin{pmatrix} S_0 + S_1 & S_2 - iS_3 \\ S_2 + iS_3 & S_0 - S_1 \end{pmatrix} \tag{2.14}$$

It is easily derived from this that the Stokes parameters can be derived from the coherency products as follows:

$$
\begin{pmatrix} S_0 \\ S_1 \\ S_2 \\ S_3 \end{pmatrix} = \begin{pmatrix} \langle|e_x|^2\rangle + \langle|e_y|^2\rangle \\ \langle|e_x|^2\rangle - \langle|e_y|^2\rangle \\ 2\Re(\langle e_y e_x^*\rangle) \\ 2\Im(\langle e_y e_x^*\rangle) \end{pmatrix},
\tag{2.15}
$$

with $\Re(\langle e_y e_x^*\rangle)$ and $\Im(\langle e_y e_x^*\rangle)$ the real and imaginary parts of $\langle e_y e_x^*\rangle$, respectively. It is important to note that $e_x^2 = a_x^2$ and $e_y^2 = a_y^2$ are simply the amplitudes of the signals in the two orthogonal directions we commenced with (Equation 2.6) and are therefore readily measured. Also, $2\Re(\langle e_y e_x^*\rangle) = 2\langle a_x a_y \cos(\phi_x - \phi_y)\rangle$ is the average power of the product of those two original signals and therefore also easily measured. Finally, $2\Im(\langle e_y e_x^*\rangle) = 2a_x a_y \sin(\phi_x - \phi_y)\rangle = 2a_x a_y \cos(\phi_x - \phi_y - \pi/2)\rangle$ is the same averaged power, but now with one signal shifted by $90°$. All four of these numbers - and therefore all the values of the coherency matrix $\bar{\rho}$ (Equation 2.14), are readily determined from two orthogonal probes, both in hardware and in software. Most of the receivers used for data acquisition in this thesis measure two orthogonal and linear components to the electric field as described above. On a more general note, however, it is possible to rewrite Equation 2.6 in terms of two circular probes with opposite handedness - in which case the same results ensue. Such a derivation is beyond the scope of this introduction, but can be found in Rohlfs & Wilson (2000).

2.3   Observing Hardware

2.3.1   Basic Signal Chain

Figure 2.2 shows the components of a signal chain for pulsar timing observations. The first elements of the system are standard in all radio astronomy observations and will be discussed here. Starting at the left end, we have the radio antenna, which focusses the radio waves originating at the astronomical source. To this end, the telescope surface is parabolic, with a receiver (which converts the electromagnetic radiation into voltages) in the focus[2]. For reasons clarified in §2.2.2, the receivers are cooled and the signal is passed through a cryogenically cooled low noise amplifier (LNA). Next the signal will be transfered to the ground or control room, where all other hardware resides. This involves data transfer via cables that normally attenuate high-frequency ($\nu \approx 1\,\mathrm{GHz}$) signals. In order to transfer the radio signal with minimal loss, its frequency is therefore first downconverted. This is accomplished

---

[2]Note that in the case of a Cassegrain system there is only a reflective surface near the focus of the paraboloid, while the receivers are placed at the secondary focus, either to the side of the antenna (Green Bank Telescope, e.g.) or, more commonly, in the dish surface (Australia Telescope Compact Array, e.g.). For ease of discussion, we will consider the set-up of the Parkes Radio Telescope, which has the receivers and focus cabin at the focus of the paraboloid.

by mixing the signal with that from a local oscillator (LO) at a precisely defined frequency. Mathematically speaking, this mixing is a multiplication of two waves, which equates to an upconverted signal at the summed frequency and a downconverted signal at the difference of the frequencies:

$$\cos \nu_{\mathrm{obs}} t \times \cos \nu_{\mathrm{LO}} t = 0.5 \big(\cos (\nu_{\mathrm{obs}} - \nu_{\mathrm{LO}})t + \cos (\nu_{\mathrm{obs}} + \nu_{\mathrm{LO}})t \big)$$

The downconverted signal is selected by running the signal through a low-pass filter subsequently. Notice that, while the LO frequency ν_{LO} is precisely defined, the observed signal has a finite bandwidth B that depends on the receiver response. The downconverted signal therefore has a bandwidth as well, with a frequency range of $\nu_{\mathrm{obs}} - \nu_{\mathrm{LO}} - B/2$ to $\nu_{\mathrm{obs}} - \nu_{\mathrm{LO}} + B/2$. This means that if the LO frequency is smaller than the observed centre frequency ($\nu_{\mathrm{LO}} < \nu_{\mathrm{obs}}$), the resulting downconverted signal will be an exact copy of the original bandpass, simply translated in frequency - this is called *upper sideband* downconversion. If the reverse is true: $\nu_{\mathrm{LO}} > \nu_{\mathrm{obs}}$, then the bandpass is mirrored in addition to being translated. This is called *lower sideband* downconversion. Through downconversion, the radio frequency (RF) signal is reduced to an intermediate frequency (IF) signal. The low-pass filter used in this downconversion process can also be used as a bandpass filter to select the frequency range required by the backend. Alternatively, another stage of filtering may need to be applied. Following another step of amplification, the signal is passed on to the different pulsar instruments or backends, which are described below.

2.3.2   Analogue Filter Banks

There are two types of resolution a pulsar backend attempts to achieve. Firstly, time resolution is required at a level well below the pulse period. Secondly, frequency resolution is required in order to enable mitigation of the dispersive effects illustrated in Figure 1.5 and described by Equation 1.14. The easiest means to achieve frequency resolution is to pass the signal through a series of parallel band-pass filters with adjoining frequency responses. Each of these filters creates a single frequency channel, the width of which determines the frequency resolution of our data. The analogue power is subsequently sampled in each of these channels, at a given sampling periodicity that determines the time resolution. Finally, the signals of the different channels are shifted in time relative to each other, according to the expected DM delay calculated through Equation 1.14. While this corrects for the DM delay between the channels, it is incapable of correcting the smearing within each channel.

The analogue filter bank system used in this thesis, provides 512 frequency channels over a total bandwidth of 256 MHz - resulting in a 500 kHz channel bandwidth at a centre frequency of around 1400 MHz. Equation 1.14 can be used to calculate the DM smearing within a channel - for PSR J1939+2134, for example:

$$\Delta t = 4.15 \times 10^3 DM \left(1399.75^{-2} - 1400.25^{-2} \right) = 107 \, \mu\mathrm{s}$$
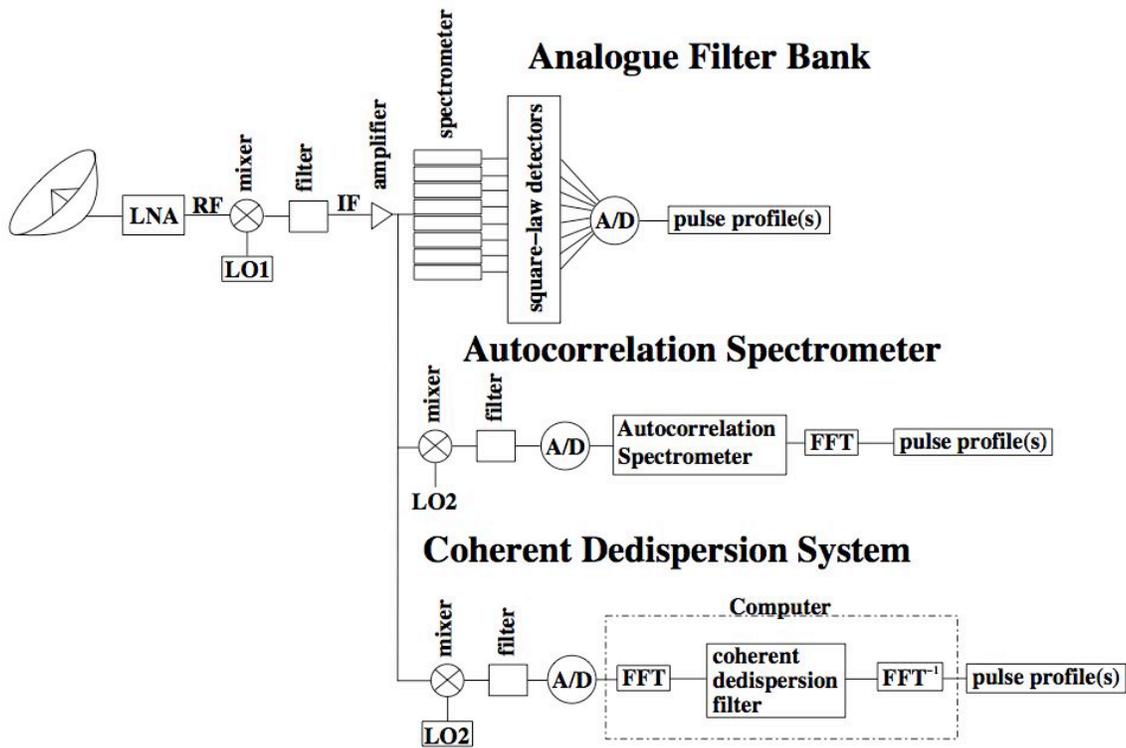
Figure 2.2: Fundamental system chain for different backends used for the radio pulsar observations analysed in this thesis.
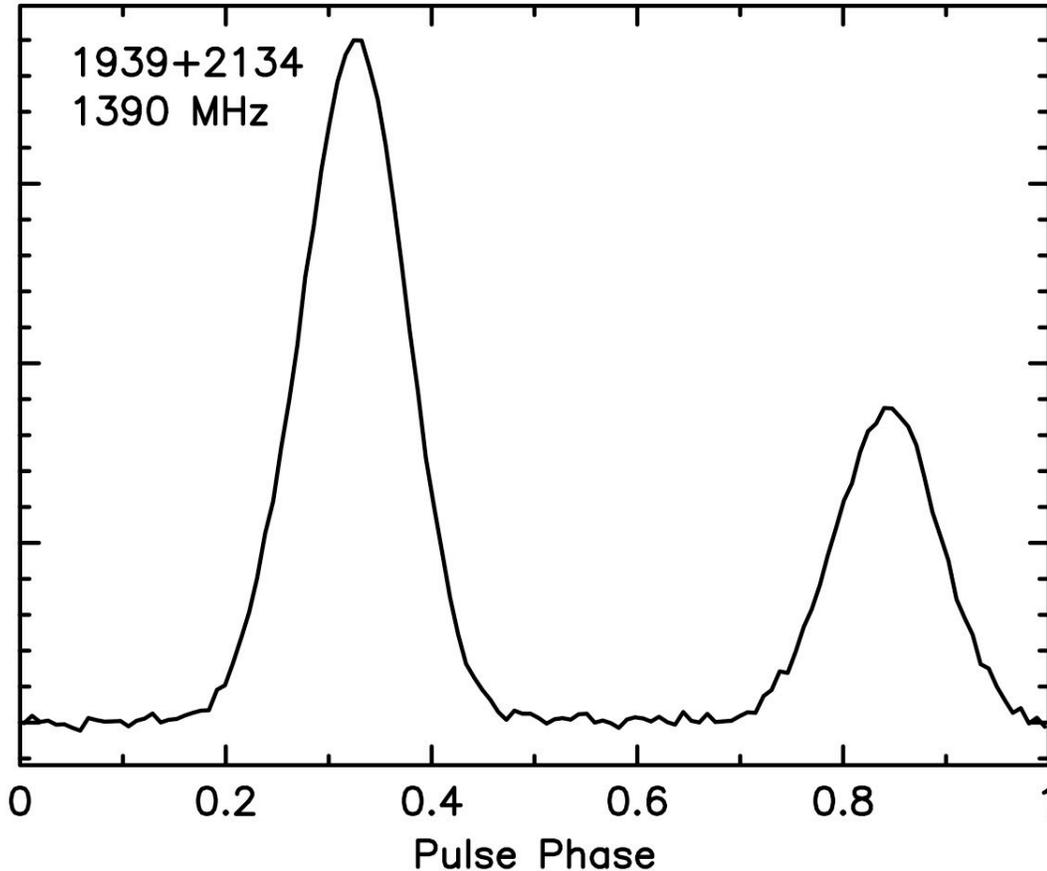
Figure 2.3: Pulse profile of PSR J1939+2134, taken with an analogue filter bank backend. The smearing of the pulse peak by 9 bins is clearly visible when compared to Figure 2.5.

with DM = $71.0226\,\mathrm{cm}^{-3}$pc. With 128 time bins across a profile for a pulsar with $P = 1.5578\,\mathrm{ms}$, this results in nearly nine bins of smearing, which can be seen in Figure 2.3, when compared to 2.5.

There are a few disadvantages to these systems. Firstly, the spectrometer (band-pass filters) is implemented in hardware and is thus inflexible: the channel number and width cannot easily be changed for pulsars with different dispersion measures. This leads to large smearing for pulsars with high DM (like the example of Figure 2.3, PSR J1939+2134). Secondly and more importantly, there is a trade-off between channel number and time resolution. On the one hand one desires a large number of very narrow channels so that the DM smearing can be optimally corrected. Whereas on the other, the narrower a single channel is, the less time resolution it will have, owing to the finite rise time of the filter. Finally, the cost of a large number of filters can be high and the response may differ between filters, leading to systematic errors.

2.3.3   Autocorrelation Spectrometers

As rederived in Rohlfs & Wilson (2000), the Wiener-Khinchin theorem states that the autocorrelation function of a signal is the Fourier transform of the power spectrum of that same signal. This fact is used by autocorrelation spectrometers to facilitate obtaining frequency resolution in configurable (flexible) hardware. In practise such a system works in the following steps:

Digitisation of the analogue signal: The analogue signal, $S(t)$, is sampled at intervals of t_{samp}. Notice this digitisation step comes at the start of the process, while it came last in the case of analogue filterbanks. We call the digitised signal $S_{\mathrm{d}}(t)$ and it consists of discrete voltages. Sampling is performed at the Nyquist sampling rate: $t_{\mathrm{samp}} = 1/(2B)$, where B is the bandwidth of the signal. For a $256\,\mathrm{MHz}$ bandwidth system, this implies $t_{\mathrm{samp}} \approx 2\,\mathrm{ns}$.

Addition of delays to copies of the signal stream: The digitised signal, $S_{\mathrm{d}}(t)$, is delayed by $2N_{\mathrm{chan}}$ lags of size $\Delta\tau$, resulting in delayed signals $S_{\mathrm{d}}(t + i\Delta\tau)$ with $i = 1$ to N_{chan}. The number of lags used will eventually determine the number of frequency channels in our data, hence its naming.

Autocorrelation of the signal: Given the definition of autocorrelation:

$$R(i\Delta\tau) = \langle S_{\mathrm{d}}(t) \times S_{\mathrm{d}}(t + i\Delta\tau)\rangle$$

the next step is to multiply the original and delayed signals and to average them, resulting in the autocorrelation of the signal, as a function of lag: $R(\tau)$. This multiplying and averaging continues during the "dump time", t_{dump}, after which $R(\tau)$ is saved. The dump time defines the time resolution of the final observation and is therefore required to be much smaller than the pulse period: $t_{\mathrm{dump}} \ll P$. As an example, consider a $3\,\mathrm{ms}$ pulsar and a desired 256 time bins across its profile. This would require: $t_{\mathrm{dump}} \approx 12\,\mu\mathrm{s}$. Assuming we desired 512 frequency channels, the longest lag in the autocorrelation would be $\Delta\tau \times 512 = 1\,\mu\mathrm{s}$, which is much less than the dump time.

Folding at the pulse period: In order to increase the SNR and decrease the required disk space for data storage, the autocorrelation functions at equal pulse phases can be averaged for an arbitrary amount of time. This is the first step that can be performed in software, while all previous steps usually happen in hardware. The autocorrelation spectrometer used to gather some of the data for this thesis (the "fast pulsar timing machine" or FPTM) however, used a numerically clocked oscillator to perform the folding in hardware.

Fourier transform to obtain a pulse profile: At this stage we have the autocorrelation values as a function of pulse phase and correlation delay. In order to convert this to power as a function of phase and frequency (as seen in Figure 1.5), we perform a Fourier transform for each pulsar phase bin. This is

traditionally done off-line, although current computing power would be able to do this in real time. This finally results in a pulse profile with frequency resolution $\Delta\nu \approx B/N_{\mathrm{chan}}$ and time resolution t_{samp}.

Dedispersion of the pulse profile: As with the analogue filterbank systems, dispersion effects are removed by shifting the frequency channels with respect to each other. Within the frequency channels, the effects remain, so the dispersion smearing is still determined by the width of the frequency channels.

Even though almost all of the above is performed in hardware, this hardware is much more easily modified and configured than the bandpass filters of the analogue filter bank system. This implies there is much larger flexibility in both frequency and time resolution. While the fundamental trade-off of time versus frequency resolution still holds, these numbers can more easily be optimised depending on the observed pulsar, choosing higher frequency resolution for high-DM pulsars and higher time resolution for low-DM pulsars with narrow pulses. The observing set-up for the high-DM pulsar PSR J1939+2134 can therefore provide higher frequency resolution, resulting in less smearing than was the case for analogue filter bank systems (see figures 2.3 and 2.4).

Another important difference between autocorrelation spectrometers and analogue filter banks is that the former need a baseband input signal. Baseband implies that the frequency range of the signal lies between 0 and the bandwidth B. The main reason for this requirement is that the Nyquist sampling rate is far reduced, from $1/(2f_{\mathrm{h}})$ to $1/(2B)$, as used above ($f_{\mathrm{h}} = f_0 + B/2$ being the highest frequency of the IF signal and B the bandwidth of the signal). The transformation to baseband is accomplished through a second stage of down-conversion, as depicted in Figure 2.2.

2.3.4   Coherent Dedispersion Systems

In Section 1.2.3, we have commented on the dispersive effects of the ISM due to the varying group velocity of electromagnetic waves travelling through an ionised plasma. We also derived the relative time delay this induced between two frequency channels. This relative time delay is - as described in §2.3.2 and §2.3.3 - corrected in pulsar backend systems after the signal has been detected and recorded. However, to correct this dispersion in a continuous and absolute way, i.e. to *phase-coherently* dedisperse a pulsar signal, requires a somewhat more involved treatment.

The basic signal chain for coherent dedispersion backend systems is identical to that for autocorrelation spectrometers: the IF signal is downconverted to baseband and subsequently digitised. Next, the signal is Fourier transformed to the frequency domain.

The reason for Fourier transforming is that dispersion is mathematically a convolution process. Using the convolution theorem which states that convolution in time is multiplication in frequency, deconvolving in Fourier space can be done through division, which is computationally easily achieved. The frequency response function
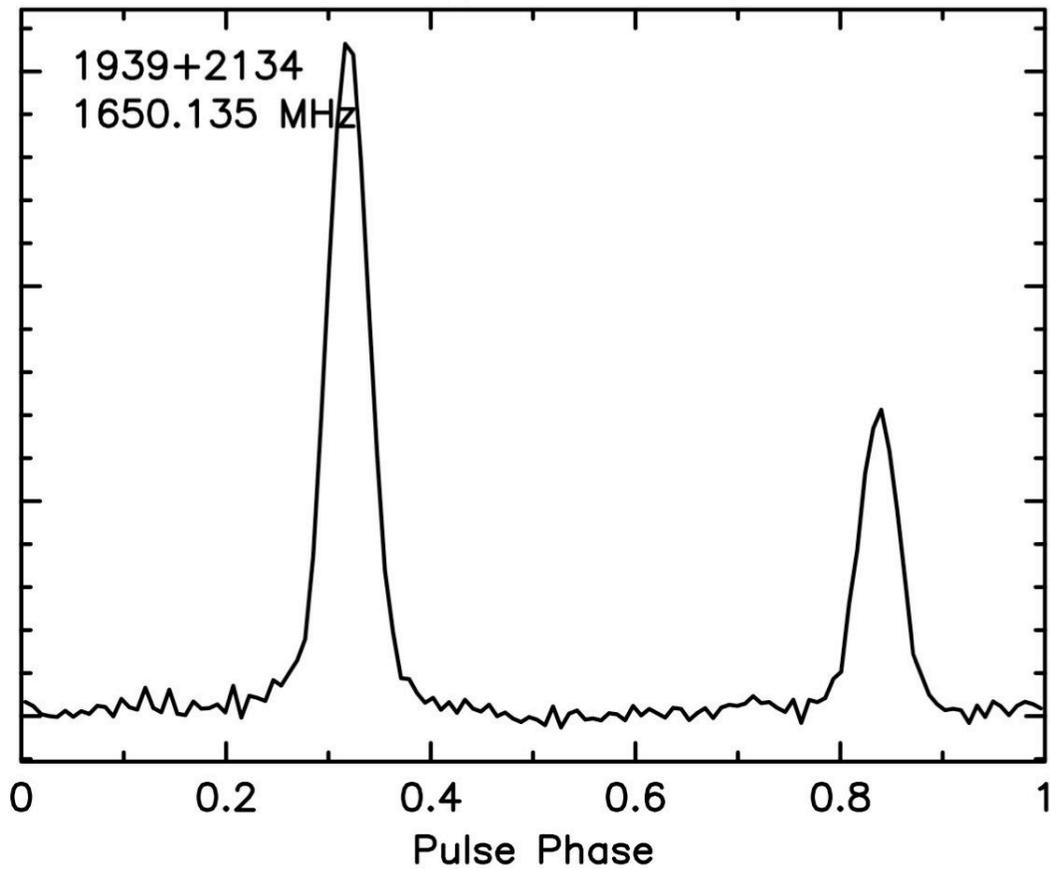
Figure 2.4: Pulse profile of PSR J1939+2134, taken with the FPTM autocorrelation spectrometer backend. The smearing is considerably reduced when compared to Figure 2.3, but sharp features visible with coherent dedispersion backends (Figure 2.5), remain unresolved.

characterising the dispersion effects of the ISM was derived by Hankins & Rickett (1975) and shown to have the following analytic form:

$$H(f_0 + \Delta f) = \exp\left(\frac{i2\pi D(\Delta f)^2}{f_0^2\,(f_0 + \Delta f)}\right) \tag{2.16}$$

with f_0 the centre frequency, Δf (for which holds $-B/2 < \Delta f < B/2$) the offset from the centre frequency and D the dispersion constant as defined in Equation 1.12. Removal of the dispersive effects can therefore easily be accomplished by dividing the Fourier transform of the signal by this function. At present, computing power is sufficient to perform this coherent dedispersion in real time, followed by an inverse Fourier transform, providing the observer with an almost instantaneous view of the pulsar, if it is sufficiently bright. However, during the first half of this decade, the raw data had to be stored for off-line deconvolution.

Since the interstellar dispersion effects are now removed within the frequency channels, a small channel bandwidth is not urgently required anymore. Given the fundamental limitation that frequency and time resolution are inversely proportional in Fourier analysis, this reduced need for small bandwidths of frequency channels, allows higher time resolution. An example for a coherently dedispersed pulse is shown in Figure 2.5, which shows a narrow spike on the trailing edge of the main pulse of PSR J1939+2134. This narrow spike was unresolved with the older backends, mostly due to DM smearing.

2.3.5 Overview of Instruments

Five different instruments were used in the data collection for this thesis. Two of these were only used on PSR J0437−4715, as described in Chapter 3. These were:

S2: The S2 VLBI recorder is a 16 MHz bandwidth recorder that stores raw data with 31 ns time resolution onto eight SVHS tapes for offline coherent dedispersion. More details are provided in Wietfeldt et al. (1998).

CPSR: The first generation Caltech-Parkes-Swinburne Recorder, CPSR, recorded a 20 MHz bandpass at dual polarisation onto DLT tapes. The data was coherently dedispersed offline and generated pulse profiles with a resolution of 4096 bins per pulse period. More information can be found in van Straten et al. (2000) and references therein.

The three back ends that were used for both PSR J0437−4715 and for all pulsars described in Chapter 4, were:

FB: The analogue filter bank had a 256 MHz bandwidth with 512 frequency channels. It generates profiles after offline processing in software. Its time resolution of $t_s = 80\,\mu s$ limited the effective number of bins to P/t_s where P is the pulsar's pulse period. This system was upgraded in the early 2000s to provide higher time resolution and higher bandwidth.
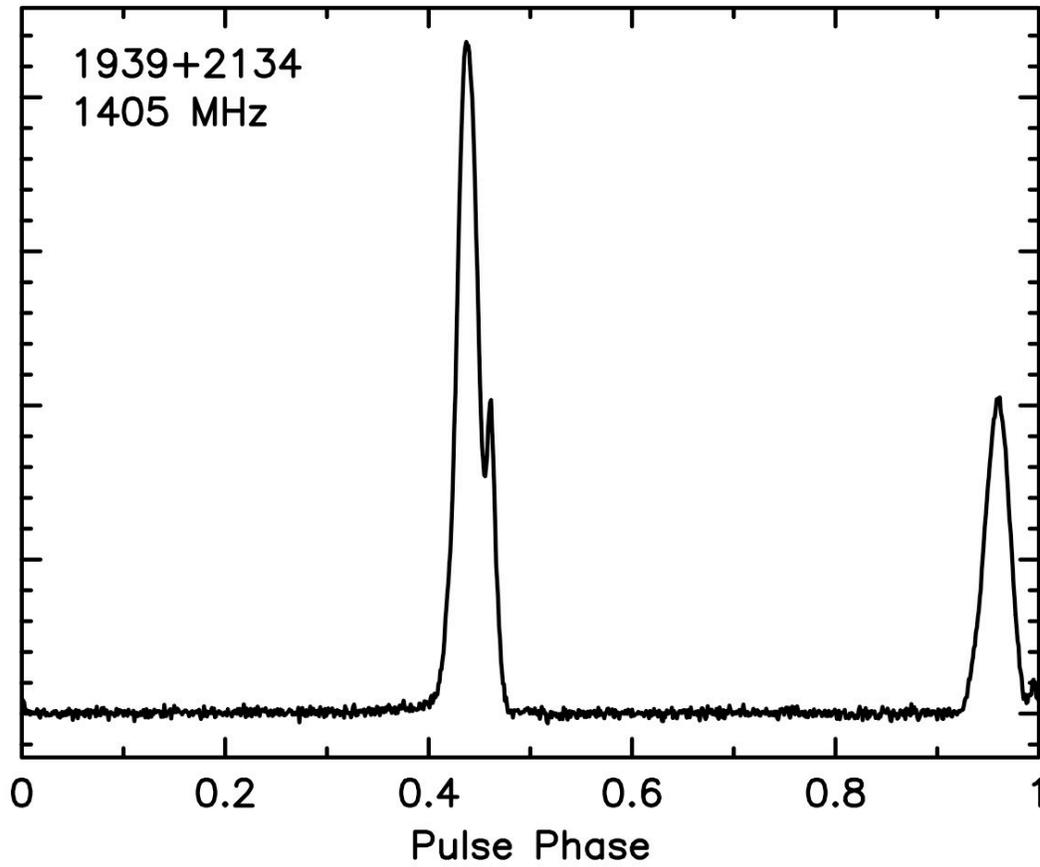
Figure 2.5: Pulse profile of PSR J1939+2134, taken with the CPSR2 coherent dedispersion backend system. Sharp features are now fully resolved, in contrast to observations made with other systems (figures 2.3 and 2.4).

FPTM: The fast pulsar timing machine is an autocorrelation spectrometer with a maximum bandwidth of 256 MHz and up to 1024 bins across a profile. Details are provided in Sandhu et al. (1997) and Sandhu (2001).

CPSR2: The second generation Caltech-Parkes-Swinburne recorder, CPSR2, is a coherent dedispersion baseband system that samples two independent 64 MHz-wide observing bands. For observations around an observing frequency of 1400 MHz, these two bands were placed adjacent to each other, with centre frequencies at 1341 and 1405 MHz. In case of observations in the 50 cm ($\approx$685 MHz) band, one observing band was either ignored or centred around 3 GHz wavelength, using the coaxial 10/50 cm receiver at Parkes. More details are provided in Hotan, Bailes & Ord (2006).

Chapter 3

High-Precision Timing of PSR J0437−4715

Twenty-five years ago, general relativity was often thought of more as a branch of mathematics than of physics.
Backer & Hellings, "Pulsar Timing and General Relativity", ARA&A, 1986

This chapter was previously published as Verbiest et al., "Precision Timing of PSR J0437−4715: An Accurate Pulsar Distance, a High Pulsar Mass, and a Limit on the Variation of Newton's Gravitational Constant", published in the Astrophysical Journal, volume 679, pp. 675–680, 2008 May 20. Minor updates and alterations have been made for the purpose of inclusion in this thesis.

3.1   Abstract

Analysis of ten years of high-precision timing data on the millisecond pulsar PSR J0437−4715 has resulted in a model-independent kinematic distance based on an apparent orbital period derivative, $\dot{P}_{\rm b}$, determined at the 1.5% level of precision ($D_{\rm k} = 157.0 \pm 2.4\,{\rm pc}$), making it one of the most accurate stellar distance estimates published to date. The discrepancy between this measurement and a previously published parallax distance estimate is attributed to errors in the DE200 Solar System ephemerides. The precise measurement of $\dot{P}_{\rm b}$ allows a limit on the variation of Newton's gravitational constant, $|\dot{G}/G| \leq 2.3 \times 10^{-11}\,{\rm yr}^{-1}$. We also constrain any anomalous acceleration along the line of sight to the pulsar to $|a_{\odot}/c| \leq 1.5 \times 10^{-18}\,{\rm s}^{-1}$ at 95% confidence and derive a pulsar mass, $m_{\rm psr} = 1.76 \pm 0.20\,M_{\odot}$, one of the highest estimates so far obtained.

3.2   Introduction

Johnston et al. (1993) reported the discovery of PSR J0437−4714, the nearest and brightest millisecond pulsar known. Within a year, the white dwarf companion and pulsar wind bow shock were observed (Bell, Bailes & Bessell 1993) and pulsed X-rays were detected (Becker & Trümper 1993). The proper motion and an initial estimate of the parallax were later presented along with evidence for secular change in the inclination angle of the orbit due to proper motion (Sandhu et al. 1997). Using high time resolution instrumentation, the three-dimensional orbital geometry of the binary system was determined, enabling a new test of general relativity (GR; van Straten et al. 2001). Most recently, multi-frequency observations were used to compute the dispersion measure structure function (You et al. 2007a), quantifying the turbulent character of the interstellar medium towards this pulsar.

The high proper motion and proximity of PSR J0437−4715 led to the prediction (Bell & Bailes 1996) that a distance measurement independent of parallax would be available within a decade, when the orbital period derivative $(\dot{P}_{\rm b})$ would be determined to high accuracy. Even if the predicted precision of $\approx 1\%$ would not be achieved, such a measurement would be significant given the strong dependence of most methods of distance determination on relatively poorly constrained models and the typically large errors on parallax measurements. Even for nearby stars, both the Hubble Space Telescope and the Hipparcos satellite give typical distance errors of 3% (Valls-Gabaud 2007) and so far only two distances beyond 100 pc have been determined at $\approx 1\%$ uncertainty (Torres et al. 2007). This kinematic distance is one of the few model-independent methods that does not rely upon the motion of the Earth around the Sun.

As demonstrated by Damour & Taylor (1991), $\dot{P}_{\rm b}$ can also be used to constrain the variation of Newton's gravitational constant. The best such limit from pulsar timing to date ($|\dot{G}/G| = (4 \pm 5) \times 10^{-12}\,{\rm yr}^{-1}$ from PSR B1913+16; Taylor 1993) is compromised due to the poorly constrained equation of state (EOS) for the neutron star companion (Nordtvedt 1990). The slightly weaker but more reliable limit of $|\dot{G}/G| = (-9 \pm 18) \times 10^{-12}\,{\rm yr}^{-1}$ (from PSR B1855+09, which has a white dwarf companion; Kaspi, Taylor & Ryba 1994) should therefore be considered instead. However, neither of these limits come close to that put by lunar laser ranging (LLR; Williams, Turyshev & Boggs 2004): $\dot{G}/G = (4 \pm 9) \times 10^{-13}\,{\rm yr}^{-1}$. Besides limiting alternative theories of gravity, bounds on $\dot{G}$ can also be used to constrain variations of the Astronomical Unit (AU). Current planetary radar experiments (Krasinsky & Brumberg 2004) have measured a significant linear increase of $dAU/dt = 0.15 \pm 0.04\,{\rm m\ yr}^{-1}$, which may imply $\dot{G}/G = (-1.0 \pm 0.3) \times 10^{-12}\,{\rm yr}^{-1}$, just beyond the sensitivity of the limits listed above.

As mentioned before, the EOS for dense neutron star matter is very poorly constrained. Specifically, it is generally accepted that nuclear matter would degenerate into quark matter as pressure and density increase, but the critical pressure and density at which this would happen are as yet mostly unknown (Lattimer & Prakash

2007). Alternative scenarios of further degeneration and state changes into hyperons or Bose-Einstein condensates of pions and/or kaons are also not ruled out, leading to uncertainty about what the fundamental ground state of matter is. In order to probe matter at such high densities and constrain potential EOSs for dense nuclear matter, two avenues are currently open. One is provided by particle accelerators such as the large hadron collider (LHC) at CERN and the RHIC at the Brookhaven national laboratory. The other possibility is provided by probing the masses and radii (and therefore densities) of neutron stars, the densest known objects without an event horizon (Weise 2008).

While no accurate measurement of a neutron star radius has been made to date, the combination of the requirement for hydrostatic equilibrium with the pressure expected by a given EOS, provides an EOS-dependent upper limit on neutron star masses (for a more detailed derivation, see Lattimer & Prakash 2007). While most measured pulsar masses fall within a narrow range close to $1.4\,M_\odot$, recent results on the pulsars NGC 6440B, Terzan 5 I and Terzan 5 J indicate the potential for substantially heavier pulsars (Freire et al. 2008; Ransom et al. 2005); however, as discussed in more detail in Section 3.6, these predictions do not represent objective mass estimates.

The remainder of this chapter is structured as follows: Section 3.3 describes the observations, data analysis and general timing solution for PSR J0437−4715. Section 3.4 describes how the measurement of $\dot{P}_\mathrm{b}$ leads to a new and highly precise distance. In Section 3.5, this measurement is combined with the parallax distance to derive limits on $\dot{G}$ and the Solar System acceleration. Section 3.6 presents the newly revised pulsar mass and our conclusions are summarised in Section 3.7.

3.3 Observations and Data Reduction

Observations of PSR J0437−4715 were made over a time span of ten years (see Figure 3.1), using the Parkes 64-m radio telescope. Two 20 cm receiving systems (the central beam of the Parkes multi-beam receiver (Staveley-Smith et al. 1996a) and the H-OH receiver) were used and four generations of digital instrumentation (see Table 3.1): the Fast Pulsar Timing Machine (FPTM), the S2 VLBI recorder and the Caltech-Parkes-Swinburne Recorders (CPSR and CPSR2), all described in Chapter 2.

3.3.1 Arrival Time Estimation

For the FPTM, S2 and CPSR backends, the uncalibrated polarisation data were combined to form the polarimetric invariant interval (Britton 2000) and each observation was integrated in time and frequency before pulse arrival times were calculated through standard cross-correlation with an instrument-dependent template profile. For the CPSR2 data, the technique described by van Straten (2004) was

used to calibrate 5 days of intensive PSR J0437−4715 observations made on 2003 July 19 to 21, 2003 August 29 and 2005 July 24. The calibrated data were integrated to form a polarimetric template profile with an integration length of approximately 40 hours and frequency resolution of 500 kHz. This template profile and Matrix Template Matching (MTM, van Straten 2006) were used to calibrate the three years of CPSR2 data. An independent MTM fit was performed on each five-minute integration, producing a unique solution in each frequency channel, as shown in Figure 2 of van Straten (2006). The calibrated data were then integrated in frequency to produce a single full-polarisation profile at each epoch. MTM was then used to derive time-of-arrival (TOA) estimates from each calibrated, five-minute integration. The application of MTM during the calibration and timing stages reduced the weighted RMS of the CPSR2 post-fit timing residuals by a factor of two. All the data reduction described above was performed using the PSRCHIVE software package (Hotan, van Straten & Manchester 2004).

Table 3.1: Characteristics of the timing data from the four instruments used.

Backend	Date range	Bandwidth	RMS Residual
FPTM	1996 Apr – 1997 May	256 MHz	368 ns
S2	1997 Jul – 1998 Apr	16 MHz	210 ns
CPSR	1998 Aug – 2002 Aug	20 MHz	218 ns
CPSR2	2002 Nov – 2006 Mar	2×64 MHz[a]	164 ns
Backend	**Observation length[b]**	**Number of TOAs**	**TOA error[b]**
FPTM	10 min	207	500 ns
S2	120 min	117	160 ns
CPSR	15 min	1782	250 ns
CPSR2	60 min	741	140 ns

[a] CPSR2 records two adjacent 64 MHz bands simultaneously at 20 cm.

[b] Displayed are typical values only.

3.3.2   Timing Analysis

Most data were recorded at a wavelength of 20 cm; however, in the final three years, simultaneous observations at 10 and 50 cm were used to measure temporal variations of the interstellar dispersion delay (corrections for these variations were implemented in a way similar to that of You et al. 2007a). A linear trend of these delays was also obtained for the year of FPTM data, using data at slightly different frequencies close to 1400 MHz.

Table 3.2: PSR J0437−4715 timing model parameters[a]

Parameter Name and Units	Parameter Value	T2 Error[b]	M-C Error[b]	Error Ratio
Fit and Data Set				
MJD range	50191.0–53819.2			
Number of TOAs	2847			
Rms timing residual (μs)	0.199			
Measured Quantities				
Right ascension, α (J2000)	$04^{\mathrm{h}}37^{\mathrm{m}}15^{\mathrm{s}}.8147635$	3	29	9.8
Declination, δ (J2000)	$-47°15'08''.624170$	3	34	11
Proper motion in α,				
$\mu_\alpha \cos\delta$ (mas yr^{-1})	121.453	1	10	8.7
Proper motion in δ, μ_δ (mas yr^{-1}) ..	−71.457	1	12	9.0
Annual parallax, π (mas)	6.65	7	51	7.9
Dispersion measure, DM (cm^{-3} pc)	2.64476	7	d	d
Pulse period, P (ms)	5.757451924362137	2	99	47
Pulse period derivative, $\dot{P}$ (10^{-20}) ..	5.729370	2	9	4.8
Orbital period, P_{b} (days)	5.74104646[c]	108	200	1.9
Orbital period derivative, $\dot{P}_{\mathrm{b}}$ (10^{-12})	3.73	2	6	2.5
Epoch of periastron passage,				
T_0 (MJD)	52009.852429[c]	582	780	1.3
Projected semi-major axis, x (s)	3.36669708[c]	11	14	1.4
Longitude of periastron, ω_0 (°)	1.2224[c]	365	490	1.3
Orbital eccentricity, e (10^{-5})	1.9180	3	7	2.1
Periastron advance, $\dot{\omega}$ (° yr^{-1})	0.01600[c]	430	800	1.8
Companion mass, m_2 (M$_\odot$)	0.254[c]	14	18	1.3
Longitude of ascension, Ω (°)	207.8[c]	23	69	3.0
Orbital inclination, i (°)	137.58	6	21	3.7
Set Quantities				
Reference epoch for P, α and δ determination (MJD)	52005			
Reference epoch for DM determination (MJD)	53211			

[a] These parameters are determined using TEMPO2 which uses the International Celestial Reference System and Barycentric Coordinate Time. As a result this timing model must be modified before being used with an observing system that inputs TEMPO format parameters. See Hobbs, Edwards & Manchester (2006) for more information.

[b] Given uncertainties are 1σ values in the last digits of the parameter values. "T2" refers to the formal uncertainties provided by the TEMPO2 software package, "M-C" refers to the uncertainties resulting from the Monte-Carlo simulations.

[c] Because of large covariances, extra precision is given for selected parameters.

[d] Dispersion measure was determined through alignment of simultaneous CPSR2 observations centred at 1341 MHz and 1405 MHz. The effect of red noise is therefore not applicable.
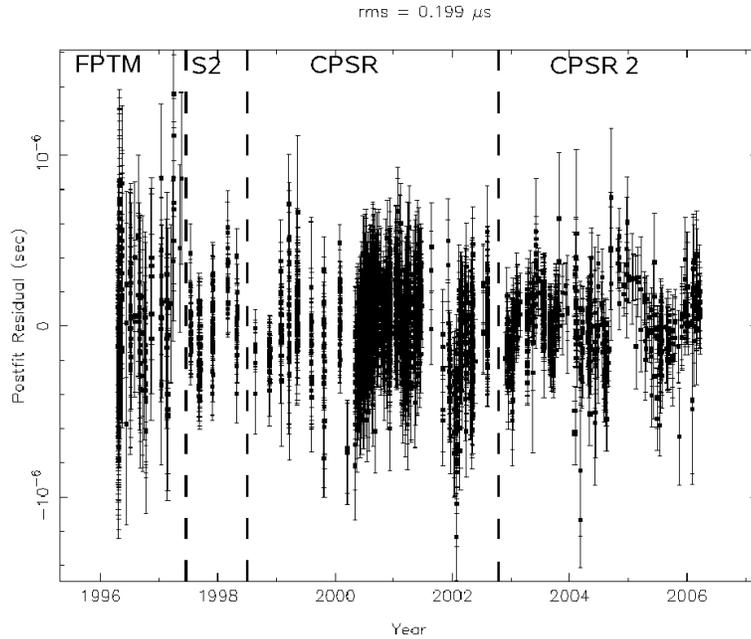
Figure 3.1: Combined 20 cm post-fit timing residuals for new and archival PSR J0437−4715 timing data. Vertical dashed lines separate the different instruments.

The arrival times were analysed using the TEMPO2 pulsar timing software package (Hobbs, Edwards & Manchester 2006; Edwards, Hobbs & Manchester 2006) and consistency with the earlier program, TEMPO, was verified. The timing model (see Table 3.2) is based on the relativistic binary model first derived by Damour & Deruelle (1986) and expanded to contain the geometric orbital terms described by Kopeikin (1995) and Kopeikin (1996) - see also §1.2.4. The model is optimised through a standard weighted least-squares fit in which all parameters are allowed to vary, including all parameters presented in Table 3.2, as well as the unknown time delays between data from different instruments, but excluding the mean value of dispersion measure, which is determined from the simultaneous CPSR2, 64 MHz-wide bands centred at 1341 and 1405 MHz.

A major difference between our implementation of solutions for the orbital angles Ω and i and previous efforts (van Straten et al. 2001; Hotan, Bailes & Ord 2006) is that they were implemented as part of the standard fitting routine. This ensures any covariances between these and other parameters (most importantly the periastron advance and companion mass, see Table 3.2 and Section 3.6) are properly accounted for, thereby yielding a more reliable measurement error. The previous works mentioned above derived these effects from an independent mapping of χ^2 space, leaving the errors of other parameters unaffected.

As can be seen from Figure 3.1, there are significant low-frequency structures present in the timing residual data. Since the standard least-squares fitting routine used in TEMPO2 does not account for the effect of such correlations on parameter

estimation, we performed a Monte-Carlo simulation where data sets with a post-fit power spectrum statistically consistent with that of the PSR J0437−4715 data were used to determine the parameter estimations uncertainties in the presence of realistic low frequency noise. These errors, as well as the factors by which the original errors were underestimated, are shown in Table 3.2. As an example, the distribution of derived pulsar masses from the Monte-Carlo simulation is given in Figure 3.4. Because of the dispersion measure corrections implemented in the final three years of data, one can expect the spectrum of these most precise data points to contain less low-frequency noise than the ten year data set as a whole. We therefore expect the errors resulting from this analysis to be slightly overestimated. Ongoing research into extending the fitting routine with reliable whitening schemes to avoid spectral leakage and hence improve the reliability of the measured parameters, is expected to reduce these errors by factors of around two. All errors given in this paper are those resulting from the Monte-Carlo simulations, unless otherwise stated. The simulations also showed that any biases resulting from the red noise are statistically negligible for the reported parameters. (A full description of this Monte-Carlo technique and the whitening schemes mentioned will be detailed in a future publication.)

Table 3.3: Comparison of DE200 and DE405 results for PSR J0437−4715[a]

Parameter name	DE200 result	DE405 result
Rms residual (ns)	281	199
Relative χ^2	2.01	1.0
Parallax, π (mas)	7.84(7)	6.65 (7)
Parallax distance, D_π (pc)	127.6(11)	150.4(16)
Previously published π (mas)	7.19(14)[c]	6.3(2)[d]
Kinematic distance, D_k (pc)	154.5 (10)	156.0 (10)
D_k corrected for Galactic effects (pc)	155.5 (10)	157.0 (10)
Variation of Newton's gravitational constant, $|\dot{G}/G|$ (10^{-12} yr^{-1}).........	−21.2(22)[b]	−5.0(26)[b]
Total proper motion, μ_{tot} (mas yr^{-1})	140.852(1)	140.915(1)
Companion mass, m_c ($M_\odot$)	0.263(14)	0.254(14)
Pulsar mass, m_{psr} ($M_\odot$)	1.85(15)	1.76(15)
Periastron advance, $\dot{\omega}$ (° yr^{-1})	0.020(4)	0.016(4)
GR prediction of $\dot{\omega}$ (° yr^{-1})	0.0178(9)	0.0172(9)

[a] Numbers in parentheses represent the formal TEMPO2 1σ uncertainty in the last digits quoted, unless otherwise stated.
[b] Given are 2σ errors, i.e. 95% confidence levels.
[c] van Straten et al. (2001)
[d] Hotan, Bailes & Ord (2006)

3.3.3   Solar System Ephemerides

Pulsar timing results are dependent on accurate ephemerides for the Solar System bodies. The results presented in this paper were obtained using the DE405 model (Standish 2004) and, for comparison, selected parameters obtained with the earlier DE200 model are shown in Table 3.3. The greatly reduced χ^2 indicates that the newer Solar System ephemerides are superior to the earlier DE200, reinforcing similar conclusions of other authors (Splaver et al. 2005; Hotan, Bailes & Ord 2006). We notice the parallax value changes by more than $10\,\sigma$ and that the different derived values are closely correlated with the ephemeris used. Although the effect is not as dramatic as it appears because of the under-estimation of the TEMPO2 errors, the fact that the DE405 results agree much better with the more accurate kinematic distance (discussed in the next section), strongly suggests that the differences are due to the ephemeris used and confirms that the DE405 ephemeris is superior. Finally, we note that the DE405 measurement of $\dot\omega$ $(0.016 \pm 0.008\,°\mathrm{yr}^{-1})$ is consistent with the GR prediction for this system $(0.0172 \pm 0.0009\,°\mathrm{yr}^{-1})$.

3.4   Kinematic Distance

As shown in Figure 3.2, the long-term timing history enables precise measurement of the orbital period derivative, $\dot P_\mathrm{b} = (3.73 \pm 0.06) \times 10^{-12}$. This observed value represents a combination of phenomena that are intrinsic to the binary system and dynamical effects that result in both real and apparent accelerations of the binary system along the line of sight (Bell & Bailes 1996); i.e.

$$\dot P_\mathrm{b}^\mathrm{obs} = \dot P_\mathrm{b}^\mathrm{int} + \dot P_\mathrm{b}^\mathrm{Gal} + \dot P_\mathrm{b}^\mathrm{kin} \tag{3.1}$$

where "obs" and "int" refer to the observed and intrinsic values; "Gal" and "kin" are the Galactic and kinematic contributions.

Intrinsic orbital decay is a result of energy loss typically due to effects such as atmospheric drag and tidal dissipation; however, in a neutron star–white dwarf binary system like PSR J0437−4715, energy loss is dominated by quadrupolar gravitational wave emission. For this system, GR predicts (Taylor & Weisberg 1982) $\dot P_\mathrm{b}^\mathrm{GR} = -4.2 \times 10^{-16}$, two orders of magnitude smaller than the uncertainty in the measured value of $\dot P_\mathrm{b}$.

Galactic contributions to the observed orbital period derivative include differential rotation and gravitational acceleration (Damour & Taylor 1991). The differential rotation in the plane of the Galaxy is estimated from the Galactic longitude of the pulsar and the Galactocentric distance and circular velocity of the Sun. Acceleration in the Galactic gravitational potential varies as a function of height above the Galactic plane (Holmberg & Flynn 2004), which may be estimated using the parallax distance and the Galactic latitude of the pulsar. Combining these terms gives $\dot P_\mathrm{b}^\mathrm{Gal} = (-1.8 - 0.5) \times 10^{-14} = -2.3 \times 10^{-14}$, which is of the same order as the current measurement error.
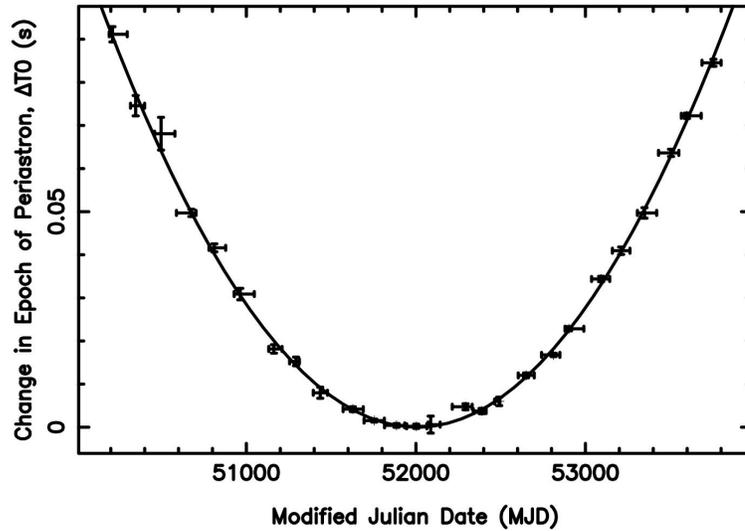
Figure 3.2: Variations in epoch of periastron passage (T_0) due to apparent orbital period increase. A steady increase in orbital period is equivalent to a quadratic increase in T_0 relative to periastron times for a constant orbital period. For this plot, T_0 was measured on data spans of up to 120 days with a model having no orbital period derivative. The formal one-σ measurement errors reported by **Tempo2** are shown by vertical error bars and the epochs over which the measurements were made are shown by horizontal bars. As the mean measurement time was determined through a weighted average of the data contained in the fit, these horizontal bars need not be centred at the mid time associated with the measurement. The parabola shows the effect of the $\dot{P}_{\rm b}$ value obtained from a fit to the data shown in Figure 3.1.
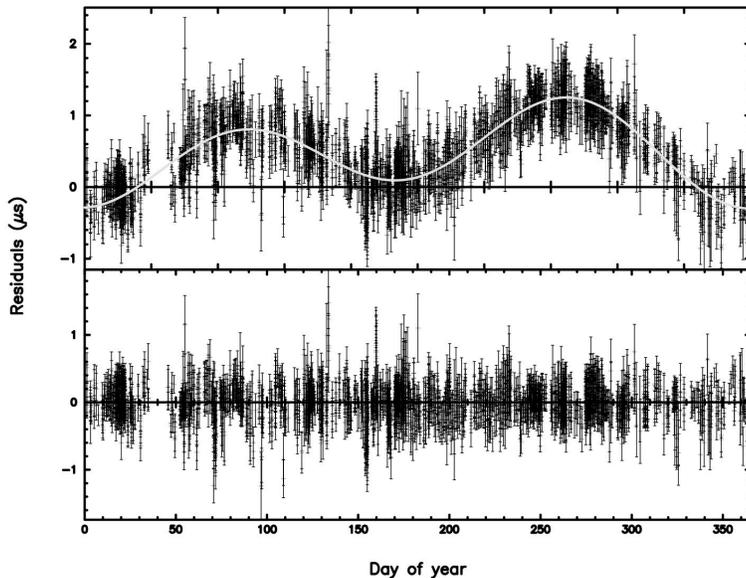
Figure 3.3: Parallax signature of PSR J0437−4715. Top: Timing residuals for PSR J0437−4715 as a function of day of year (starting on 18 November), without parallax but with all remaining parameters at their best-fit values. The smooth curve represents the model fit of a parallax of 6.65 mas. Bottom: The same timing residuals with parallax included in the model. The overall RMS for the top and bottom plots is 524 and 199 ns respectively. The double-humped signature specific to parallax originates from the delay in pulse time-of-arrival (TOA) as the Earth orbits the Sun and samples different parts of the curved wave-front originating at the pulsar.

Given the negligible intrinsic contribution, Equation 3.1 can be simplified and rewritten in terms of the dominant kinematic contribution known as the Shklovskii effect (Shklovskii 1970), an apparent acceleration resulting from the non-linear increase in radial distance as the pulsar moves across the plane perpendicular to the line of sight; quantified by the proper motion, μ and distance D from the Earth:

$$\dot{P}_{\rm b}^{\rm obs} - \dot{P}_{\rm b}^{\rm Gal} \simeq \dot{P}_{\rm b}^{\rm kin} = \frac{\mu^2 D}{c} P_{\rm b}, \qquad (3.2)$$

where c is the vacuum speed of light. Using the measured values of μ, $P_{\rm b}$ and $\dot{P}_{\rm b}$, Equation 3.2 is used to derive the kinematic distance (Bell & Bailes 1996): $D_k = 157.0 \pm 2.4\,{\rm pc}$. This distance is consistent with the one derived from the timing parallax ($D_\pi = 150 \pm 12\,{\rm pc}$ – see also Figure 3.3) and with the VLBI parallax derived for this system: $D_{\rm VLBI} = 156.3 \pm 1.3\,{\rm pc}$ (Deller et al. 2008). Our measurement is, with a relative error of 1.5%, comparable in precision to the best parallax measurements from VLBI (Torres et al. 2007; Deller et al. 2008) and better than typical relative errors provided by the Hipparcos and Hubble space telescopes (Valls-Gabaud 2007).

Given the dependence of parallax distances on ephemerides, as described in Section 3.3.3, it is interesting to note the robustness of $D_{\rm k}$. Also, Table 3.2 shows that

the presence of red noise corrupts the parallax error by a factor of 7.9, whereas $\dot{P}_{\mathrm{b}}$ is only affected by a factor of 2.5. These facts clearly indicate the higher reliability of D_{k} as compared to D_{π}.

3.5 Limits on $\dot{P}_{\mathrm{b}}$ Anomalies: $\dot{G}$ and the Acceleration of the Solar System

Any anomalous orbital period derivative can be constrained by substituting the parallax distance into Equation 2, yielding

$$
\begin{aligned}
\left(\frac{\dot{P}_{\mathrm{b}}}{P_{\mathrm{b}}}\right)^{\mathrm{excess}} &= \left(\dot{P}_{\mathrm{b}}^{\mathrm{obs}} - \dot{P}_{\mathrm{b}}^{\mathrm{Gal}} - \dot{P}_{\mathrm{b}}^{\mathrm{kin}}\right)/P_{\mathrm{b}} \\
&= (3.2 \pm 5.7) \times 10^{-19}\,\mathrm{s}^{-1}.
\end{aligned} \tag{3.3}
$$

in which the error is almost exclusively due to the parallax uncertainty. Following Damour & Taylor (1991), this can be translated into a limit on the time derivative of Newton's gravitational constant (given are 95% confidence levels):

$$
\frac{\dot{G}}{G} = -\frac{1}{2}\left(\frac{\dot{P}_{\mathrm{b}}}{P_{\mathrm{b}}}\right)^{\mathrm{excess}} = (-5 \pm 18) \times 10^{-12}\,\mathrm{yr}^{-1} \tag{3.4}
$$

This limit is of the same order as those previously derived from pulsar timing (see Section 3.2) but have been further improved by Deller et al. (2008) who used the VLBI parallax distance in combination with our $\dot{P}_{\mathrm{b}}$measurement to achieve a better limit still:

$$
\frac{\dot{G}}{G} = (-5 \pm 26) \times 10^{-13}\,\mathrm{yr}^{-1} \tag{3.5}
$$

at 94% certainty. This limit is close to that put by LLR: $(4 \pm 9) \times 10^{-13}$ yr^{-1} (Williams, Turyshev & Boggs 2004). The LLR experiment is based on a complex n–body relativistic model of the planets that incorporates over 140 estimated parameters, such as elastic deformation, rotational dissipation and two tidal dissipation parameters. In contrast, the PSR J0437$-$4715 timing and VLBI results are dependent on a different set of models and assumptions and therefore provide a useful independent confirmation of the LLR result.

A recent investigation into the possible causes of a measured variability of the Astronomical Unit (AU; Krasinsky & Brumberg 2004) has refuted all but two sources of the measured value of $dAU/dt = 0.15 \pm 0.04$ m/yr. Krasinsky & Brumberg (2004) state that the measured linear increase in the AU would be due to either systematic effects or to a time-variation of G at the level of $\dot{G}/G = (-1.0 \pm 0.3) \times 10^{-12}$ yr^{-1}, comparable to, but inconsistent with, the LLR limit.

The anomalous $\dot{P}_{\mathrm{b}}$ measurements of a number of millisecond pulsars have also been used to place limits on the acceleration of the Solar System due to any nearby stars or undetected massive planets (Zakamska & Tremaine 2005). The PSR

J0437−4715 data set limits any anomalous Solar System acceleration to $|a_\odot/c| \leq 1.5 \times 10^{-18}\,\mathrm{s}^{-1}$ in the direction of the pulsar with 95% certainty. This rules out any Jupiter-mass objects at distances less than 117 AU along the line of sight, corresponding to orbital periods of up to 1270 years. Similarly, this analysis excludes any Jupiter-mass planets orbiting PSR J0437−4715 between ∼5 and 117 AU along the line of sight. Zakamska & Tremaine (2005) also compared the sensitivity of this limit to that of optical and infra-red searches for trans-Neptunian objects (TNOs) and concluded that beyond ∼ 300 AU the acceleration limit becomes more sensitive than the alternative searches. At a distance of 300 AU from the Sun, the 95% confidence upper limit on the mass of a possible TNO (in the direction of the pulsar) is 6.8 Jupiter masses. The precise VLBI measurement of parallax mentioned above improves these limits somewhat, as reported in Deller et al. (2008).

3.6   Pulsar Mass

A combination of the mass function and a measurement of the Shapiro delay range can be used to obtain a measurement of the pulsar mass. Using this method, van Straten et al. (2001) derived a mass for PSR J0437−4715 of $1.58 \pm 0.18\,M_\odot$ whereas Hotan, Bailes & Ord (2006) obtained $1.3 \pm 0.2\,M_\odot$. It should be noted, however, that these values resulted from a model that incorporated geometric parameters first described by Kopeikin (1995) and Kopeikin (1996), but covariances between these and other timing parameters (most importantly the companion mass or Shapiro delay range) were not taken into account. Whilst the length of the data sets used by these authors was only a few years, it can also be expected that some spectral leakage from low-frequency noise was unaccounted in the errors of these previously published values. As described in Section 3.3, the Monte-Carlo simulations and extended fitting routines implemented for the results reported in this paper do include these covariances and spectral leakage; it can therefore be claimed that the current estimates (at 68% confidence) of $m_\mathrm{c} = 0.254 \pm 0.018\,M_\odot$ and $m_\mathrm{psr} = 1.76 \pm 0.20\,M_\odot$, for the white dwarf companion and pulsar respectively, reflect the measurement uncertainty more realistically than any previous estimate. The distribution of m_psr that follows from the 5000 Monte-Carlo realisations is shown in Figure 3.4, together with a Gaussian with mean 1.76 and standard deviation 0.20. This demonstrates the symmetric distribution of the pulsar mass likelihood distribution, induced by the precise determination of the orbital inclination angle.

We also note that the new mass measurement of PSR J0437−4715 is the highest obtained for any pulsar to date. Distinction needs to be made between the objective mass estimate presented in this paper and the subjective mass predictions presented in Ransom et al. (2005) and Freire et al. (2008). The pulsar mass confidence interval presented in this paper is derived from the measurement uncertainties of all relevant model parameters, including the well-determined orbital inclination angle, i. In contrast, i is unknown in the Terzan 5 I and J (Ransom et al. 2005) and PSR
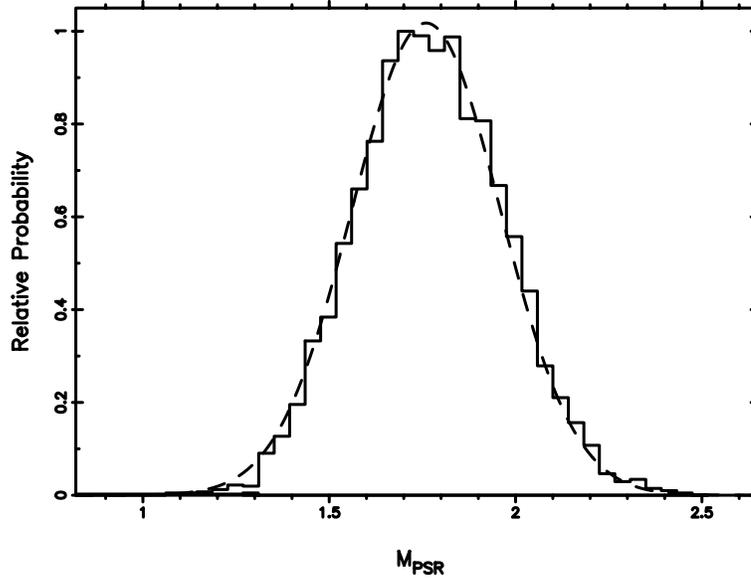
Figure 3.4: Pulsar mass probability distribution. The solid line shows the histogram of 5000 pulsar masses derived from a Monte-Carlo simulation with power spectrum and sampling equal to that of the PSR J0437−4715 data set. The dashed line is a Gaussian distribution with a mean value of $m_{\mathrm{psr}} = 1.76\,M_\odot$ and standard deviation of $0.20\,M_\odot$.

J1748−2021B (Freire et al. 2008) binary systems and the posterior probability intervals for the pulsar masses presented in these works are based upon the prior assumption of a uniform distribution of $\cos i$. These fundamental differences must be accounted for in any subsequent hypothesis testing. Consequently, PSR J0437−4715 is currently the only pulsar to provide reliable constraints on EOSs based on hyperons and Bose-Einstein condensates as described by Lattimer & Prakash (2007). Simulations with TEMPO2 indicate that a forthcoming observational campaign with a new generation of backend systems can be expected to increase the significance of this measurement by another factor of about two in the next few years.

3.7 Conclusions

We have presented results from the highest-precision long-term timing campaign to date. With an overall residual RMS of 199 ns, the 10 years of timing data on PSR J0437−4715 have provided a precise measurement of the orbital period derivative, $\dot{P}_{\mathrm{b}}$, leading to the first accurate kinematic distance to a millisecond pulsar: $D_{\mathrm{k}} = 157.0 \pm 2.4\,\mathrm{pc}$. Application of this method to other pulsars in the future can be expected to improve distance estimates to other binary pulsar systems (Bell & Bailes 1996).

Another analysis based on the $\dot{P}_{\mathrm{b}}$ measurement places a limit on the temporal variation of Newton's gravitational constant. We find a bound comparable to the

best so far derived from pulsar timing: $\dot{G}/G = (-5 \pm 18) \times 10^{-12}\,\mathrm{yr}^{-1}$. A VLBI parallax measurement for this pulsar has further improved this limit, enabling an independent confirmation of the LLR limit.

Previous estimates of the mass of PSR J0437−4715 have been revised upwards to $m_{\mathrm{psr}} = 1.76 \pm 0.20\,M_{\odot}$, which now makes it one of the few pulsars with such a heavy mass measurement. A new generation of backend instruments, dedicated observing campaigns and data prewhitening techniques currently under development should decrease the error in this measurement enough to significantly rule out various EOSs for dense nuclear matter.

Chapter 4

Stability of Millisecond Pulsars and Prospects for Gravitational Wave Detection

[...]regular timing observations of 40 pulsars each with a timing accuracy of 100 ns will be able to make a direct detection of the predicted stochastic background from coalescing black holes within 5 years.
Jenet et al., "Detecting the Stochastic Gravitational Wave Background using Pulsar Timing", The Astrophysical Journal, 2005

This chapter will be submitted to Monthly Notices of the Royal Astronomical Society for publication as Verbiest et al., "On the stability of millisecond pulsars and prospects for gravitational wave detection", in 2009. Minor alterations have been made for the purpose of inclusion in this thesis.

4.1   Abstract

Analysis of high-precision timing observations of an array of $\sim$20 millisecond pulsars (a so-called "timing array") may ultimately result in the detection of a stochastic gravitational wave background (see also §1.3). The overall timing precision achievable using a given telescope and the stability of the pulsars themselves determine the duration of an experiment required to detect a given stochastic background level. We present the first long-term, high-precision timing and stability analysis of a large sample of millisecond pulsars used in gravitational wave detection projects. The resulting pulsar ephemerides are provided for use in future observations. Intrinsic instabilities of the pulsar or the observing system are shown to contribute to timing irregularities only at or below the 100 ns level for our most precisely timed

pulsars. Based on this stability analysis, realistic sensitivity curves for planned and ongoing timing array efforts are determined. We conclude that, given the stability of the investigated millisecond pulsars, prospects for gravitational wave detection within five years to a decade are good for current timing array projects in Australia, Europe and North America and for the South African SKA pathfinder telescope, MeerKAT.

4.2   Introduction

The rotational behaviour of pulsars has long been known to be predictable, especially in the case of MSPs. Current models suggest that such pulsars have been spun up by accretion from their binary companion star to periods of several milliseconds, making them much faster than the more numerous younger pulsars, which typically have periods of seconds (as outlined in §1.1.4). MSPs are generally timed 3-4 orders of magnitude better than normal pulsars and on timescales of several years, it has been shown that some MSPs have a stability comparable to the most precise atomic clocks (Matsakis, Taylor & Eubanks 1997). This intrinsic stability is most clearly quantified through the technique of pulsar timing, which compares arrival times of pulses to a model describing the pulsar, its binary orbit and the ISM between the pulsar and Earth (as described in §1.2 and by Edwards, Hobbs & Manchester 2006). This technique has enabled precise determination of physical parameters at outstanding levels of precision, such as the orbital characteristics of binary star systems (e.g. van Straten et al. 2001), the masses of pulsars and their companions (e.g. Jacoby et al. 2005; Nice 2006) and the turbulent character of the ISM (e.g. You et al. 2007a). The strong gravitational fields of pulsars in binary systems have also enabled outstanding tests of GR and alternative theories of gravity, as described by, e.g., Kramer et al. (2006b) and Bhat, Bailes & Verbiest (2008). Finally, pulsars have provided the first evidence that gravitational waves exist at levels predicted by GR (Taylor & Weisberg 1982) and have placed the strongest limit yet on the existence of a background of gravitational waves (Jenet et al. 2006). It is predicted (most recently by Jenet et al. 2005) that pulsar timing will also enable a direct detection of such a GWB, as fully discussed in §1.3.

A main result that follows from the work of Jenet et al. (2005) is Equation 1.34, replicated below:

$$A_{S=3} \approx 2.3 \times 10^{-12} \frac{\sigma_n}{T^{5/3}\sqrt{N}}, \tag{4.1}$$

where $A_{S=3}$ is the lowest GWB amplitude at which a given PTA achieves a 3σ sensitivity, T is the data span, σ is the typical RMS and N is the number of TOAs. As described in §1.3.4, this results in the standard PTA scenario proposed by Jenet et al. (2005): $N = 250$, $\sigma_n = 0.1\,\mu$s, $T = 5$ years and $M = 20$. However, depending on achievable timing precision of MSPs, an alternative PTA could achieve the same results through timing of 20 MSPs on a biweekly basis for ten years with an RMS of

close to 300 ns. This raises two questions related to the potential of PTAs to detect a GWB. First, down to which precision can MSPs be timed ($\sigma_{\min}$) and second, can high timing precision be maintained over long campaigns (i.e. does $\sigma/T^{5/3}$ decrease with time)?

It has been shown for a few pulsars that timing at a precision of a few hundred nanoseconds is possible for campaigns lasting a few years. Specifically, Hotan, Bailes & Ord (2006) presented a timing RMS of 200 ns over two years of timing on PSRs J1713+0747 and J1939+2134 and 300 ns over two years of timing on PSR J1909−3744; Splaver et al. (2005) reported an RMS of 180 ns on six years of timing on PSR J1713+0747 and Verbiest et al. (2008, also Chapter 3) timed PSR J0437−4715 at 200 ns over ten years. It has, however, not been demonstrated thus far that MSPs can be timed with an RMS residual of ≤ 100 ns over five years or more.

The second question - whether high timing precision can be maintained over ten years or longer, also remains unanswered. Kaspi, Taylor & Ryba (1994) detected excessive low-frequency noise in PSR J1939+2134; Splaver et al. (2005) presented apparent instabilities in long-term timing of PSR J1713+0747 and in Chapter 3, we noted a low-frequency structure in the timing residuals of PSR J0437−4715, but apart from these, no long-term timing of MSPs has been presented to date. Given the high timing precision reported on all three sources, it is unclear how strongly the reported low-frequency noise would affect the use of these pulsars in a GWB detection effort.

In this chapter we present the first high-precision stability analysis for a sample of 20 MSPs, which have been timed for ten years on average. §4.3 describes the source selection, observing systems and data analysis methods used. §4.4 provides the timing models and residual plots for all pulsars in our sample. In accordance with previous publications, we present twice the formal 1σ uncertainties on our parameters, though we defer a full discussion of these timing model parameters and their uncertainties to a later paper. In §4.6 we analyse the stability of two of the most precisely timed MSPs and quantify the different noise sources present in our timing residuals. Specifically, we separate the levels of low-frequency noise, radiometer noise and effects dependent on observing frequency. In §4.7, we use this stability information to calculate sensitivity curves for the ongoing Parkes pulsar timing array (PPTA; Manchester 2008), European pulsar timing array (EPTA; Janssen et al. 2008) and the North American nanohertz observatory for gravitational waves (NANOGrav[1]) projects. We also assess the usefulness of the two square kilometre array (SKA) pathfinder telescopes currently being built (the Australian SKA pathfinder - ASKAP - and the extended Karoo array telescope - MeerKAT) for PTA-type projects. In §4.8 we summarise our results.

---

[1]http://www.nanograv.org

4.3 Observations and Data Reduction

4.3.1 Sample Selection

The data presented in this chapter have been collated from two pulsar timing programmes at the Parkes radio telescope. The oldest of these commenced during the Parkes 70 cm millisecond pulsar survey (Bailes et al. 1994), aiming to characterise properly the astrometric and binary parameters of the MSPs found in the survey. Initial timing results from this campaign were published by Bell et al. (1997) and Toscano et al. (1999). The bright millisecond pulsars PSRs J1713+0747 and B1937+21 (both discovered earlier at Arecibo) were also included in this programme. A few years later, as new discoveries were made in the Swinburne intermediate latitude survey (Edwards et al. 2001), these pulsars were also added, resulting in a total of 16 MSPs that were regularly timed by 2006. Improved timing solutions for these 16 pulsars were presented by Hotan, Bailes & Ord (2006) and Ord et al. (2006).

Besides the projects described above, the PPTA project commenced more regular timing observations of these pulsars in late 2004, expanding the number of MSPs to 20 (listed in Table 4.1) and adding regular monitoring at low observing frequencies (685 MHz) in order to allow correction for variations of the ISM electron density. A detailed analysis of these low frequency observations and ISM effects was recently presented by You et al. (2007a) and an analysis of the combined data on PSR J0437−4715 was presented in Chapter 3. For this pulsar we will use the timing results presented in that chapter; for all other pulsars we will present our improved timing models in §4.4.

4.3.2 Observing Systems

Unless otherwise stated, the data presented were obtained at the Parkes 64 m radio telescope, at a wavelength of 20 cm. Two receivers were used: the H-OH receiver and the 20 cm multibeam receiver (Staveley-Smith et al. 1996b). Over the last five years, observations at 685 MHz were taken with the 10/50 cm coaxial receiver for all pulsars; however, they were only used directly in the final timing analysis of PSR J0613−0200, whose profile displays a sharp spike at this frequency, which can be resolved with coherent dedispersion. For PSRs J1045−4509, J1909−3744 and J1939+2134, the 685 MHz observations were used to model and remove the effects of temporal variations in interstellar dispersion delays and hence included indirectly in the timing analysis.

Three different observing backend systems were used. Firstly, the FPTM (as described in §2.3.5 and by Sandhu et al. 1997; Sandhu 2001), between 1994 and November 2001. Secondly, the 256 MHz bandwidth analogue filterbank (FB) was used in 2002 and 2003. Finally, the CPSR2 back end (see §2.3.5 and Hotan, Bailes & Ord 2006) was used from November 2002 onwards.

Table 4.1: Pulsars in our sample. Column 2 gives the reference for the discovery paper, while column 3 provides references to recent or important publications on timing of the sources. For the three pulsars with original B1950 names, these names are given as footnotes to the J2000.0 names.

Pulsar name	Discovery	Previous timing solution[a]	Pulse period (ms)	Orbital period (d)	Dispersion measure (cm^{-3} pc)
J0437−4715	Johnston et al. (1993)	1, 2	5.8	5.7	2.6
J0613−0200	Lorimer et al. (1995a)	3	3.1	1.2	38.8
J0711−6830	Bailes et al. (1997)	3, 4	5.5	−	18.4
J1022+1001	Camilo et al. (1996)	3	16.5	7.8	10.3
J1024−0719	Bailes et al. (1997)	3	5.2	−	6.5
J1045−4509	Bailes et al. (1994)	3	7.5	4.1	58.2
J1600−3053	Ord et al. (2006)	5	3.6	14.3	52.3
J1603−7202	Lorimer et al. (1996)	3	14.8	6.3	38.0
J1643−1224	Lorimer et al. (1995a)	4	4.6	147.0	62.4
J1713+0747	Foster et al. (1993)	3, 6	4.6	67.8	16.0
J1730−2304	Lorimer et al. (1995a)	4	8.1	−	9.6
J1732−5049	Edwards & Bailes (2001)	7	5.3	5.3	56.8
J1744−1134	Bailes et al. (1997)	3	4.1	−	3.1
J1824−2452[b]	Lyne et al. (1987)	8, 10	3.1	−	120.5
J1857+0943[b]	Segelstein et al. (1986)	3, 9	5.4	12.3	13.3
J1909−3744	Jacoby et al. (2003)	3, 11	2.9	1.5	10.4
J1939+2134[b]	Backer et al. (1982)	3, 9	1.6	−	71.0
J2124−3358	Bailes et al. (1997)	3	4.9	−	4.6
J2129−5721	Lorimer et al. (1996)	3	3.7	6.6	31.9
J2145−0750	Bailes et al. (1994)	3, 12	16.1	6.8	9.0

[a] References: (1) Chapter 3 and Verbiest et al. (2008); (2) van Straten et al. (2001); (3) Hotan, Bailes & Ord (2006); (4) Toscano et al. (1999); (5) Ord et al. (2006); (6) Splaver et al. (2005); (7) Edwards & Bailes (2001); (8) Hobbs et al. (2004); (9) Kaspi, Taylor & Ryba (1994); (10) Cognard & Backer (2004); (11) Jacoby et al. (2005); (12) Löhmer et al. (2004)

[b] PSRs J1824−2452, J1857+0943 and J1939+2134 are also known under their B-names: PSRs B1821−24, B1855+09 and B1937+21, respectively.
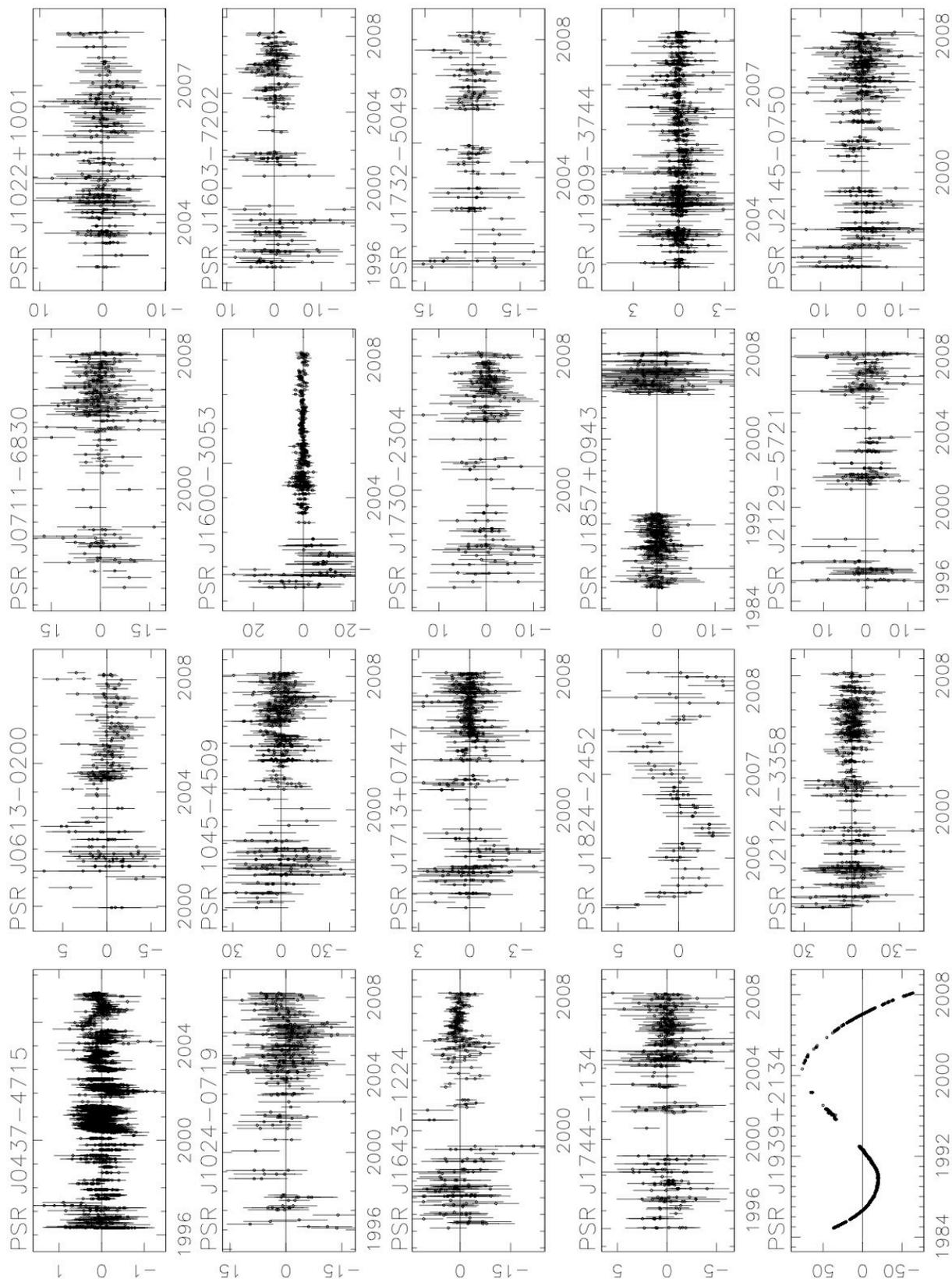
Figure 4.1: Timing residuals of the 20 pulsars in our sample. Scaling on the x-axis is in years and on the y-axis in μs. For PSRs J1857+0943 and J1939+2134, these plots include the Arecibo data made publically available by Kaspi, Taylor & Ryba (1994); all other data are from Parkes, as described in §4.3. Sudden changes in white noise levels are due to changes in pulsar backend set-up - see §4.3 for more details.

4.3.3 Arrival Time Estimation

The processing applied differs for data from different observing backends. The FPTM data were calibrated using a real-time system to produce either two or four Stokes parameters which were later combined into Stokes I. The FB data were produced from a search system with no polarimetric calibration possible. This system produced Stokes I profiles after folding 1-bit data. Data from both of these systems were integrated in frequency and time to produce a single profile for each observation. These observations were ∼25 minutes in duration. For CPSR2 data, in order to minimise the effects of aliasing and spectral leakage, 12.5% of each edge of the bandpass was removed. To remove the worst radio frequency interference, any frequency channel with power more than 4σ in excess of the local median was also removed ("local" was defined as the nearest 21 channels and the standard deviation σ was determined iteratively). CPSR2 also operated a total power monitor on microsecond timescales, which removed most impulsive interference.

The CPSR2 data were next integrated for five minutes and calibrated for differential gain and phase to correct for possible asymmetries in the receiver hardware. If calibrator observations were available (especially in the years directly following the CPSR2 commissioning, observations of a pulsating noise source, needed for polarimetric calibration, were not part of the standard observing schedule). Subsequently the data were integrated for the duration of the observation, which was typically 32 minutes for PSRs J2124−3358, J1939+2134 and J1857+0943 and 64 minutes for all other pulsars. In the case of PSR J1643−1224, the integration time was 32 minutes until December 2005 and 64 minutes from 2006 onwards. Finally, the CPSR2 data were integrated in frequency and the Stokes parameters were combined into total power. CPSR2 data that did not have calibrator observations available were processed identically, except for the calibration step. While for some pulsars (like PSR J0437−4715) these uncalibrated data are provably of inferior quality (see, e.g. van Straten 2006), in our case this is largely outweighed by the improved statistics of the larger number of TOAs and by the extended timing baseline these observations provided. We therefore include both calibrated and uncalibrated observations in our data sets.

To obtain pulse TOAs, the total intensity profiles thus obtained were cross-correlated with pulsar and frequency-dependent template profiles. These template profiles were created through addition of a large number of observations and were phase-aligned for both CPSR2 observing bands. As there were only few high signal-to-noise observations obtained with the FPTM and FB backends for most pulsars, these data were timed against standards created with the CPSR2 backend. This may affect the reliability of their derived TOA errors. For this reason we have evaluated the underestimation of TOA errors for each backend separately. We note that these factors do not vary much with backend, which indicates that the application of the CPSR2 templates to the FB and FPTM data does not affect the timing significantly. While the TOA errors were generally determined through the standard

Fourier phase gradient method, the Gaussian interpolation method produced more precise estimates for pulsars with low signal-to-noise ratios (Hotan, Bailes & Ord 2005) - specifically for PSRs J0613−0200, J2129−5721, J1732−5049, J2124−3358 and J1045−4509. The PSRCHIVE software package (Hotan, van Straten & Manchester 2004) was used to perform all of the processing described above.

4.4   Timing Results

The TEMPO2 software package (Hobbs, Edwards & Manchester 2006) was used to calculate the residuals from the TOAs and initial timing solutions (Table 4.1). In order to account for the unknown instrumental delays and pulsar-dependent differences in observing setup, arbitrary phase-offsets between the backends were introduced. Where available, data at an observing frequency of 685 MHz were included in an initial fit to inspect visually the presence of DM variations. In the case of PSRs J1045−4509, J1909−3744, J1939+2134 and J0437−4715, such variations were obviously and dealt with in the timing software through a method similar to that presented by You et al. (2007a). We updated all the pulsar ephemerides to use International Atomic Time (implemented as TT(TAI) in TEMPO2) and the DE405 Solar System ephemerides (Standish 2004). In order to achieve a reduced χ^2 value of close to unity, the TOA errors were multiplied by backend and pulsar-dependent error factors which were generally close to unity. A summary of the lengths of the data sets and the achieved timing precision can be found in Table 4.2, highlighting the superior timing precision of PSRs J1909−3744, J0437−4715 and J1713+0747 when compared to other pulsars. While the residual RMS has been an oft-quoted measure of data quality, it does not take the density of observations into account and can therefore be misleading. We hence introduce the concept of the "normalised RMS" (column 5 of Table 4.2), which is the theoretical RMS one would get by averaging all TOAs within a year:

$$\sigma_{\mathrm{Norm}} = \frac{\sigma}{\sqrt{NT/T_0}}, \tag{4.2}$$

with σ the RMS of the timing residuals, N the number of TOAs and T the time span, normalised by $T_0 = 1\,\mathrm{yr}$. For comparison of data sets from different projects or telescopes the normalised RMS provides a more objective measure of data quality than the residual RMS. We therefore encourage future authors to use this statistic instead.

The timing residuals for our data sets are presented in Figure 4.1 and the timing models are presented in tables 4.3, 4.4, 4.5, 4.6, 4.7 and 4.8. While several parameters are listed that have not previously been published, the analysis by Verbiest et al. (2008) has demonstrated the unreliability of parameter uncertainties resulting from standard pulsar timing techniques, especially in the presence of (even small amounts of) low-frequency noise. The focus of this present paper is on the overall pulsar stability and implications for pulsar timing array science, we therefore defer

the discussion of these new astrometric parameters - along with a reliable analysis of the parameter uncertainties - to a later paper. However, we encourage observers to use the improved models when observing. We also note that all but a few of the parameters in our timing models are consistent with those published previously.

Table 4.2: Summary of the timing results, sorted in order of decreasing timing precision. The columns present the pulsar name, the RMS of the timing residuals, the length of the data set, the number of TOAs, the normalised RMS, the second period derivative (which is not contained in our timing models, but determined independently as a measure of stability) and the stability parameter Δ_8. For $\ddot{\nu}$, the numbers in brackets represent twice the formal $1\,\sigma$ errors in the last digit quoted. See §4.4 and §4.6 for details.

Pulsar name	rms (μs)	T (yr)	N_{pts}	Norm. rms (ns)	$\ddot{\nu}$ $(10^{-27}\,\mathrm{s}^{-1})$	Δ_8
J1909−3744	0. 166	5.2	893	13	1.1(4)	−5.51
J0437−4715	0. 199	9.9	2847	12	−0.23(4)	−5.79
J1713+0747	0. 204	14.0	392	39	−0.01(3)	< −4.93
J1939+2134	0. 576	12.5	180	152	4.3(9)	−4.58
J1744−1134	0. 614	13.2	342	121	0.03(16)	< −4.66
J1600−3053	1. 14	6.8	477	136	1.4(28)	< −4.85
J0613−0200	1. 54	8.2	190	320	−6.1(22)	< −4.56
J1824−2452	1. 62	2.8	89	287	200.0(540)	−$^{\mathrm{a}}$
J1022+1001	1. 63	5.1	260	228	−3.3(12)	< −4.85
J2145−0750	1. 81	13.8	377	346	0.093(89)	< −4.34
J1603−7202	1. 95	12.4	212	472	0.5(2)	< −4.06
J2129−5721	2. 20	12.5	179	581	0.85(92)	< −3.48
J1643−1224	2. 51	14.0	241	605	1.2(7)	−3.82
J1730−2304	2. 51	14.0	180	700	0.08(39)	< −3.95
J1857+0943	2. 91	3.9	106	558	−7.0(230)	< −4.39
J0711−6830	3. 24	14.2	227	810	0.2(6)	< −4.00
J1732−5049	3. 24	6.8	129	744	6.2(62)	−4.07
J2124−3358	4. 03	13.8	416	925	0.01(61)	< −4.14
J1024−0719	4. 20	12.1	269	891	−3.3(10)	< −3.93
J1045−4509	6. 64	14.1	401	1251	1.5(6)	< −3.76

$^{\mathrm{a}}$ The CPSR2 data on PSR J1824−2452 are only 2.8 years long so insufficient data are available to determine a Δ_8 parameter.

Table 4.3: Timing parameters for the single pulsars, PSRs J0711−6830, J1024−0719, J1730−2304 and J1744−1134. Numbers in brackets give twice the formal 1σ uncertainty in the last digit quoted. Note that these parameters are determined using Tempo2, which uses the International Celestial Reference System and Barycentric Coordinate Time. As a result this timing model must be modified before being used with an observing system that inputs Tempo format parameters. See Hobbs, Edwards & Manchester (2006) for more information.

Pulsar name............	J0711−6830	J1024−0719	J1730−2304	J1744−1134
		Fit and data-set parameters		
MJD range...........	49373.6−54546.4	50117.5−54544.6	49421.9−54544.8	49729.1−54546.9
Number of TOAs.........	227	269	180	342
RMS timing residual (μs) .	3.24	4.20	2.51	0.614
Reference epoch for P, α, δ and DM determination .	49800	53000	53300	53742
		Measured Quantities		
Right ascension, α (J2000.0).............	07:11:54.22579(15)	10:24:38.68849(4)	17:30:21.6612(3)	17:44:29.403209(4)
Declination, δ (J2000.0) ...	−68:30:47.5989(7)	−07:19:19.1696(11)	−23:04:31.28(7)	−11:34:54.6606(2)
Proper motion in α, $\mu_\alpha \cos\delta$ (mas yr^{-1})	−15.55(9)	−35.5(2)	20.27(6)	18.804(15)
Proper motion in δ, μ_δ (mas yr^{-1})	14.23(7)	−48.6(3)	–	−9.40(6)
Annual parallax, π (mas)	–	–	–	2.4(2)
Dispersion measure, DM (cm^{-3} pc)........	18.408(4)	6.486(4)	9.618(2)	3.1380(6)
Pulse frequency, ν (Hz) ...	182.117234869347(4)	193.715683568727(3)	123.110287192301(2)	245.4261197483027(5)
Pulse frequency derivative, $\dot\nu$ (10^{-16} s^{-2})...........	−4.94406(15)	−6.9508(3)	-3.05907(11)	-5.38188(4)

Table 4.4: Timing parameters for the single pulsars, PSRs J1824−2452, J1939+2134 and J2124−3358. See caption of Table 4.3 for more information.

Pulsar name	J1824−2452	J1939+2134	J2124−3358
	Fit and data-set parameters		
MJD range	53518.8−54544.9	49956.5−54526.9	49489.9−54528.9
Number of TOAs	89	180	416
RMS timing residual (μs)	0.990	0.576	4.03
Reference epoch for P, α, δ and DM determination	54219	52601	53174
	Measured Quantities		
Right ascension, α (J2000.0)	18:24:32.00797(5)	19:39:38.561286(7)	21:24:43.85347(3)
Declination, δ (J2000.0)	−24:52:10.824(13)	+21:34:59.12913(15)	−33:58:44.6667(7)
Proper motion in α, $\mu_\alpha \cos\delta$ (mas yr^{-1})	0.1(7)	0.13(3)	−14.12(13)
Proper motion in δ, μ_δ (mas yr^{-1})	−11(15)	−0.25(5)	−50.34(25)
Annual parallax, π (mas)	–	0.4(4)	3.1(11)
Dispersion measure, DM (cm^{-3} pc)	120.502(3)	71.0227(9)	4.601(3)
Pulse frequency, ν (Hz)	327.405594693013(7)	641.928233559522(5)	202.793893879496(2)
Pulse frequency derivative, $\dot\nu$ (10^{-16} s^{-2})	−1735.291(4)	−433.1100(5)	−8.4597(2)
Second frequency derivative, $\ddot\nu$ (s^{-3})	−2.0(19)	–	–
Third frequency derivative, $\dddot\nu$ (s^{-4})	−2.6(12)	–	–

Table 4.5: Timing parameters for binary PSRs J0613−0200, J1045−4509 and J1643−1224. See caption of table 4.3 for more information.

Fit and data-set parameters	J0613−0200	J1045−4509	J1643−1224
Pulsar name	J0613−0200	J1045−4509	J1643−1224
MJD range	51526.6−54527.3	49405.5−54544.5	49421.8−54544.7
Number of TOAs	190	401	241
RMS timing residual (μs)	1.54	6.64	2.51
Reference epoch for P, α, δ and DM determination	53114	53050	49524
Measured Quantities			
Right ascension, α (J2000.0)	06:13:43.975142(11)	10:45:50.18951(5)	16:43:38.15543(8)
Declination, δ (J2000.0)	−02:00:47.1737(4)	−45:09:54.1427(5)	−12:24:58.735(5)
Proper motion in α, $\mu_\alpha \cos\delta$ (mas yr^{-1}) .	1.85(7)	−6.0(2)	6.0(1)
Proper motion in δ, μ_δ (mas yr^{-1})	−10.6(2)	5.3(2)	4.2(4)
Annual parallax, π (mas)	0.8(7)	3.3(38)	1.6(9)
Dispersion measure, DM (cm^{-3} pc) . . .	38.782(4)	58.137(6)	62.410(3)
Pulse frequency, ν (Hz)	326.600562190182(4)	133.793149594456(2)	216.373337551615(7)
Pulse frequency derivative, $\dot\nu$ (10^{-16} s^{-2})	−10.2307(7)	−3.1613(3)	−8.6439(2)
Orbital period, P_b (days)	1.1985125753(1)	4.0835292547(9)	147.01739776(6)
Epoch of periastron passage, T_0 (MJD) .	53113.98(2)	53048.98(2)	49577.969(2)
Projected semi-major axis, $x = a\sin i$ (s)	1.0914444(3)	3.0151325(10)	25.072614(2)
$\dot x$ (10^{-14})	−	−	−4.9(6)
Longitude of periastron, ω_0 (deg)	54(6)	242.7(16)	321.850(4)
Orbital eccentricity, e (10^{-5})	0.55(6)	2.37(7)	50.579(4)

Table 4.6: Timing parameters for binary PSRs J1022+1001, J1600−3053 and J1857+0943. See caption of Table 4.3 for more information.

	J1022+1001	J1600−3053	J1857+0943
	Fit and data-set parameters		
MJD range	52649.7−54528.5	52055.7−54544.6	53086.9−54526.9
Number of TOAs	260	477	106
RMS timing residual (μs)	1.63	1.14	2.91
Reference epoch for P, α, δ and DM determination	53589	53283	53806
	Measured Quantities		
Right ascension, α (J2000.0)	10:22:58.003(3)	16:00:51.903798(12)	18:57:36.39129(4)
Declination, δ (J2000.0)	+10:01:52.76(13)	−30:53:49.3407(5)	+09:43:17.225(1)
Proper motion in α, $\mu_\alpha \cos\delta$ (mas yr^{-1})	−17.02(14)	−1.06(9)	−2.4(5)
Proper motion in δ, μ_δ (mas yr^{-1})	–	−7.1(3)	−5.7(9)
Annual parallax, π (mas)	1.8(6)	0.2(3)	2.8(23)
Dispersion measure, DM (cm^{-3} pc)	10.261(2)	52.3262(10)	13.286(7)
Pulse frequency, ν (Hz)	60.779447976215(4)	277.937707098492(17)	186.494078441977(5)
Pulse frequency derivative, $\dot\nu$ (10^{-16} s^{-2})	−1.6012(2)	−7.3390(5)	−6.204(3)
Orbital period, P_b (days)	7.8051302826(4)	14.3484577709(13)	12.32717138(7)
Epoch of periastron passage, T_0 (MJD)	53587.3140(6)	53281.191(4)	53804.442(22)
Projected semi-major axis, $x = a\sin i$ (s)	16.7654074(4)	8.801652(10)	9.230778(4)
$\dot x$ (10^{-14})	1.5(10)	−0.4(4)	–
Longitude of periastron, ω_0 (deg)	97.75(3)	181.85(10)	276.8(6)
Orbital eccentricity, e (10^{-5})	9.700(4)	17.369(4)	2.21(4)
Sine of inclination angle, $\sin i$	0.73^2	0.8(4)	0.997(5)
Inclination angle, i (deg)	47^2	–	–
Companion mass, M_c ($M_\odot$)	1.05^2	0.6(15)	0.42(24)

^{2}From Hotan, Bailes & Ord (2006)

Table 4.7: Timing parameters for binary PSRs J1603−7202, J1732−5049 and J1909−3744. See caption of Table 4.3 for more information.

	Fit and data-set parameters		
Pulsar name	J1603−7202	J1732−5049	J1909−3744
MJD range	50026.1−54544.7	52056.8−54544.8	52618.4−54528.8
Number of TOAs	212	129	893
RMS timing residual (μs)	1.95	3.24	0.166
Reference epoch for P, α, δ and DM determination	53024	53300	53631
	Measured Quantities		
Right ascension, α (J2000.0)	16:03:35.67980(4)	17:32:47.76686(4)	19:09:47.4366120(8)
Declination, δ (J2000.0)	−72:02:32.6985(3)	−50:49:00.1576(11)	−37:44:14.38013(3)
Proper motion in α, $\mu_\alpha \cos\delta$ (mas yr^{-1})	−2.52(6)	—	−9.510(7)
Proper motion in δ, μ_δ (mas yr^{-1})	−7.42(9)	−9.3(7)	−35.859(19)
Annual parallax, π (mas)	—	—	0.79(4)
Dispersion measure, DM (cm^{-3} pc)	38.060(2)	56.822(6)	10.3934(2)
Pulse frequency, ν (Hz)	67.3765811408911(5)	188.2335122654 37(3)	339.3156874094 9071(10)
Pulse frequency derivative, $\dot\nu$ (10^{-16} s^{-2})	-0.70952(5)	-5.0338(12)	-16.14819(5)
Orbital period, $P_{\rm b}$ (days)	6.3086296703(7)	5.262997206(13)	1.533449474590(6)
Orbital period derivative, $\dot P_{\rm b}$ (10^{-13})	—	—	5.5(3)
Projected semi-major axis, $x = a \sin i$ (s)	6.8806610(4)	3.9828705(9)	1.89799106(7)
$\dot x$ (10^{-14})	1.8(5)	—	−0.05(4)
$\kappa = e\sin\omega_0$ (10^{-6})	1.61(14)	2.20(5)	−0.4(4)
$\eta = e\cos\omega_0$ (10^{-6})	−9.41(13)	−8.4(4)	−13(2)
Ascending node passage, $T_{\rm asc}$ (MJD)	53309.3307830(1)	51396.366124(2)	53630.7232148 94(4)
Sine of inclination angle, $\sin i$	—	—	0.9980(2)
Companion mass, $M_{\rm c}$ ($M_\odot$)	—	—	0.212(4)

Table 4.8: Timing parameters for binary PSRs J1713+0747, J2129−5721 and J2145−0750. See caption of Table 4.3 for more information.

Pulsar name	Fit and data-set parameters		
	J1713+0747	J2129−5721	J2145−0750
MJD range	49421.9−54546.8	49987.4 −54547.1	49517.8−54547.1
Number of TOAs	392	179	377
RMS timing residual (μs)	0.204	2.20	1.81
Reference epoch for P, α, δ and DM determination	54312	54000	53040
	Measured Quantities		
Right ascension, α (J2000.0)	17:13:49.532628(2)	21:29:22.76533(5)	21:45:50.46412(3)
Declination, δ (J2000.0)	+07:47:37.50165(6)	−57:21:14.1981(4)	−07:50:18.4399(13)
Proper motion in α, $\mu_\alpha \cos\delta$ (mas yr^{-1})	4.923(10)	9.35(10)	−9.67(15)
Proper motion in δ, μ_δ (mas yr^{-1})	−3.85(2)	−9.47(10)	−8.8(4)
Annual parallax, π (mas)	0.94(11)	1.9(17)	1.5(5)
Dispersion measure, DM (cm^{-3} pc)	15.9915(2)	31.853(4)	8.9979(14)
Pulse frequency, ν (Hz)	218.8118404414362(3)	268.359227423608(3)	62.295887856965(6)
Pulse frequency derivative, $\dot\nu$ (10^{-16} s^{-2})	−4.08379(3)	-15.0179(2)	-1.15588(3)
Orbital period, P_{b} (days)	67.825130964(16)	6.625493093(1)	6.83892(2)
Orbital period derivative, $\dot{P}_{\mathrm{b}}$ (10^{-13})	41(20)	—	4(3)
Epoch of periastron passage, T_0 (MJD)	54303.6328(8)	53997.52(3)	53042.431(3)
Projected semi-major axis, $x = a\sin i$ (s)	32.3424236(3)	3.5005674(7)	10.1641080(3)
$\dot{x}$ (10^{-14})	—	1.1(6)	−0.28(33)
Longitude of periastron, ω_0 (deg)	176.190(4)	196.3(15)	200.63(17)
Orbital eccentricity, e (10^{-5})	7.4940(3)	1.21(3)	1.930(6)
Periastron advance, $\dot\omega$ (deg/yr)	—	—	0.06(6)
Inclination angle, i (deg)	78.5(18)	—	—
Companion mass, M_{c} ($M_\odot$)	0.20(2)	—	—
Longitude of ascending node, Ω (deg)	68(17)	—	—

4.5   Quantifying Low-Frequency Noise

In this Section, we determine some standard stability measures for our data sets, to allow comparison with previous publications. The first of these measures is the second time derivative of the spin frequency. Since pulse frequency, ν, and frequency derivative, $\dot{\nu}$, are fitted as part of the timing model, a quadratic functional form is effectively removed from the timing residuals. The effect of any low-frequency process is therefore best characterised by a cubic polynomial, as is clearly seen in the timing residuals of PSR J1939+2134 in Figure 4.1. In order to quantify the size of this instability, a second derivative of the pulsar spin frequency with respect to time, $\ddot{\nu}$, can be fitted. The $\ddot{\nu}$ values for all 20 MSPs of our sample are presented in column six of Table 4.2. While the clear low-frequency noise of PSRs J1939+2134 and J1824−2452 results in significant, high values of $\ddot{\nu}$, the insignificance of the measurement for the remaining pulsars renders this parameter ineffective for comparative purposes.

The fact that $\ddot{\nu}$ effectively characterises the stability of the data set on timescales of the data length, which differs between data sets, further reduces the usefulness of this parameter. A partial solution to this problem was presented by Arzoumanian et al. (1994) who introduced the Δ_8 parameter, which is proportional to the logarithm of the average $|\ddot{\nu}|/\nu$ value measured over a time span of 10^8 seconds (~ 3.16 years). The Δ_8 parameters for our data are presented in column seven of Table 4.2. As Δ_8 measures stability on a given timescale, it provides a more straightforward comparison between pulsars.

While Δ_8 is of interest for comparison with previous publications and as an initial measure of timing stability, a full analysis at varying timescales requires a power spectrum. Because of various pulsar timing-specific issues such as clustering of data, large gaps in data and large variations in error bar size, however, standard spectral analysis methods fail to provide reliable results. An alternative is provided by the σ_z statistic, as described by Matsakis, Taylor & Eubanks (1997). The interpretation of this statistic - plotted as a function of timescale in Figure 4.2 - requires some attention. As presented by Matsakis, Taylor & Eubanks (1997), a power spectrum with spectral index β:

$$P(\nu) \propto f^{\beta}$$

would translate into a σ_z curve:

$$\sigma_z^2(\tau) \propto \tau^{\mu}$$

where the spectral indices are related as:

$$\mu = \begin{cases} -(\beta + 3) & \text{if } \beta < 1 \\ -4 & \text{otherwise.} \end{cases} \tag{4.3}$$

This implies that spectra have different slopes in a σ_z graph than in a power spectrum. Figure 4.2 provides some examples for guidance: lines with a slope of $-3/2$

represent spectrally white data and a GWB with a spectral index $\alpha = -2/3$ in the gravitational strain spectrum, would have a positive slope of 2/3 in σ_z.

Figure 4.2 clearly reveals the scale-dependent stability of PSR J1939+2134: this pulsar is stable at sub-microsecond levels on short timescales, but experiences a turnover on a timescale of ~ 2 years, indicating poorer stability. PSR J1824−2452 shows similar behaviour, with microsecond precision at timescales below one year and increases at larger scales. Our longest high-precision data set, on PSR J1713+0747, shows constant levels of stability up to 14 years, which contradicts the analysis of Splaver et al. (2005).

Overall, six pulsars show signs of a turnover or flattening off like PSR J1939+2134. These six are PSRs J0613−0200, J1022+1001, J1024−0719, J1045−4509, J1824−2452 and J1939+2134 itself. The σ_z graphs for the 14 remaining pulsars all show consistency with a white noise slope, implying stability at the level of the residual RMS over all timescales shorter than the time span of our data. While the graph for PSR J0437−4715 displays a slope slightly less steep than that expected for pure white noise, this excess of low-frequency noise (first discussed in Chapter 3 and by Verbiest et al. 2008) is not strong enough to affect its usefulness for GWB detection efforts since a GWB is expected to induce a much steeper slope.

In summary, the σ_z graphs demonstrate that most of the MSPs investigated in this analysis will prove useful in PTA projects, provided the RMS is reduced and/or the stability is maintained over longer time spans. Whilst stability on longer timescales cannot be analysed without continued observing, the following sections will assess the prospects for reduction of the residual RMS.

4.6   Timing Precision Analysis

For pulsar timing arrays to detect gravitational waves successfully, MSPs must both be stable over long timescales and be able to be timed with high precision. In the previous section, we have analysed some standard stability measures for our data sets. In this section, we will break down the timing RMS, σ_{Tot}, into various components in order to achieve an upper limit on intrinsic timing noise and therefore on the ultimate timing precision of MSPs[3]. In §4.6.1, we will estimate the level of radiometer noise, σ_{Rad}, in our timing. A new measure which we dub "the sub-band timing measure", σ_{sb}, will be introduced in §4.6.2; this new measure eliminates many systematic effects to provide an indicator of theoretical precision. In §4.6.3, we discuss how these estimates can be used to provide a simple upper limit on the precision with which MSPs may be timed. Because the timing of most pulsars in our sample is strongly dominated by radiometer noise, we will perform this analysis

---

[3]Since it is known that intrinsic timing noise differs strongly from pulsar to pulsar (see, e.g. 4.5), the upper limit we derive in this section will not necessarily hold for any MSPs that aren't included in this analysis. However, since this limit will imply that there is no inherent reason why MSPs would always time worse, we assume pulsar searches will discover MSPs with timing properties comparable to those of the pulsars investigated here.
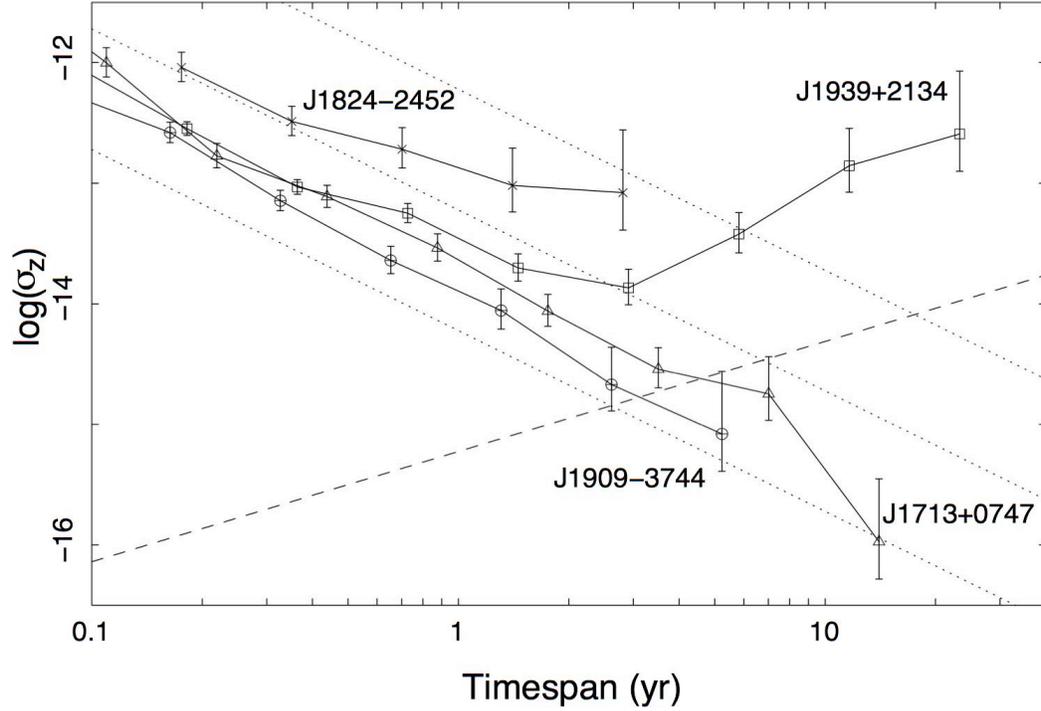
Figure 4.2: σ_z stability parameter for the two most unstable (PSR J1939+2134: squares; PSR J1824−2452: crosses) and two of the most stable pulsars in our sample (PSR J1909−3744: circled plusses; PSR J1713+0747: triangles), against timescale. The dotted slanted lines represent white noise levels of (bottom to top) 100 ns, 1 μs and 10 μs; the dashed slanted line shows the steepness introduced by a hypothetical GWB (see §4.2); pulsars whose curve is steeper than this line (like PSR J1939+2134), can therefore be expected to be of little use to PTA efforts. The specific line plotted here is for a GWB with $\Omega_{\mathrm{gw}}h^2 = 10^{-9}$ and $\alpha = -1$ (i.e. $A = 1.26 \times 10^{-15}$). However, since this theoretical effect disregards sampling and model fitting effects, a bound on the GWB amplitude cannot be directly derived from this graph. To fully account for such effects, a method based on simulations of the GWB is presented in Chapter 5.
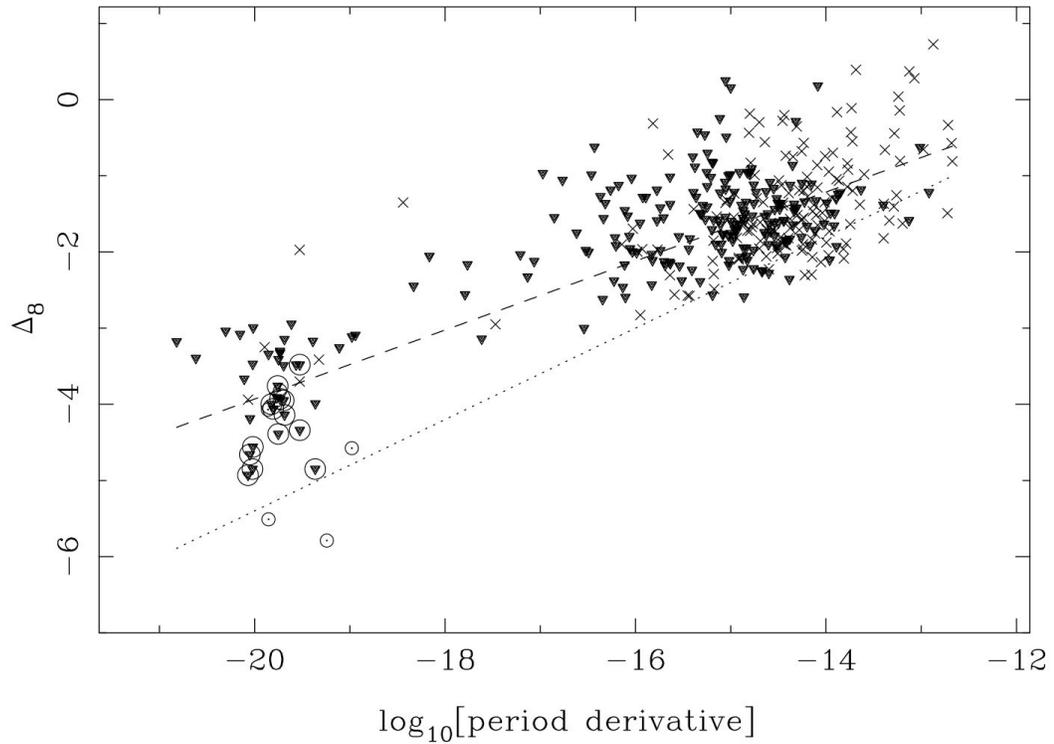
Figure 4.3: Δ_8 **stability parameter for a combination of the data presented in this paper (circled dots and triangles) and in the upcoming Hobbs, Lyne & Kramer (2009; crosses and non-circled triangles). Inverted triangles present upper limits, crosses and dots show actual measured values. The dotted line corresponds to** $\Delta_8 = 6.6 + 0.6 \log \dot{P}$ **as obtained by Arzoumanian** et al. **(1994). Hobbs et al. (2009) suggest that this is low and obtain** $\Delta_8 = 5.1 + 0.5 \log \dot{P}$ **(dashed line) instead.**

Table 4.9: Breakdown of weighted timing residuals for three selected pulsars. The timing RMS (σ_{Tot}) is the RMS of the CPSR2 timing residuals; the sub-band RMS (σ_{sb}) is the RMS of the offset between the two frequency bands of the CPSR2 backend (divided by $\sqrt{2}$) and the radiometer limit (σ_{Rad}) is the theoretical prediction of the timing precision, assuming that only radiometer noise is present in the data. The temporal and frequency components (σ_τ and σ_ν respectively), are derived from the previous three quantities, as described in §4.6.2.

Pulsar name	σ_{Tot} (ns)	σ_{sb} (ns)	σ_{Rad} (ns)	σ_τ (ns)	σ_ν (ns)
J1909$-$3744	166	144	131	83	60
J1713$+$0747	170	149	105	82	106
J1939$+$2134	283	124	64	254	106

only on two of the most precisely timed pulsars, PSRs J1909$-$3744 and J1713$+$0747, as well as on the most clearly unstable pulsar, PSR J1939$+$2134. Also, given the large variation of systematic effects one can expect for the different backends, this analysis will be based only on the Parkes CPSR2 data, which implies that only effects on timescales of five years or less will be estimated. While a full analysis of lower spectral frequencies may be of interest in itself, for our purpose of PTA feasibility assessment a five year timescale is sufficient, as will be demonstrated in §4.7.

4.6.1 Theoretical Estimation of Radiometer-Limited Precision

The receiver noise present in pulsar timing data can be reduced through longer observations, larger bandwidth or larger telescopes. The larger bandwidth of new pulsar instrumentation will therefore reduce this noise in future data. Considering timing projects worldwide, the larger effective collecting area of several telescopes with respect to Parkes will further limit the radiometer noise present in future data sets. The advantage of these improved technologies and larger telescopes, will be determined by the proportion of our timing precision caused by this source of noise. The amount of radiometer noise present in the timing residuals can be determined based on the pulsar's observed pulsar profile shape and brightness. Equation (13) of van Straten (2006) provides the following measure (notice we only consider the total intensity, S_0, to allow direct comparison with our timing results):

$$\sigma = P \times \sqrt{V} = P \times \left(4\pi^2 \sum_{m=1}^{N_{\text{max}} \leq N/2} \nu_{\text{m}}^2 \frac{S_{0,\text{m}}^2}{\varsigma_0^2} \right)^{-0.5}, \qquad (4.4)$$

where ν_{m} is the mth frequency of the Fourier transform of the pulse profile, $S_{0,\text{m}}^2$ is the total power at that frequency, ς_0 is the white noise variance of the profile under

consideration, N is the total number of time bins across the profile and N_{max} is the frequency bin where the Fourier transform of the pulse profile reaches the white noise level, ς_0. V is the expected variance in the phase-offset or residual, P is the pulse period and σ is the residual RMS predicted for the input pulse profile.

Applying this equation to the CPSR2 observations used in our timing, provides a measure of the expected timing precision, assuming that only radiometer noise affects hourly integrations. This measure is listed in column 4 of Table 4.9 for the three pulsars considered. The consistency of these values with the formal errors resulting from the TOA determination (as described by Taylor 1992) demonstrates the robustness of this method. The values show that even the most precise timing data sets are dominated by white noise. For more than half of our sample of 20, the estimated radiometer noise is of the order of a microsecond or more, demonstrating the need for longer integration times, larger bandwidth or larger collecting area.

4.6.2 Estimating Frequency-Dependent Effects

A second class of timing irregularities, which may be reduced by improved modelling of the ISM, are frequency-dependent effects. By measuring the offset between the timing residuals of the two 64 MHz-wide frequency bands of the CPSR2 backend system (see §2.3.5), we achieve a combined measure of such frequency-dependent effects and the earlier determined radiometer noise. For ease of reference, we will call the RMS of the timing offset between the two bands, divided by $\sqrt{2}$, the "sub-band RMS" henceforth; beyond radiometer noise, it includes the effects of frequency-dependent interstellar scattering, unmodelled dispersion measure variations (to some degree) and possibly some frequency-dependent calibration errors or profile variations. However, errors that affect both bands equally will be excluded from the sub-band RMS, while still contributing to the RMS of the normal timing residuals. The difference between the timing and sub-band RMS must therefore be composed of clock errors, most calibration imperfections, errors in the pulsar and planetary ephemerides, intrinsic timing noise and backend-induced instabilities.

The sub-band RMS for the three selected pulsars is presented in column three of Table 4.9. Columns five and six of the same Table provide the differences of the sub-band RMS with the timing RMS and the radiometer noise, respectively and were derived by assuming these effects all add in quadrature:

$$\sigma_\nu = \sqrt{\sigma_{\mathrm{sb}}^2 - \sigma_{\mathrm{Rad}}^2} \tag{4.5}$$

and

$$\sigma_\tau = \sqrt{\sigma_{\mathrm{Tot}}^2 - \sigma_{\mathrm{sb}}^2}. \tag{4.6}$$

4.6.3 Discussion

The quantities derived in the previous sections allow a simple bound to be placed on the potential timing precision that may be achieved with new backends and larger

telescopes. Specifically, assuming that newly researched techniques (Hemberger & Stinebring 2008; Walker et al. 2008) succeed in mitigating frequency-dependent ISM effects, the time-dependent instabilities in our timing will ultimately limit the timing precision. A simple estimate of this bound is provided by the difference between the RMS of the timing residuals and the sub-band RMS. This difference does not only include intrinsic pulsar timing noise, but also correctable corruptions such as errors in the clock corrections or planetary ephemerides, instabilities in the observing system or changes in hardware, incompleteness of the pulsar timing model and even dispersion measure changes (since only the differential part of the DM variations will be contained in the sub-band timing, while the largest contribution affects both bands equally). The combination of these effects implies the bound we derive on the time-dependent timing variations (titled "temporal systematic" in Table 4.9) is clearly a conservative limit on the achievable timing precision. Nevertheless, our analysis of PSRs J1909−3744 and J1713+0747 inspires confidence in the potential for pulsar timing at < 100 ns precision. We also note that, while both PSRs J1909−3744 and J1713+0747 are amongst the brightest MSPs in our sample, their timing is dominated by white noise; this suggests that the timing of most if not all of the weaker pulsars (which have inherently higher levels of radiometer noise) can be readily enhanced by the adoption of backends with larger bandwidth, longer integration times or future larger telescopes.

It is interesting to ponder whether future very large X-ray telescopes might be able to time MSPs accurately, thus removing the entire ISM contribution to arrival time uncertainties. At present X-ray observatories cannot compete with radio timing but future missions might for selected objects. For example, X-ray timing profiles lack the sharp features that make pulsars like PSR J1909−3744 such a great timer, but this might change with increased sensitivity. Ultimately, gravitational wave astronomy based on pulsar timing might not only use data from a host of international observatories, but also from different wavebands.

4.7 Prospects for Gravitational Wave Detection

Jenet et al. (2005) derived the expected sensitivity of a PTA to a GWB with given amplitude, A, both for homogeneous arrays (where all pulsars have comparable timing residuals) and inhomogeneous arrays. They also pointed out the importance of prewhitening the residuals to increase sensitivity at larger GWB amplitudes. We present a simpler derivation of the sensitivity in Appendix A, in a manner that provides some guidance on analysing the data. We assume that the prewhitening and correlation are handled together by computing cross-spectra and we estimate the amplitude of the GWB directly rather than using the normalised cross correlation function. We assume that the noise is white, but can be different for each pulsar. Our results are very close to those of Jenet et al. (2005). The analysis could be easily extended to include non-white noise. In this section, we apply this analysis to the

current data and use it to make predictions for ongoing and future PTA projects. The input parameters for the different PTA scenarios considered are listed in Table 4.10, while the sensitivity curves are drawn in Figures 4.4 and 4.5.

We considered five ongoing PTA scenarios: *Current* refers to the data presented in this paper, using the shortest overlapping time span of the sample: five years[4]. *Predicted PPTA* assumes the usage of 256 MHz of bandwidth at Parkes, which implies a four-fold bandwidth increase and therefore a two-fold timing precision increase. In order to scale the RMS from our current data, we assume an intrinsic noise floor of 80 ns (as expected from Table 4.9) and scale the remainder according to the radiometer equation. This implicitly assumes that improvements in technology (which reduce the radiometer noise) are equalled by progress in calibration and ISM-correction methodologies (which decrease the frequency-dependent noise). This scenario is also the only one to be considered for more than five years, mainly in order to show the large impact a doubling of campaign length can have, but also because several years of high precision timing data with the given bandwidth do already exist (Manchester 2008). The *NANOGrav* scenario assumes Arecibo gain for the ten least well-timed pulsars and GBT gain for the ten best-timed pulsars, in order to get a fairly equal RMS for all 20 MSPs. *EPTA* assumes monthly observations with five 100 m-class telescopes (Janssen et al. 2008). An alternative to this scenario is presented in *EPTA–LEAP*, which interferometrically combines the five telescopes to form a single, larger one. This decreases the number of observations, but increases the gain.

Table 4.10: Assumed parameters for future and ongoing PTA efforts.

Scenario name	N_{tel}	Relative bandwidth	Dish diam. (m)	Observing regularity	Project length (yrs)
Current	1	1(=64 MHz)	64	weekly	5
Predicted PPTA	1	4	64	weekly	10
NANOGrav	2	4	305; 100	monthly	5
EPTA	5	2	100	monthly	5
EPTA - LEAP	1[a]	2	224	monthly	5
Arecibo-like	1	8	305	two-weekly	5
100 m-size	1	8	100	two-weekly	5
ASKAP	40	4	12	weekly	5
MeerKAT[b]	80	8	12	weekly	5

[a] Under the LEAP initiative, five 100 m-class telescopes will be combined into an effective 224 m single telescope.

[b] MeerKAT architecture from Justin Jonas, private communication.

---

[4]This ignores the shorter sampling of PSR J1824−2452, which may not prove useful in a PTA project lasting longer than a few years. For the purpose of this simulation we assume the timing precision of PSR J1824−2452 to remain identical, while the time span is increased to five years.

It must be noted that several of the pulsars under consideration cannot be observed with most Northern telescopes, due to the declination limits of these telescopes. Furthermore, this analysis assumes the timing residuals to be statistically white and while more than ten of the 20 pulsars under consideration already have shown significant stability over ten years or more, for the remaining ten we cannot confidently assume their stability on such timescales yet. We therefore assume stable replacement pulsars to be discovered as needed, especially for the few pulsars that have insufficient stability over five years. As mentioned before, we also assume that progress will be made in the mitigation of frequency-dependent calibration and ISM effects. Finally, this analysis is based on the Parkes data presented in this paper and therefore assumes systematic effects to be at most at the level of the Parkes observing system used.

Bearing all of this in mind, cautious optimism seems justified for GWB detection through PTA experiments on timescales of five to ten years, provided current models of gravitational wave backgrounds are correct. As described in §1.3.3, it must be noted that there are a substantial number of badly determined inputs in these models, especially those concerned with a GWB from SMBH mergers. It is, for example, still unclear exactly what fraction of galaxy mass is a result of merger events as opposed to accretion. Since only the merging of galaxies results in binary black holes and hence contributes to the GWB, this mass fraction is crucial for any reliable prediction of GWB strength.

Given the scaling laws that can easily be derived from equation (12) of Jenet et al. (2005), the GWB amplitude at which a $3\,\sigma$ detection can be made, scales as follows:

$$A_{S=3} \propto \frac{\sigma}{T^{5/3}\sqrt{N_{\mathrm{pts}}}}, \qquad\qquad (4.7)$$

where T is the time span of the data set, N_{pts} is the number of TOAs for each data set and σ is the average RMS of a data set. Since our analysis assumes an intrinsic noise floor of 80 ns for each scenario, the potential for reduction of σ is limited, leaving only the regularity of observations and the length of the campaign to dominate the sensitivity curve. This explains the equivalence of the NANOGrav and LEAP scenarios. It also implies that the sensitivity curves for the larger telescopes (i.e. all scenarios except "Current" and "PPTA") are limited by our bound of 80 ns - if this assumption for MSP intrinsic instability is overly pessimistic, then the actual sensitivity is expected to be higher. In particular, the benefit of LEAP over the standard EPTA scenario is strongly dependent upon this bound. Finally, the strong dependence on T underscores the importance of stability analysis over much longer time spans and continued observing. While our σ_{z} graph for J1713+0747 provides the first evidence for high stability over timescales beyond 10 years, such stability must still be demonstrated for many more MSPs.

With the completion of the Square Kilometre Array (SKA) pathfinders expected in three years time, we consider the potential of both the Australian SKA Pathfinder (ASKAP) and the South African Karoo Array Telescope (MeerKAT) for PTA pro-
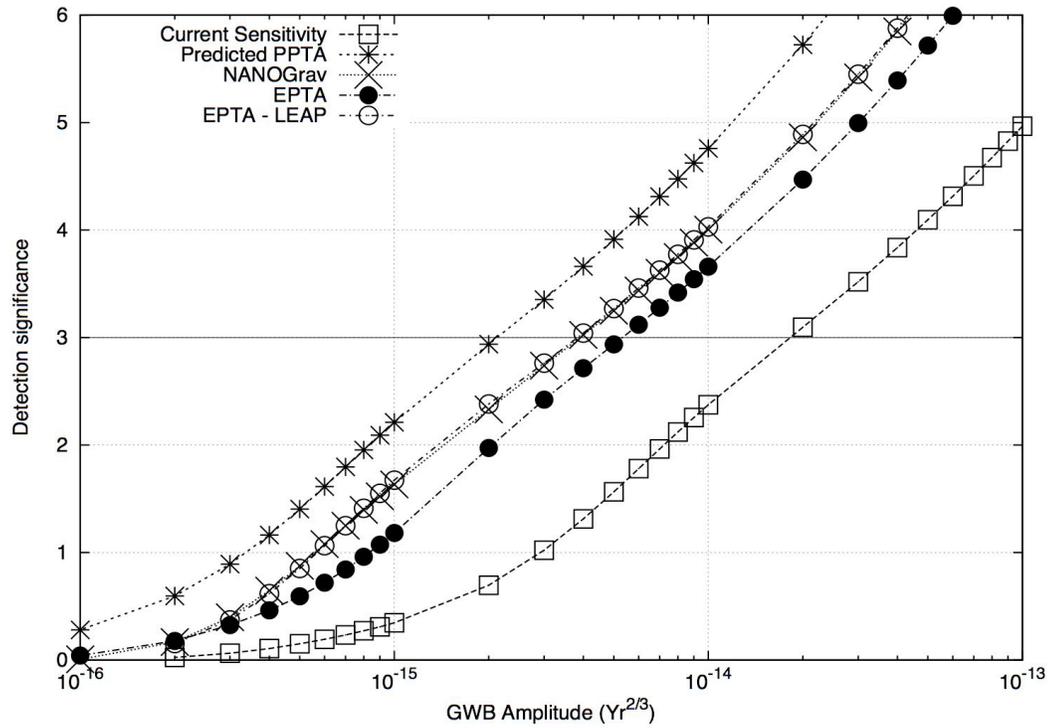
Figure 4.4: Sensitivity curves for different scenarios of PTA efforts. Notice the "NANOGrav" and "EPTA − LEAP" curves are almost coincident. Gravitational waves are predicted to exist in the range $10^{-15} - 10^{-14}$. See text and Table 4.10 for more information.
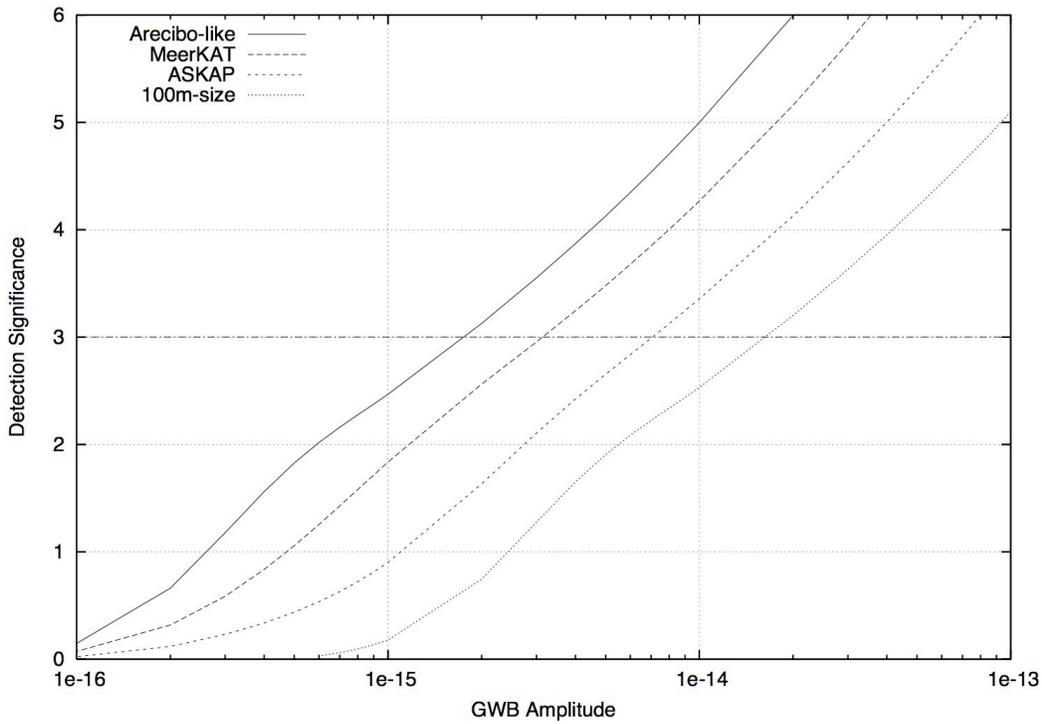
Figure 4.5: **Sensitivity curves for the two main SKA pathfinders and for telescopes with collecting area equal to those of the Arecibo and Green Bank radio telescopes. Gravitational waves are predicted to exist in the range $10^{-15} - 10^{-14}$. See discussion in §4.7 and Table 4.10 for more information.**

grammes. ASKAP is primarily designed for H I surveys and therefore sacrifices point source sensitivity for a wide field of view, whereas MeerKAT's design is better suited for point source sensitivity over a more limited field of view. The expected architecture for either telescope is listed in Table 4.10 - notice we assume phase-coherent combination of the signals of all dishes, effectively resulting in a scenario equivalent to a single telescope of diameter 107 m for MeerKAT and 76 m for ASKAP. The resulting sensitivity curves are drawn in Figure 4.5, along with a hypothetical curve for the most sensitive telescope currently operational, the Arecibo radio telescope. This Figure clearly shows the advantage MeerKAT holds over ASKAP for PTA work, both in number of dishes and in bandwidth. The sensitivity of Arecibo is much higher than that of either prototype, but its usefulness in reality is limited by the restricted sky coverage and hence available pulsars. While both MeerKAT and ASKAP can see large parts of the sky, the sky coverage of Arecibo as well as the short transit time make an exclusively Arecibo-based PTA practically impossible; however, its potential as part of a combined effort (Figure 4.4) or in a global PTA, is undeniable if the level of systematic errors is small compared to the radiometer noise.

4.8 Conclusions

We have presented the first long-term timing results for the 20 MSPs constituting the Parkes pulsar timing array. While two of these pulsars show clear signs of un-modelled low-frequency noise (PSRs J1824−2452 and J1939+2134), the remaining 18 pulsars show remarkable stability on timescales of five to ten years. A stability analysis has revealed that the overall level of systematic and pulsar-intrinsic effects is estimated to be below 100 ns for at least some of our pulsars. We interpreted this result in the context of ongoing and future pulsar timing array projects, demonstrating the realistic potential for GWB detection through pulsar timing within five to ten years, provided suitable replacements are found for the few unstable pulsars currently in the sample and provided technical developments evolve as expected. Given the location of currently known MSPs, the prospects of the MeerKAT SKA pathfinder as a gravitational wave detector are found to be particularly good.

Chapter 5

Spectral Analysis of Pulsar Timing Residuals and a Limit on the GWB

It is difficult to make predictions, especially about the future.
Niels Bohr and various others

5.1   Abstract

Pulsar timing data has been used to place limits on the amplitude of any potential GWB. The methods used for placing such limits have been either statistically unreliable or had limited applicability due to intricacies of real data sets (as discussed in §1.3.2). We present a new and universally applicable method that deals with many of these problems through the use of Monte-Carlo simulations. The method is based on the power spectrum of pulsar timing residuals, for the simulation of which we present a method similar to that proposed by Coles & Filice (1984). We use the proposed technique to bound the amplitude of the GWB based on the PSR J1713+0747 data set presented in Chapter 4. The derived limit is: $A < 1.0 \times 10^{-14}$ for a background with a spectral index of $\alpha = -2/3$.

5.2 Introduction

As described by Jenet et al. (2006) and in §1.3.2, the power a GWB introduces into pulsar timing residuals, is given by Equation 1.27:

$$P(f) = \frac{A^2}{12\pi^2} \frac{f^{2\alpha-3}}{f_0^{2\alpha}},$$

where A and α are the dimensionless amplitude and spectral index of the background and f is the frequency in the timing residuals. With spectral indices of $\alpha = -2/3$ or steeper (see §1.3.3), this results in a strongly low-frequency dominated spectrum in the timing residuals: $\alpha_{\mathrm{Res}} = 2\alpha - 3 = -13/3$ or steeper. In contrast, most MSP timing residuals have power spectra that approximate white noise (i.e. spectral index of zero), as demonstrated in Figure 4.2. Thus, when the GWB is present at the limit of detection, the GWB spectrum will rise above the white noise background only at the lowest frequencies in the power spectrum. The lowest frequencies of these power spectra can therefore be used as a constraint on the amplitude of any GWB present in this data, irrespective of the overall characteristics of the spectrum.

In order to achieve a proper estimate of the power present at these lowest frequencies, one requires a spectral power estimator that is capable of analysing unevenly sampled data with the potential presence of large gaps and significant deviations in measurement errors between data points. The spectral estimator must preserve the full spectral resolution of the data set, i.e. it must be sensitive to power at $f = 1/T$, where T is the length of the data set. The spectral estimator should furthermore be capable of analysing both the steep red noise of a GWB and the near-white noise of actual timing residuals. Some such techniques have been proposed in literature. These include the discrete Fourier transform (DFT; Scargle 1989), which has two major drawbacks. Firstly, spectral leaking restricts this method to spectral indices $\alpha_{\mathrm{Res}} \geq -2$; secondly, clustering of data can significantly affect the resulting spectrum (as e.g. shown in Figure 1d of Scargle 1989). The Lomb-Scargle periodogram (LSP) (Lomb 1976; Scargle 1982) is an alternative method based on least-squares fitting of sine waves to the data. Spectral leakage also restricts this method to spectral indices $\alpha_{\mathrm{Res}} \geq -2$. A different approach was described by Groth (1975) and Deeter (1984) and consists of fitting a series of orthonormal polynomials to data subsets with different lengths. The major advantage of this approach is its sensitivity to spectral indices down to $\alpha_{\mathrm{Res}} = -7$, but it sacrifices spectral resolution and the frequency scaling is not clearly defined. The σ_{z} stability parameter used in Chapter 4 and defined based on the Allen variance by Matsakis, Taylor & Eubanks (1997), is similar to the previous one, as it is also fundamentally defined in terms of third order polynomials (or particularly, $\ddot{\nu}$, which has a cubic signature in timing residuals). This method also lacks spectral resolution, however. Bayesian methods of determining spectral properties (such as spectral index and amplitude of spectral components) more directly, are also being developed (van Haasteren et al. 2008).

In this chapter, we present a new method for limiting the power in the GWB.

The method is described in §5.3 and is based on spectral analysis of pulsar timing residuals. To this end, we present a spectral analysis method for reliable estimation of low-frequency power in pulsar timing residuals in §5.3.1. The spectral estimates thus obtained are subsequently added in a weighted sum. The optimal weighting function is derived in §5.3.2. In §5.4, this method is applied to the PSR J1713+0747 data set presented in Chapter 4. In §5.5 we list a few lines of ongoing research which may improve the sensitivity of the proposed method. Our findings are summarised in §5.6.

5.3 Overview of the Method

Because the timing residuals are the sum total of all physical effects that are not included in the pulsar timing model, the power in these residuals can provide a limit on the strength of any GWB. Considering the strong prevalence of low frequencies in the effect of a GWB on timing residuals (as in Equation 1.27), the lowest frequency bins of a power spectrum from timing residuals contain most information and could be used to derive a stringent bound. The actual power spectrum of pulsar timing residuals is, however, biased by uneven sampling, fitting of model parameters and variable error bars on residuals. This causes a discrepancy between the measured power spectrum in timing residuals and the analytic prediction for the GWB effect as given by Equation 1.27, since it is very difficult to model these real-world biasing effects analytically. The method presented here is therefore based on a comparison of the spectrum of the actual timing residuals with the spectra of many simulated timing residuals. The simulated timing residuals, consisting of GWB plus white noise, are analysed in exactly the same way as the actual timing residuals.

First, a weighted sum of the lowest frequency powers of the timing data set is determined as the statistic S_{data} from which the limit will be derived. Secondly, a series of stochastic GWBs at a trial amplitude, A_{GWB}, are added to statistically white (radiometer) noise and sampled at the SATs of the real data set. After performing the same parameter fitting as for the real data, the same statistic is calculated from the simulated, GWB-affected data sets, resulting in a distribution of statistics $S_{\text{GWB},i}$. The amplitude $A_{\text{GWB},95\%}$ for which 95% of the simulated statistics $S_{\text{GWB},i}$ are higher than S_{data}, will be a $2\,\sigma$ limit on the GWB amplitude.

The different steps of the method will be described below. §5.3.1 outlines the spectral analysis method, §5.3.2 derives the optimal spectral weighting formula for determination of the statistic. The Monte-Carlo simulations are based on the code described in detail in Hobbs et al. (2009).

5.3.1   Spectral Analysis of Pulsar Timing Residuals

Most commonly, power spectra are obtained based on the discrete Fourier transform (DFT) of the data (adapted from Bracewell 2000)[1]:

$$X(\nu_m) = \frac{1}{N} \sum_{n=0}^{N-1} x(t_n) e^{-2\pi i t_n \nu_m} \tag{5.1}$$

for a time series $x(t)$ with N data points. Time and frequency are discretised as follows:

$$
\begin{aligned}
t_n &= n\, dt \\
\nu_m &= \frac{m}{N\, dt},
\end{aligned}
\tag{5.2}
$$

with m and n integers running from 0 to $N - 1$. The power spectral density $P(\nu)$ is then obtained as the squared amplitude of $X(\nu)$. In order to allow comparison with a theoretical spectral density, this function needs to be normalised. Furthermore, we are interested only in the power at positive frequencies, because the power spectrum is even ($X(\nu) = X(-\nu)$). This follows from the hermitian property of Fourier transforms and the fact that the sampled time-series $x(t_n)$ is real valued. Normalising the power spectral density in case of a one sided power spectrum, is achieved through:

$$P(\nu_m) = T\, |X(\nu_m)|^2 \tag{5.3}$$

with T the length of the time series, $x(t)$.

The requirement for equal spacing between samples is not fulfilled in pulsar timing data. A possible solution for this is provided by the Lomb-Scargle periodogram (Lomb 1976; Scargle 1982), which estimates the power spectrum of a time series based on least-squares fitting of sines and cosines. An alternative method that holds our preference for reasons to be outlined shortly, is to interpolate the data onto an equally spaced grid (as for example described in Press et al. 1992).

Aliasing and Smoothing

According to the Nyquist sampling theorem, the sampling frequency f_{samp} of a signal must be twice as high as the highest frequency present in that signal. Pulsar timing data is typically only sampled at weekly to monthly intervals, but has power at much higher frequencies. In such an event, power at frequencies higher than $f_{\mathrm{samp}}/2$ will be aliased to lower frequencies according to the formula $f_{\mathrm{measured}} = |f_{\mathrm{data}} - f_{\mathrm{samp}}|$. By means of example, power at a frequency $f_{\mathrm{in}} = f_{\mathrm{samp}}/2 + \delta f$, will be aliased down to $f_{\mathrm{measured}} = f_{\mathrm{samp}}/2 - \delta f$, as shown in the top image of Figure 5.1 and more fully

---

[1]Notice that the normalisation by $1/N$ in Equation 5.1 may be omitted depending on the definition used.
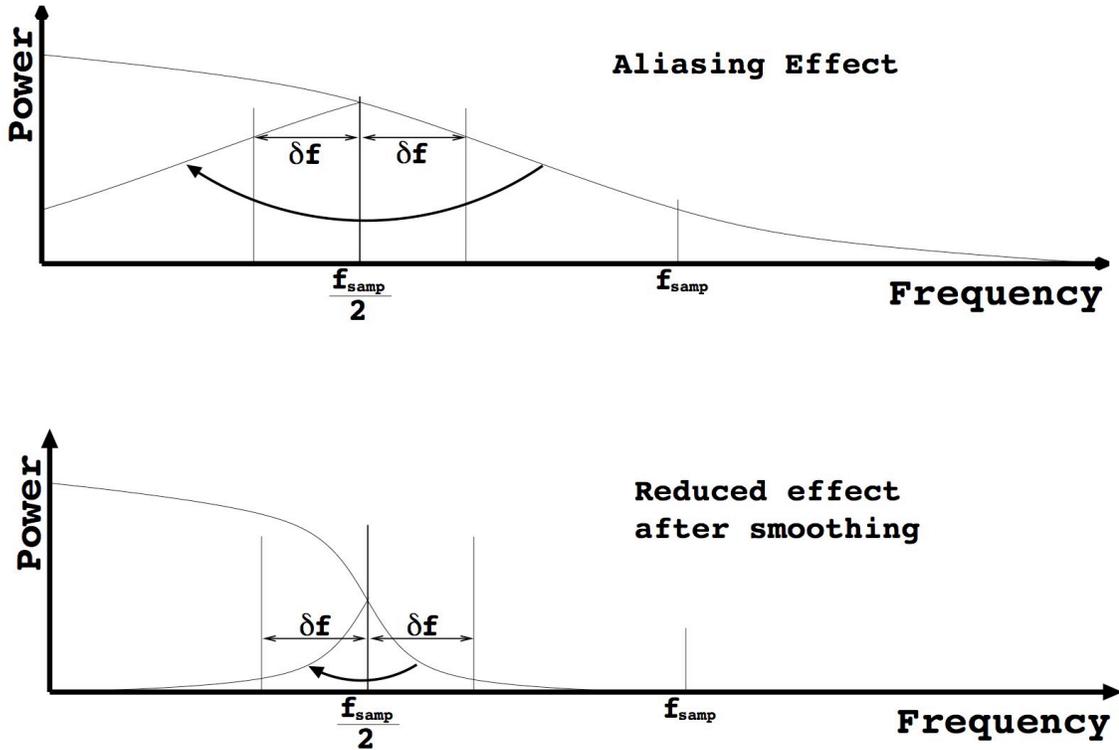
Figure 5.1: Aliasing in power spectral analysis. If a process contains power at frequencies higher than half the sampling frequency f_{samp}, then that power will be mirrored into lower frequencies of the spectrum. This mirroring is displayed in the top image. This effect can be far reduced by smoothing the time signal at timescales up to $t_{\text{smooth}} = 2/f_{\text{samp}}$, as shown in the bottom image. The effect of this smoothing will depend on the spectral characteristics of the smoothing filter and the spectral leakage properties of the spectral analysis method.

discussed in Bracewell (2000). This aliasing effect is only significant at the high-frequency end of the spectrum since fitting for pulse phase, pulse frequency and pulse frequency derivative strongly reduce the power at the lowest frequencies; moreover, the power spectrum is an even function as the time series is real valued. To limit the aliasing effect at higher frequencies, we apply a boxcar smoothing algorithm as described in Press et al. (1992). The combined effect of this smoothing on the earlier mentioned interpolation, can bee seen in Figure 5.2 for the actual pulsar data and in Figure 5.3 for a simulated data set with a GWB included.

Prewhitening and post-reddening

Another difficulty in spectral analysis of pulsar timing residuals is the potential spectral steepness of the data. While MSPs are mostly spectrally white (i.e. equal power at all frequencies - as shown in Chapter 4), the spectra of young pulsars can be much steeper (see, e.g. Kopeikin 1999) and residuals with a simulated GWB are
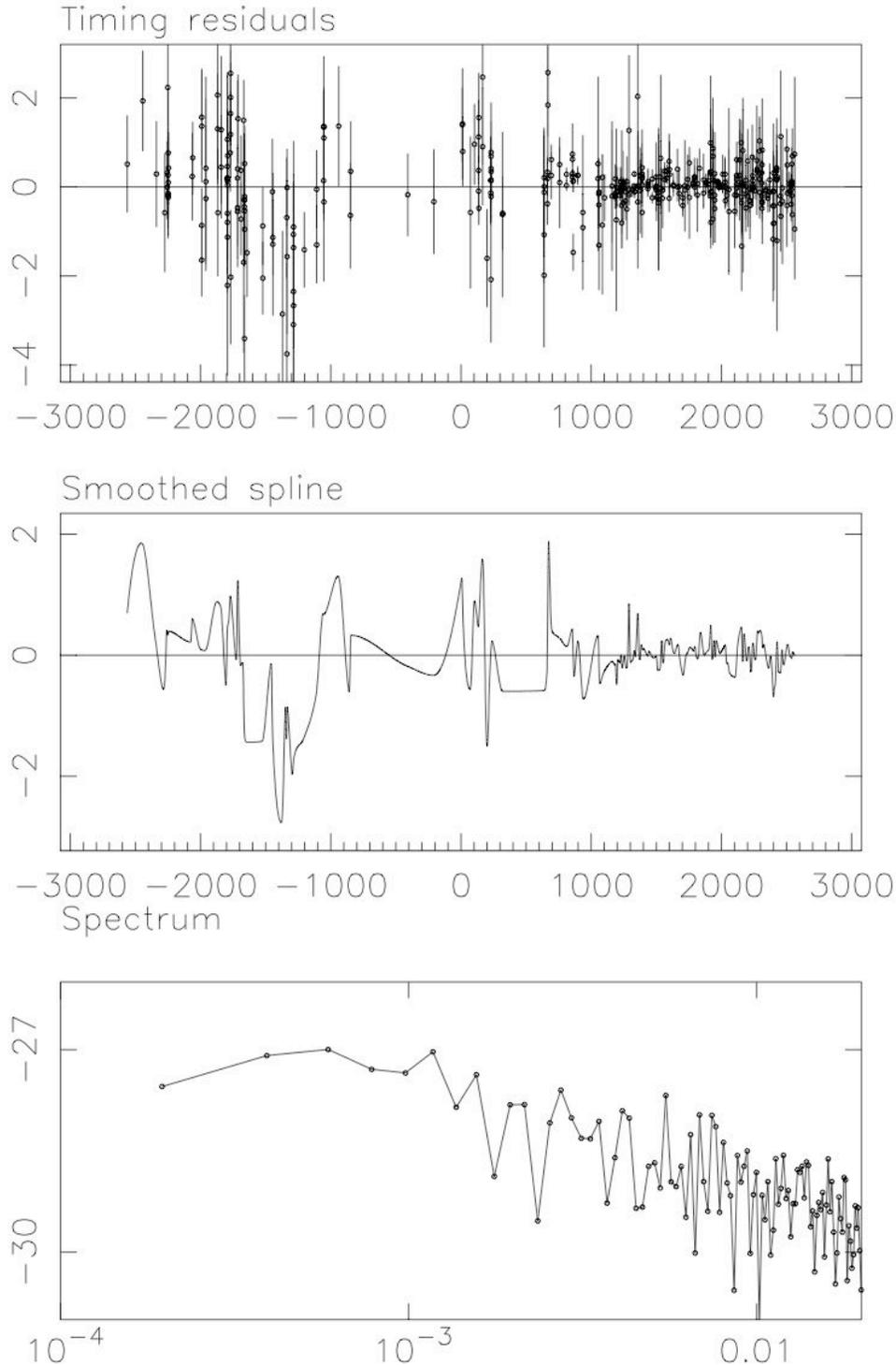
Figure 5.2: Spectral analysis of timing residuals from PSR J1713+0747. Top: PSR J1713+0747 timing residuals. Middle: smoothed spline interpolation of the timing residuals shown above. Bottom: lowest frequencies of the power spectrum of PSR J1713+0747. Units of the X-axes are days from the centre for the top two figures, days^{-1} for the bottom figure. Units of the Y-axes are μs for the top two figures and yr^3 for the bottom figure. Since this spectral analysis is unweighted, the power spectral estimates shown in the bottom plot are χ^2 distributed with two degrees of freedom. This means that the uncertainties can be obtained by scaling of the displayed curve, as can e.g. be seen in Figure 5.4.
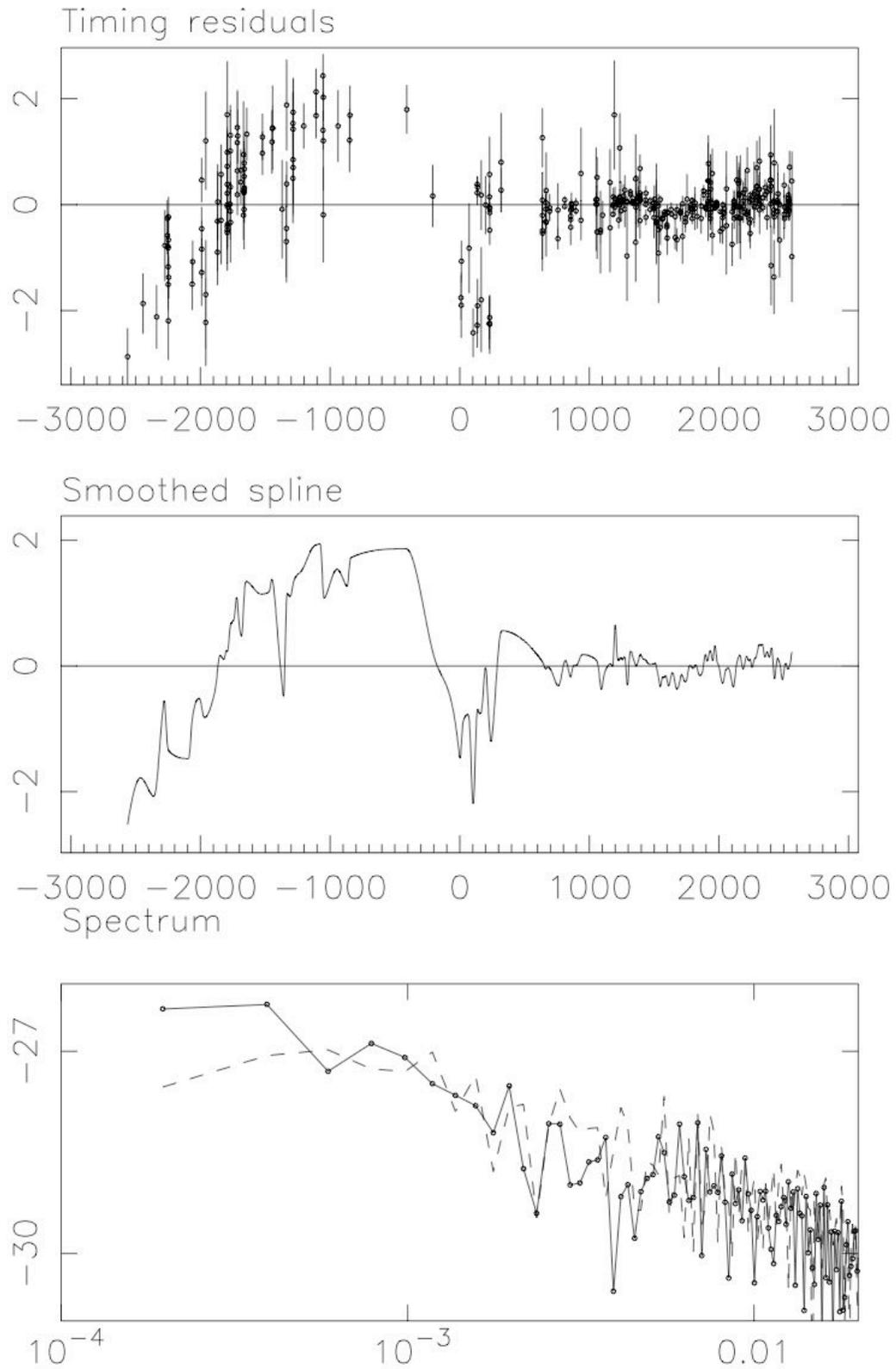
Figure 5.3: Spectral analysis of the actual timing residuals from PSR J1713+0747 with a simulated GWB of $\alpha = -2/3$ and $A = 1.1 \times 10^{-14}$ added. Plots and units identical to those of Figure 5.2. The dashed line in the bottom plot is the spectrum of the pulsar data shown in Figure 5.2.

also expected to be steep, as shown in Equation 1.27. Such steep spectra will cause problems with spectral leakage (Bracewell 2000). This arises as a consequence of the discrete sampling of the time series. Effectively, sampling equals a multiplication of the continuous time series with a set of delta functions. As multiplication in the time domain is equivalent to convolution in the Fourier domain, the effect of sampling on the Fourier transform of the data (and by extension on the power spectrum) is a convolution with a sinc-like function, the shape of which depends on the actual characteristics of the sampling function. This convolution causes power to be redistributed across the spectrum, which has no significant effect in the case of a white noise spectrum. In any other case however, power will seep from frequencies with high power to frequencies with lower powers. In the case of a DFT or LSP, this causes spectral features to be flattened to have a maximal spectral slope of two. A possible remedy is to taper the sampling function, but this reduces the effective length of the data set and therefore the sensitivity to GWs.

An alternative solution is provided by the combined application of (first or second order) prewhitening before spectral analysis and post-reddening of the obtained spectrum. In first order prewhitening, data points are replaced by their difference with the next point. Effectively the resulting data set is the first time derivative of the time series and will therefore be less steep. After the power spectrum of this new data set is calculated, it will be artificially steepened to undo the effect of the prewhitening. In this way, the DFT and Lomb-Scargle analyses are applicable to spectra with $-2 > \alpha_{\mathrm{Res}} > -4$ when using first order prewhitening. Second order prewhitening applies the same differencing method twice, extending the applicability of the spectral analysis to include $-4 > \alpha_{\mathrm{Res}} > -6$, covering all spectral indices expected in the analysis of GWBs and MSPs. While this method works well for spectrally uniform data sets, a combination of (white) receiver noise and a (red) GWB would require different levels of prewhitening at different frequencies. This could be accommodated through correct application of low- and high-pass filters and subsequent combination of the resulting spectra. In the present case, however, the receiver noise in the pulsar timing data is at or above the level of the GWB power, even in the lowest frequency bins. If a realistic level of white noise is added to the simulated GWB and sampling and fitting effects are taken into consideration, the effect of the GWB on the simulated data set is insufficient to warrant any prewhitening in most (if not all) cases.

Power Spectrum

After spline fitting, smoothing, resampling on a regular grid and potential prewhitening, the power spectrum can be analysed with any type of analysis technique. In order to avoid unneeded complexities, we apply a DFT and subsequently add the real and imaginary parts in quadrature to determine power. Because the data are now evenly spaced, the LS approach provides identical results. An example of the PSR J1713+0747 timing residual spectrum is given in the bottom plot of Figure 5.2.

If a GWB with spectral index $\alpha = -2$ and amplitude $A = 10^{-14}$ is added to these residuals before refitting the timing model and performing the spectral analysis, the power spectrum in Figure 5.3 is obtained. The comparison of these two spectra shows that the background effect is very limited and - if anything - restricted to the lowest frequency bin.

5.3.2 Optimal Weighting Function for the Power Spectral Statistic

After the power spectrum of the timing residuals is determined, the power spectral estimates of the lowest few frequency bins are combined into a statistic that is optimally sensitive to the simulated GWB effect. Theoretically this statistic could simply be the power in the lowest frequency bin because the GWB would have its strongest influence there. Optimally weighted addition of the power in several frequency bins, however, will reduce the variance on our statistic and therefore provide a more optimal limit. The optimal weighting can be thought of as a series of two consecutive actions, namely:

Prewhitening: If the power spectrum of the pulsar timing residuals is not spectrally white but has excess low-frequency power, then the detection statistic S will be dominated by the power in the lowest frequency bin alone. This will limit the usability of any pulsar timing data set with some form of red noise - whether this noise is due to intrinsic timing irregularities, the ISM, the instrumentation or anything else. To normalise the relative influence of frequency bins of the pulsar timing data, we prewhiten the data by dividing the power spectrum by a model of the residual power spectrum of the pulsar data, $\tilde{P}_{\text{model}}(\nu)$ (Note: $\tilde{P}(\nu)$ is the power spectrum after sampling and fitting, where $P(\nu)$ is the theoretical input power spectrum. If H is the TEMPO2 transfer function, then $\tilde{P}(\nu) = HP(\nu)$.)

Filtering: The prewhitened power spectral estimates are multiplied by a frequency-dependent filtering function $F(\nu)$ before being added into the detection statistic S. This implies S is defined as:

$$S = \sum_{i=0}^{N} \left(\frac{\tilde{P}(\nu_i)}{\tilde{P}_{\text{model}}(\nu_i)} F(\nu_i) \right) \quad (5.4)$$

where N is the number of frequency bins to be added.

The derivation of the optimal filter $F(\nu)$ follows below. Since this filter optimises the sensitivity to a GWB, it is identical for the current purpose of limiting the GWB strength and for actual detection of the GWB. It therefore also provides the optimal weighting function used in Equation A.5 in Appendix A.

The goal of filtering is to optimise the contribution of the GWB component in the observed pulsar timing residuals. The filtering function $F(\nu)$ will therefore

be defined so that $\tilde{P}_{\mathrm{obs}}(\nu)F(\nu)$ will approach $\tilde{P}_{\mathrm{GWB}}(\nu)$. Based on a standard χ^2 minimisation, this means that

$$\sum_{i=0}^{\infty} \left[\tilde{P}_{\mathrm{obs}}(\nu_i)F(\nu_i) - \tilde{P}_{\mathrm{GWB}}(\nu_i) \right]^2 \tag{5.5}$$

has to be minimised. Applying prewhitening as described above, this minimisation becomes:

$$\sum_{i=0}^{\infty} \left[\frac{\tilde{P}_{\mathrm{obs}}(\nu_i)}{\tilde{P}_{\mathrm{model}}(\nu_i)} F(\nu_i) - \frac{\tilde{P}_{\mathrm{GWB}}(\nu_i)}{\tilde{P}_{\mathrm{model}}(\nu_i)} \right]^2. \tag{5.6}$$

Derivation of this equation with respect to F at each frequency gives:

$$2 \left(\frac{\tilde{P}_{\mathrm{obs}}(\nu_i)}{\tilde{P}_{\mathrm{model}}(\nu_i)} F(\nu_i) - \frac{\tilde{P}_{\mathrm{GWB}}(\nu_i)}{\tilde{P}_{\mathrm{model}}(\nu_i)} \right) \frac{\tilde{P}_{\mathrm{obs}}(\nu_i)}{\tilde{P}_{\mathrm{model}}(\nu_i)} = 0, \tag{5.7}$$

which results in:

$$F(\nu) = \frac{\tilde{P}_{\mathrm{GWB}}(\nu)}{\tilde{P}_{\mathrm{obs}}(\nu)}. \tag{5.8}$$

Effectively, this is a Wiener filter as derived in Press et al. (1992).

Combining both the prewhitening and the filtering factors, gives the effective weighting function:

$$W(\nu) = \frac{\tilde{P}_{\mathrm{GWB}}(\nu)}{\tilde{P}_{\mathrm{obs}}(\nu)\tilde{P}_{\mathrm{model}}(\nu)}, \tag{5.9}$$

which will be applied to the power spectrum of the pulsar timing residuals as well as to the power spectra of the post-fit residuals from the simulated GWBs.

Practically, $\tilde{P}_{\mathrm{GWB}}(\nu)$ is the mean post-fit residual power spectrum of the Monte-Carlo simulations of the GWB. $\tilde{P}_{\mathrm{obs}}(\nu)$ cannot directly be obtained, since only a single instance of the timing residual spectrum can be obtained. We therefore assume the underlying post-fit power spectrum of the data to be smooth and sufficiently approximated by an analytic model, i.e. $\tilde{P}_{\mathrm{obs}}(\nu) \approx \tilde{P}_{\mathrm{model}}(\nu)$. This results in:

$$W(\nu) = \frac{\tilde{P}_{\mathrm{GWB}}(\nu)}{\tilde{P}_{\mathrm{model}}^2(\nu)}, \tag{5.10}$$

which is of the same form as the optimal weighting function used for detection of a GWB, used in Equation A.5. The detection statistic now becomes simply:

$$S = \sum_{i=0}^{N} \left(\tilde{P}(\nu_i)W(\nu_i) \right). \tag{5.11}$$

This weighting works identically to the whitening method proposed by Jenet et al. (2005) and can easily be understood intuitively. Consider a residual spectrum

with power $\tilde{P}(\nu) = \tilde{P}_{\mathrm{GWB}}(\nu) + \tilde{P}_{\mathrm{WN}}(\nu)$, where $\tilde{P}_{\mathrm{GWB}}$ is the GWB contribution to the pulsar spectrum and $\tilde{P}_{\mathrm{WN}}$ is the Gaussian (white) noise in the data. Now define the corner frequency ν_{c} at which $\tilde{P}_{\mathrm{GWB}}(\nu_{\mathrm{c}}) = \tilde{P}_{\mathrm{WN}}(\nu_{\mathrm{c}})$. Then, due to the steepness of the GWB, $\tilde{P}_{\mathrm{GWB}}(\nu) \gg \tilde{P}_{\mathrm{WN}}(\nu)$ for all $\nu < \nu_{\mathrm{c}}$ and therefore:

$$\tilde{P}(\nu) \approx \tilde{P}_{\mathrm{GWB}}(\nu) \quad \text{if } \nu \ll \nu_{\mathrm{c}} \tag{5.12}$$
$$\tilde{P}(\nu) \approx \tilde{P}_{\mathrm{WN}}(\nu) \quad \text{if } \nu \gg \nu_{\mathrm{c}} \tag{5.13}$$

This implies that the detection statistic can be split into two sums:

$$S = \sum_0^{\nu_{\mathrm{c}}} \tilde{P}_{\mathrm{GWB}}(\nu)W(\nu) + \sum_{\nu_{\mathrm{c}}}^{\infty} \tilde{P}_{\mathrm{N}}(\nu)W(\nu). \tag{5.14}$$

Which further simplifies to:

$$S = \sum_0^{\nu_{\mathrm{c}}} \frac{\tilde{P}_{\mathrm{GWB}}^2}{\tilde{P}_{\mathrm{GWB}}^2} + \sum_{\nu_{\mathrm{c}}}^{\infty} \frac{\tilde{P}_{\mathrm{GWB}}}{\tilde{P}_{\mathrm{WN}}}. \tag{5.15}$$

Effectively, this means that any frequency channel where the GWB power is dominant adds as unity, while any other channel only adds according to its SNR. Without weighting or whitening, however, each channel simply adds its power, which always results in a strong domination of the lowest frequency bin and consequentially a saturation of the detection significance for increasing GWB amplitudes.

5.3.3 Measurement Uncertainty of the Detection Statistic

As described at the start of §5.3, the detection statistic derived from the data (S_{data}) will be compared to the Monte-Carlo-derived distribution of statistics ($S_{\mathrm{sim,GWB}}$). In performing this comparison, no direct measurement uncertainty of S_{data} is determined. The justification for this is that the measurement S_{data} is treated as a single realisation of a distribution. Given this realisation, we can assess the likelihood of a given distribution of detection statistics resulting from the Monte-Carlo simulations. Because our analysis treats the timing residuals in an unweighted way, each detection statistic calculated from the simulations will have identical error bars to those applicable to the measurement of the actual data and therefore the shape of the distribution from which S_{data} is derived, will be identical to the shape of the distribution derived from $S_{\mathrm{sim,GWB}}$, irrespective of the sources of timing residuals used in the simulations.

A related point concerns the inclusion of TOA uncertainties in the Monte-Carlo simulations. Since the limit method proposed in this chapter effectively compares power levels and since any additional source of timing residuals only increases these power levels, the most conservative limit on the GWB will be obtained from simulations that contain nothing but a GWB as source of timing residuals. As will be outlined shortly, we will add white noise at a fraction of the TOA error bars to this

GWB. This addition will strengthen the limit since a lower level of GWB will be needed to achieve the same power levels - or, by extension, detection statistic. We will, however, be careful to only add white noise at a level that is well below the level that can reasonably be expected to be present in the data, in order to avoid putting an overly optimistic limit on the GWB. While this implies the level of white noise in the simulations is lower than that in the real data, this will not affect the shape of the distribution of detection statistics, but will only shift it to lower values - pushing the GWB amplitude limit higher.

5.4   A New Limit on the Amplitude of the GWB

In this section we apply the limiting method described in the preceding section to the most precise long-term timing data set presently available - the PSR J1713+0747 timing presented in Chapter 4. While the method consists of iterating over a series of GWB amplitudes to determine the amplitude that results in a 95% confidence limit, throughout this section we will illustrate the procedure using a GWB with amplitude $A = 1.1 \times 10^{-14}$ and spectral index $\alpha = -2/3$.

The spectrum of the PSR J1713+0747 data set after smoothing and interpolating can be seen in Figure 5.2. The relative steepness of this spectrum at higher frequencies is mainly due to a combination of the applied smoothing, TEMPO2 fitting and sampling effects. At the lower frequencies that are presently of interest, however, this spectrum is fairly well modelled with a uniform (i.e. white) spectrum, so that $\tilde{P}_{\mathrm{model}}$ in the weighting function becomes inconsequential.

After determining the spectral model of the pulsar data, we create fake data sets that contain a GWB with a given amplitude, to which we apply the same model fitting and spectral analysis methods as were applied to the pulsar data. However, because of the prior knowledge that radiometer noise exists in our data and because the least-squares fitting routines may not function properly in the presence of the steep red noise of the GWB, we add some amount of Gaussian scatter to the timing residuals of the simulated GWB. Because this addition will increase the spectral power levels and therefore lower the limit on the GWB amplitude, we have to make sure that the level of added white noise is realistic, if not conservative. To that purpose, we add white noise at half the level of the TOA error bar. This amount can be considered conservative when taking into account the analysis of §4.6, which separated the effects of radiometer noise from the total timing RMS. As an example, Figure 5.3 shows the post-fit residuals and spectrum of a GWB added to the actual PSR J1713+0747 data set. The white noise in the simulations used to derive the limit on the GWB amplitude, will be half of what is present in the residuals shown here.

The simulations of a large number of GWB-affected timing residual data sets is followed by the derivation of an average spectrum for the post-fit GWB spectrum, $\tilde{P}_{\mathrm{GWB}}$, along with its confidence interval. For our example GWB, such a spectrum

is shown in Figure 5.4, along with the spectrum from the original PSR J1713+0747 data set. Using this average spectrum, we can now determine the optimal weighting function defined in Equation 5.10 and calculate the detection statistic from Equation 5.11 for both the real data set and the simulated GWB-affected data sets. A histogram of these statistics can be drawn for each GWB amplitude (see, e.g. Figure 5.5). The detection percentage at a given GWB amplitude is the fraction of Monte-Carlo realisations that results in a statistic that is larger than the data statistic. The amplitude for which $S_{\mathrm{data}} < S_{\mathrm{sim,GWB}}$ for 95% of the time, will be our limit. In Figure 5.6, the detection percentage is plotted for a range of GWB amplitudes, demonstrating the smooth relation between detection percentage and GWB amplitude. This figure also shows the detection percentage reaches 95% at an amplitude of 1.0×10^{-14} - which is just lower than the limit of 1.1×10^{-14} placed by Jenet et al. (2006), but still outside the predicted range of $10^{-15} - 10^{-14}$.

5.5 Ongoing Research

The previous section demonstrated the basic functionality of the limit method presented. The method may, however, still be optimised in a few ways. These will be discussed briefly below.

Spectral analysis method: The analysis performed in the previous section used a DFT-based spectral analysis as described in §5.3.1. However, since the PSR J1713+0747 data set is very long and has reasonable sampling regularity, the effects of aliasing may be limited. This would imply smoothing is not required and that the LSP could be used without the need for interpolation of the data. This approach could affect the resulting limit, but the difference between the two approaches is difficult to analyse analytically. A quantification of the relative merits based on simulations may therefore be in order.

Pulsar model spectrum: Modelling the noisy power spectrum of a pulsar can be a relatively complicated exercise once the spectrum is not (close to) white as it is in the case of PSR J1713+0747. Formulations based on sums of exponential functions and white noise floors provide a reasonable analytic basis for such models (such functions have been used to model pulsar timing noise, see e.g. Cordes & Downs 1985; Kopeikin 1999), but these ignore the fact that model fitting for pulse phase, frequency and frequency derivative always depresses the power in the lowest frequency bin.

Accurate estimation of timing residual sources: As noted in §5.4, every additional source of noise that can be added to the Monte-Carlo simulations, will lower the derived limit on the GWB amplitude. As an illustration, the limit derived from adding white noise at 50% of the TOA error bars is 1.0×10^{-14}, which drops to 0.9×10^{-14} when 75% of the error bars is included and to
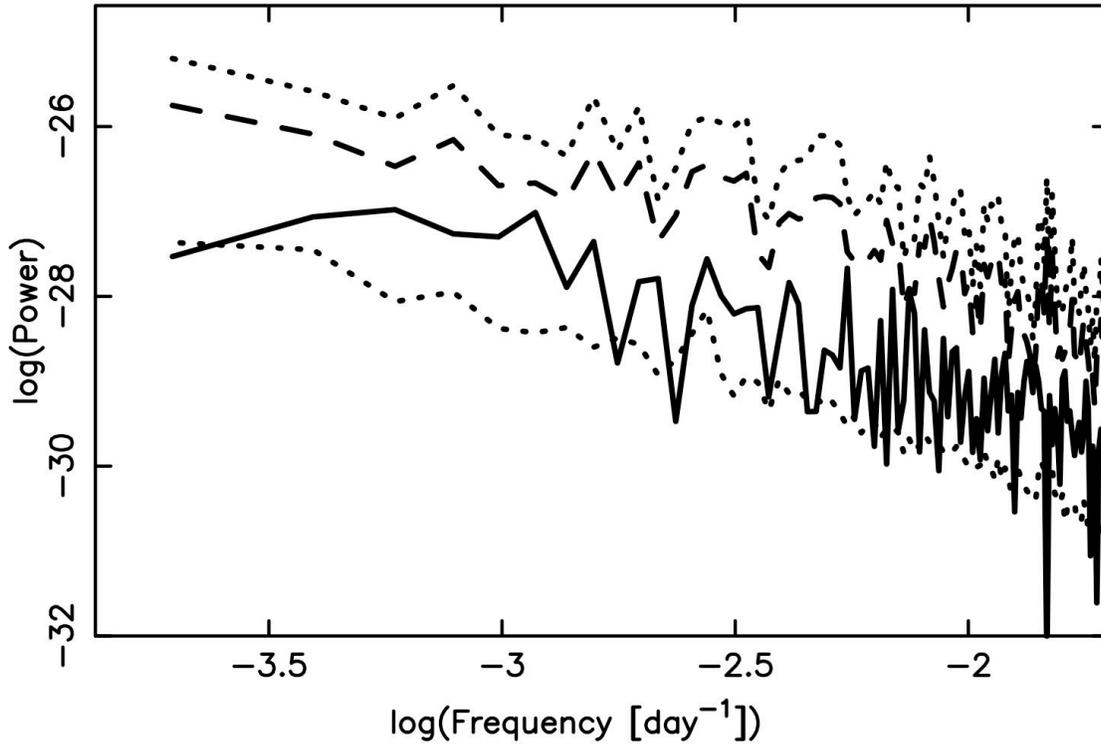
Figure 5.4: **Comparison of the power spectrum from the data with the average power spectrum of simulated data sets with a GWB introduced. The full line shows the spectrum of the PSR J1713+0747 data set previously shown in Figure 5.2. The dashed line shows the average post-fit spectrum of 5000 simulated pulsar timing data sets with sampling and model fitting identical to that of the PSR J1713+0747 data set and with the effects of a GWB with amplitude $A = 1.1 \times 10^{-14}$ and spectral index $\alpha = -2/3$ included. The dotted lines show the 90% confidence interval on this spectrum. This implies that in each frequency bin, 5% of realisations fall below the lowest dotted line, which can therefore be used as a lower bound at 95% certainty on the power spectral densities of the simulated data. These spectra are based on the DFT, after spline interpolation and smoothing on a timescale of 30 days. White noise at half the level of the TOA error bars was added to the simulated data sets, but this is not visible in this graph due to the combined effects of leakage, model fitting and smoothing.**
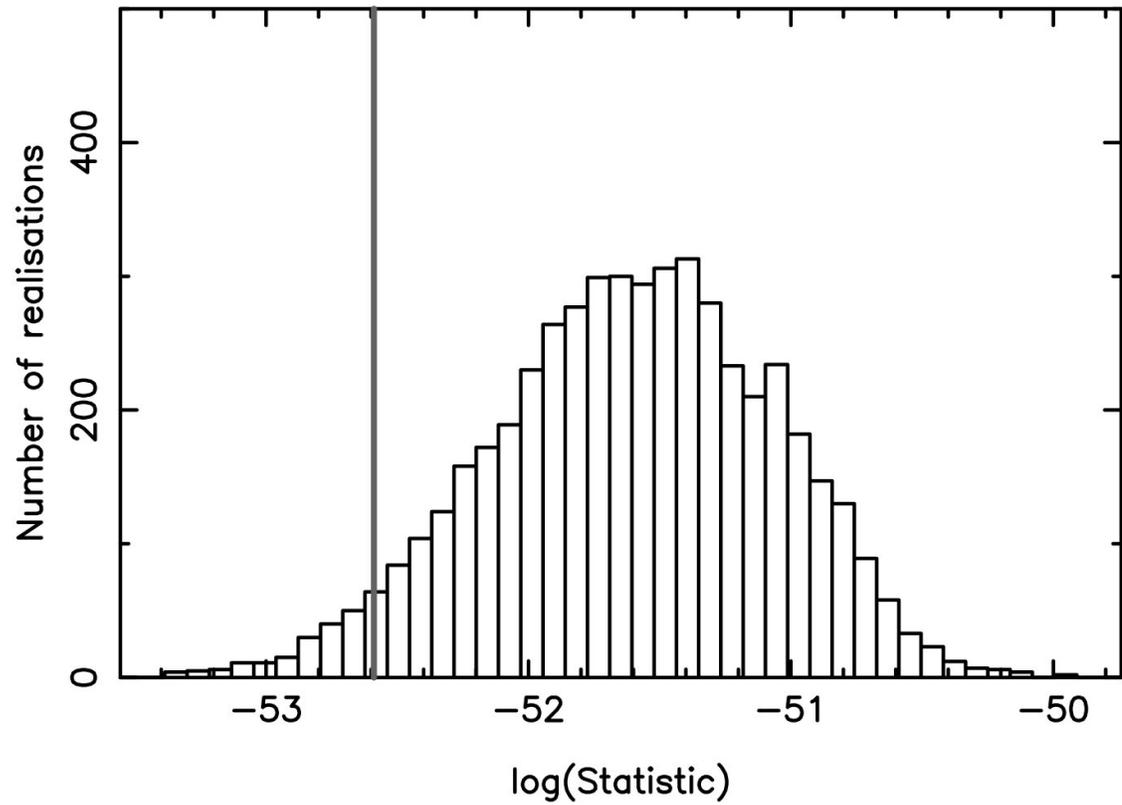
Figure 5.5: Histogram of the detection statistics from 5000 simulated pulsar timing data sets that contain the same GWB as described in the caption of Figure 5.4. The vertical line indicates the pulsar statistic. 96% of the statistics from simulated data sets are higher than this pulse statistic.
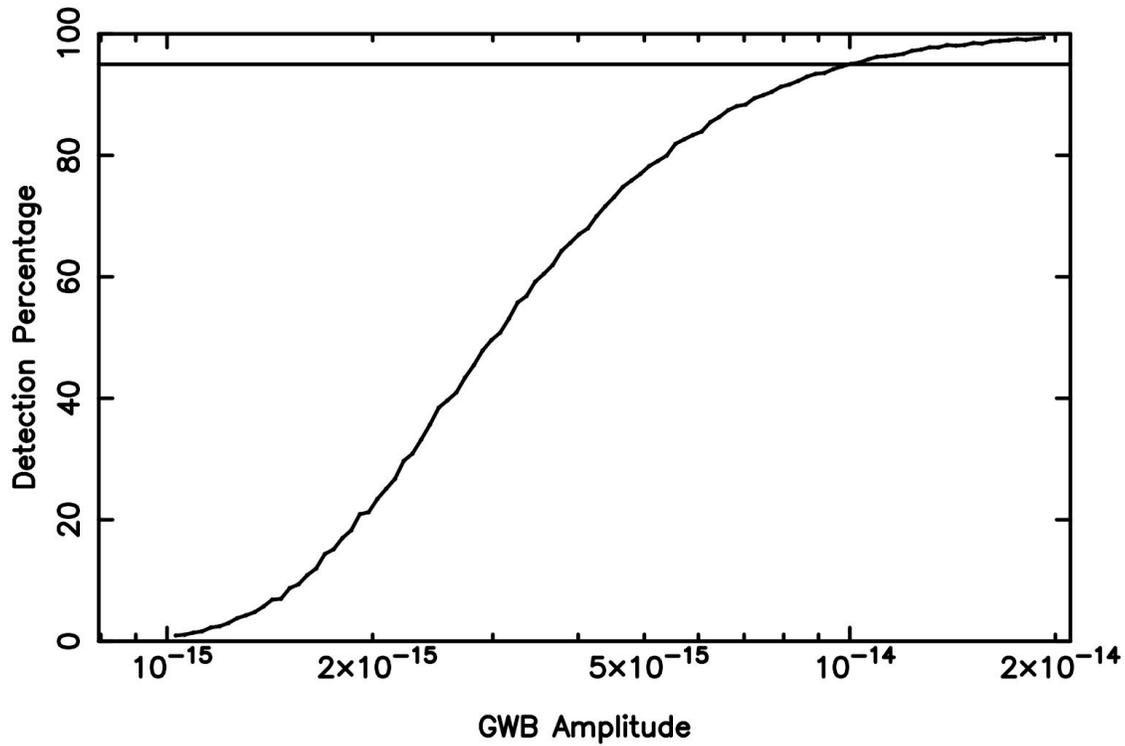
Figure 5.6: Detection statistic versus amplitude. As the GWB amplitude increases, the number of simulations that result in a detection increases. This increase is smooth, suggesting the uncertainty in the detection percentages is small. The curve crosses the 95% threshold at an amplitude around 1.0×10^{-14}.

0.8×10^{-14} when the TOA error bars are taken at face value. While the relative difference between these values may look insignificant at this stage, the increase of timing precision expected from the new generation of observational hardware may in a few years push these values down to levels close to the bottom of the predicted range, making every justifiable decrease important. Beyond addition of receiver noise, accurate spectral estimates of interstellar effects may also be determined and included in the simulations (when comparing to DM-uncorrected data such as e.g. the uncorrectable archival data), further lowering the limit.

**Weighted spectrum:** While the uncertainties on the pulsar timing residuals are not uniform, the spectrum analysis techniques we presented generally treat them as such. This does not invalidate the technique, since the treatment of the GWB-affected data is identical (and the white noise added to those TOAs is also not constant), but a weighted approach may provide a more sensitive limit. Again, an objective quantification of the difference in these approaches is not trivial.

Combination of pulsar statistics: The limit we derived is identical to that from Jenet et al. (2006), although those authors use a combination of seven pulsars, as opposed to only PSR J1713+0747. It is conceivable that an optimal way of combining the detection statistics of several pulsars will further improve our bound, but such a derivation is statistically complex because the pulsars are statistically heterogeneous.

5.6   Conclusions

Ultimately the most reliable upper bound on the GWB amplitude will be obtained through cross correlation of timing residuals from different pulsars, as implicitly intended in PTA projects. The sensitivity to the GWB, however, is a very strong function of the length of data sets. This makes long time series currently more sensitive than correlation analysis of more, but shorter data sets.

We have therefore presented a new and conceptually simple method to use pulsar timing data for placing a limit on the amplitude of the GWB. We have also applied this method to one of the longest and most precise data sets presented in Chapter 4, on PSR J1713+0747. As opposed to the method proposed by Jenet et al. (2006), our method does not make any assumptions about the timing data and can therefore be applied to any data set. As this method is based on the power spectrum of pulsar timing residuals, we have described a rigorous algorithm that allows the lowest frequencies of timing residuals to be analysed, notwithstanding potential issues caused by sampling effects and excess red noise. A Monte-Carlo simulation of the influence of a GWB on the pulsar timing residuals lies at the core of the technique, simplifying statistical arguments that caused problems for earlier methods. Our application of

this method to the PSR J1713+0747 data set resulted in a limit of $A = 1.0 \times 10^{-14}$ for a background with $\alpha = -2/3$, which is just below the strongest limit placed to date, by Jenet et al. (2006). A few ongoing lines of research that may improve the sensitivity of the technique, have been proposed.

Chapter 6

Discussion and Conclusion

... to boldly go where no man has gone before.
William Shatner (as Captain Kirk), Star Trek, 1966-1969

6.1 Introduction

This thesis considers the stability of MSPs over timescales of five to fifteen years, with the broader aim of feasibility studies for gravitational wave (GW) detection through pulsar timing arrays (PTAs). In this chapter, our most important conclusions are summarised (§6.2) in close combination with proposed extensions and improvements to this research (§6.3 and §6.4). We also list some of the more exciting prospects that can be expected in light of this research (§6.3). We end in §6.5 with the answer to the question we set out to ask: whether MSPs will enable direct detection of GWs.

6.2 Summary of Conclusions

Concerning the broader aim of GW detection, we have demonstrated the following:

Timing precision: At least some pulsars can be timed at precisions of $\sim 200\,\text{ns}$ over time spans of 5 to 14 years. Specifically, we achieved $166\,\text{ns}$ over $5.2\,\text{years}$ on PSR J1909$-$3744; $199\,\text{ns}$ over $9.9\,\text{years}$ on PSR J0437$-$4715 and $204\,\text{ns}$ over $14\,\text{years}$ on PSR J1713+0747. Following the analysis by Jenet et al. (2005) and the scaling laws derived from that analysis, this implies that GWB detection over a timescale of a decade or less is possible, provided this high level of timing precision can be achieved on a high enough number of pulsars.

Timing stability: A majority of the pulsars analysed (14 out of 20) show no convincing signs of instability in a σ_z analysis[1] on timescales of 12 years on average. This ensures sensitivity to a GWB will continue to increase as observing with new, high-bandwidth backends is continued up to a decade or longer. Such stability then enables PTA-style detection of GWs over long timescales, even if not enough bright pulsars can be found to achieve timing residuals well below $1\,\mu$s, as needed for detection efforts over shorter terms.

PTA prospects: The sensitivity of the radio telescope used drastically decreases the duration of the PTA project needed for a potential detection. This effect is, however, strongly dependent on the ultimate timing precision that might be achievable, but does underscore the importance of large telescopes for PTA efforts.

Ultimate timing precision: Over a period of five years, PSRs J1909−3744 and J1713+0747 place an upper bound of $\sim 80\,$ns on intrinsic limitations to timing precision. This demonstrates that improved algorithms for mitigation of interstellar effects as well as new observing hardware and calibration schemes, may well enable sub-100 ns timing over a time span of five years for the brightest pulsars in our sample.

Gravitational wave background (GWB) from supermassive black hole (SMBH) coalescence: In order to become sensitive to the entire predicted amplitude range from SMBH binary mergers, a PTA project will need to be maintained for well over five years, given current levels of timing precision and simple scaling laws (as shown in Figure 4.4). Five years of observations with the world's largest telescopes might, however, already provide sensitivity to a large fraction of the predicted range.

A few limits and measurements were made that in themselves or in combination with results from other authors, provide interesting input into some scientific discussions and investigations. These are summarised below:

- Limit on the variability of Newton's gravitational constant (Equation 3.4): $\dot{G}/G = (-5 \pm 18) \times 10^{12}\,\text{yr}^{-1}$. In combination with the VLBI parallax of PSR J0437−4715 measured by Deller et al. (2008), this limit was improved to $\dot{G}/G = (-5 \pm 26) \times 10^{-13}\,\text{yr}^{-1}$.

- Mass of PSR J0437−4715: $M_{\text{psr}} = 1.76 \pm 0.20\,M_{\odot}$.

- Limit on the GWB strength from PSR J1713+0747, for a background with $\alpha = -2/3$: $A < 1.0 \times 10^{-14}$. This is very close to the limit derived by Jenet et al. (2006).

---

[1]σ_z is a statistic related to the Allen variance. It analyses the stability of time series by determining the power present at different timescales.

- Anomalous Solar System acceleration: $|a_\odot/c| \leq 1.5 \times 10^{-18}\,\mathrm{s}^{-1}$ (95% certainty). This excludes the presence of any Jupiter-mass trans-Neptunian objects (TNOs) within $117\,\mathrm{AU}$ along the line of sight from the Earth to PSR J0437−4715.

- The formal measurement uncertainties reported by Tempo2 for the timing model parameters were underestimated by factors between 1.3 and 3.7 for binary parameters and factors around ten for non-binary parameters. While these are probably conservative estimates, they do demonstrate the large impact low-frequency noise can have on the reliability of timing results.

6.3 Lines of Further Research

In order to expand and improve the analysis presented in this thesis, several lines of future and ongoing research are proposed below.

Number of millisecond pulsars (MSPs) in a PTA: The standard scenario proposed by Jenet et al. (2005) required a minimum of 20 MSPs to construct a timing array and assumed the timing precision on all these pulsars to be equal. This thesis has provided some insight into the stability and relative timing precision achievable on the 20 MSPs of the Parkes PTA. Furthermore, prewhitening and optimised weighting methods effectively remove the strict requirement of 20 MSPs. In order to properly distinguish correlations due to clock errors, solar system ephemeris errors and GWB effects, some minimal number of pulsars and related distribution across the sky, will still be needed, however. An analysis into optimal inhomogeneous PTA scenarios could provide more clarity in this matter and as such aid in more optimally allocating the limited resource of observing time to a dedicated set of pulsars.

Surveys: The Southern sky has been thoroughly surveyed for all kinds of pulsars throughout the late nineties and early two-thousands. Nevertheless, PSR J1909−3744 - currently the most precisely timed pulsar in the PPTA sample - was only discovered in 2003. Given the computational complexity involved in discovering binary pulsars with high spin frequencies and the continuous increases in computational power, it can therefore be expected that even more bright and stable MSPs that may be of great use to PTA efforts, could be found in new and ongoing surveys. This is particularly true in the Northern hemisphere, where past surveys have either been insensitive to MSPs, or were badly affected by RFI. The greater sensitivity of the new generation of broadband pulsar backends as well as new, large telescopes such as the $500\,\mathrm{m}$ aperture spherical telescope (FAST) and (eventually) the SKA, will increase the sensitivity of these surveys, making exotic detections of distant but interesting pulsars more likely than ever before. Such pulsars will undoubtedly be weaker than many that already exist, unless they have large dispersions that

have hidden them from earlier generation surveys. If they are to feature in future timing arrays then it may be necessary to either use very large telescopes or use some form of methodology that eliminates or attentuates the impact of variable scattering on pulsar timing, such as those being pursued by Hemberger & Stinebring (2008) and Walker et al. (2008).

International pulsar timing array (IPTA): The data presented in this thesis were based on Parkes observations with typically hourly integrations. The timing precision of future data sets will be improved because of the increased bandwidth of the new generation of observing backends. Beyond that, timing precision could further be improved by using longer integration times, or by using larger telescopes. With current observing intensities of around 40 hours per fortnight for the PPTA (20 hours of multi-frequency observations for DM determination and an additional 20 hours for the actual timing observations), a further increase in observing time is unlikely to be granted given oversubscription rates of radio telescopes. As PTA-type projects are being undertaken at many different observatories across the world, however, a global joining of force would have access to a multiple of both the observing time and telescope sensitivity currently available to any one of the projects individually. This would imply that international collaboration may well be the fastest and surest means of securing a direct detection of the GWB.

Ultimate timing precision: With the anticipated commissioning of several large telescopes in 2012 and 2013 (FAST in the Northern hemisphere and MeerKAT and ASKAP in the Southern hemisphere) and with the proposed interferometric combination of the five major European telescopes under the LEAP project, telescope sensitivity in pulsar timing may be expected to reach unprecedented levels. This should drastically increase our knowledge of the intrinsic stability levels of MSPs and the highest possible timing precision that could be achieved. This, in turn, will provide more accurate predictions of realistic PTA sensitivity levels and provide strong bounds on timing noise in MSPs, which may aid the understanding of neutron star interiors and magnetospheres.

Jumps: In combining data from different observing systems or telescopes, arbitrary phase offsets are introduced to remove any differences in instrumental delays. In the case where data from different generations of backend systems are combined, there is often no overlapping data available, strongly limiting the accuracy with which these offsets can be determined. While attempts at achieving reliable jump values between old data sets may not succeed, future instrumental changes may take heed and ensure sufficient overlap of data sets. At present attempts are being made to determine the difference in instrumental delays through simultaneous observation of an artificial nanosecond pulse, which may - if successful - provide an alternative to long periods of overlap.

Parameter uncertainties: In Chapter 3, we have demonstrated the effect small amounts of low-frequency noise can have on the parameter uncertainties that are returned by standard pulsar timing software. The cause of this is that the χ^2 fitting routines currently in use assume that the timing residual data is statistically white and therefore don't take any covariances between the measurement points into account. A revision of the fitting procedure to include such correlation effects is possible through correct whitening of the data before attempting to fit the timing model. While a computationally expensive Monte Carlo-based alternative was used in Chapter 3, a more automated approach for wider use, is under development.

Spectral analysis: In Chapter 4, we have hinted at the value reliable spectral analysis of pulsar timing residuals can have. The spectral analysis technique presented in Chapter 5 only provides reliable measures of low-frequency power, but has already been applied to place bounds on the GWB. In a similar way limits could be placed on pulsar timing instabilities or pulsar planets. A different use was presented in Chapter 3, where the residual spectrum was employed to simulate residuals and obtain more reliable parameter uncertainties. An investigation of MSP spectra with a variety of spectral analysis tools, much like Deeter (1984) and Cordes & Downs (1985) performed on normal pulsars, may be in order. Also, the expansion of the spectral analysis method presented in Chapter 5 to include the TOA uncertainties, may prove useful.

Bayesian analysis: van Haasteren et al. (2008) presented a Bayesian approach to GW detection with pulsar timing data. While a comparative study of the sensitivity of this method and the frequentist approach advocated in Jenet et al. (2005) and Anholm et al. (2008) would be useful, the Bayesian approach may be continued well beyond that. Specifically, Bayesian analysis of timing residuals might provide an independent and radically different means of estimating model parameters and their uncertainties as well as properties of pulsar timing noise or even the residual power spectrum. A comparison or partial assimilation of Bayesian and traditional methods (as most recently described in Hobbs, Edwards & Manchester 2006), may well uncover some unexpected results.

Calibration: In Chapter 3, we applied the polarimetric calibration modelling (PCM) and matrix template matching (MTM) techniques developed by van Straten (2004) and van Straten (2006) to the most recent years of data on PSR J0437−4715. Application of these methods reduced the residual RMS by a factor of about two. While such dramatic improvements are not predicted for all pulsars, the wider and more automated application of these schemes in future research, should be encouraged.

6.4 Increasing the Statistical Significance

The scientific interest of some of our results would be greatly increased if they were to make out part of a larger scientific sample or if observing is continued. This holds specifically for the measurements listed below.

Newton's gravitational constant: Our limit on the variability of Newton's gravitational constant as presented in Verbiest et al. (2008), has already been improved by the VLBI parallax to the PSR J0437−4715 system and is now within a factor of three to the best limit available (from lunar laser ranging (LLR); Williams, Turyshev & Boggs 2004). Because of the smaller time span over which our limit is obtained (ten years as opposed to forty), continued observing can be expected to improve this limit beyond that of LLR. Given the scaling of our measurement uncertainty with $T^{-5/2}$ where T is the time span of the experiment, a further decade of data should bring the precision of the 2σ bound on $|\dot{G}/G|$ below $7\times 10^{-13}\,\mathrm{yr}^{-12}$. Such a limit would demonstrate that the measured variability of the AU (Krasinsky & Brumberg 2004) is due (at least in part) to systematic effects.

Pulsar masses: The mass of PSR J0437−4715, which we determined at $1.76 \pm 0.20\,M_\odot$, suggests certain classes of equations of state for dense nuclear matter can be disproven. This can be substantiated partly by continued observing of this pulsar and partly by the discovery of new pulsars, which should increase the sample size of pulsars with known (and heavy) masses, if these exist. One such discovery has been made since the PSR J0437−4715 mass was published: the mass of PSR J1903+0327 was determined to be $1.74\pm0.04\,M_\odot$ (Champion et al. 2008).

Excess accelerations: In Chapter 3, we have placed a bound on the anomalous acceleration of the Solar System in the direction of PSR J0437−4715. Provided correct error analysis is undertaken, the directional sensitivity of this bound can now be increased by adding the timing residuals from pulsars presented in Chapter 4. We interpreted our limit on the apparent acceleration in terms of a bound on the existence and mass of TNOs. The same principle can, however, be applied to the existence of Earth-mass dark-matter haloes that are predicted to exist within our Galaxy (Diemand, Moore & Stadel 2005). While the event rate of one of these passing close to the Solar System is extremely low, any bound would not only restrict their presence near the Solar System, but also in areas around the neutron stars concerned.

---

[2] The uncertainty in the $\dot{G}/G$ value is currently influenced equally much by the $\dot{P}_{\mathrm{b}}$ value derived from pulsar timing and by the VLBI distance. However, the uncertainty in the VLBI distance will scale with the inverse square root of the number of observing epochs and is therefore not directly dependent on time.

6.5 Closing Remarks

As PTA timing data sets grow in both length and precision, their combination with new or improved processing techniques will allow timing of MSPs to grow ever stronger as an astrophysical tool to probe fundamental physics. Even before completion of the SKA, our knowledge and understanding of fundamental gravitational theories can be expected to evolve considerably. Specifically, we note that a detection of the GWB through pulsar timing looks achievable, since the timing precision and stability of MSPs is provably sufficient. One caveat that goes beyond the scope of this thesis, though, is the existence of this background, since any prediction is only as good as the assumptions that go into it. If SMBH binaries stall rather than merge or if the predicted properties of the GWBs are significantly off, then clearly no detection may be made, though pulsar timing may be used to prove this point. In case the predicted GWBs do exist, the timescale for a detection may well be a decade or less, though a precise value will be dictated by the quantity and quality of new pulsar discoveries and the efficiency of international collaboration.

References

Anholm M., Ballmer S., Creighton J. D. E., Price L. R., Siemens X., 2008, ArXiv e-prints

Arzoumanian Z., Nice D. J., Taylor J. H., Thorsett S. E., 1994, ApJ, 422, 671

Baade W., Zwicky F., 1934, Proc. Nat. Acad. Sci., 20, 259

Backer D. C., Kulkarni S. R., Heiles C., Davis M. M., Goss W. M., 1982, Nature, 300, 615

Bailes M. et al., 1994, ApJ, 425, L41

Bailes M. et al., 1997, ApJ, 481, 386

Becker W., Trümper J., 1993, Nature, 365, 528

Bell J. F., Bailes M., 1996, ApJ, 456, L33

Bell J. F., Bailes M., Bessell M. S., 1993, Nature, 364, 603

Bell J. F., Bailes M., Manchester R. N., Lyne A. G., Camilo F., Sandhu J. S., 1997, MNRAS, 286, 463

Bhat N. D. R., Bailes M., Verbiest J. P. W., 2008, Phys. Rev. D, 77, 124017

Bhattacharya D., van den Heuvel E. P. J., 1991, Phys. Rep., 203, 1

Boyle L. A., Buonanno A., 2008, Phys. Rev. D, 78(4), 043531

Bracewell R., 2000, The Fourier Transform and Its Applications. McGraw–Hill, New York, Third edition

Britton M. C., 2000, ApJ, 532, 1240

Caldwell R. R., Battye R. A., Shellard E. P. S., 1996, Phys. Rev. D, 54, 7146

Camilo F., Nice D. J., Shrauner J. A., Taylor J. H., 1996, ApJ, 469, 819

Camilo F., Kaspi V. M., Lyne A. G., Manchester R. N., Bell J. F., D'Amico N., McKay N. P. F., Crawford F., 2000, ApJ, 541, 367

Camilo F., Ransom S. M., Halpern J. P., Reynolds J., Helfand D. J., Zimmerman N., Sarkissian J., 2006, Nature, 442, 892

Champion D. J. et al., 2008, Science, 320, 1309

Chandrasekhar S., 1931, ApJ, 74, 81

Chen K., Ruderman M., 1993, ApJ, 402, 264

Cognard I., Backer D. C., 2004, ApJ, 612, L125

Coles W. A., Filice J. P., 1984, Nature, 312, 251

Cordes J. M., Downs G. S., 1985, ApJS, 59, 343

Cordes J. M., Lazio T. J. W., 2002, astro-ph/0207156

Counselman C. C., Rankin J. M., 1971, ApJ, 166, 513

Damour T., Deruelle N., 1986, Ann. Inst. H. Poincaré (Physique Théorique), 44, 263

Damour T., Taylor J. H., 1991, ApJ, 366, 501

Damour T., Vilenkin A., 2005, Phys. Rev. D, 71(6), 063510

Deeter J. E., Boynton P. E., 1982, ApJ, 261, 337

Deeter J., 1984, ApJ, 281, 482

Deller A. T., Verbiest J. P. W., Tingay S. J., Bailes M., 2008, ApJ, 685, L67

Detweiler S., 1979, ApJ, 234, 1100

Diemand J., Moore B., Stadel J., 2005, Nature, 433, 389

Duncan R. C., Thompson C., 1992, ApJ, 392, L9

Edwards R. T., Bailes M., 2001, ApJ, 553, 801

Edwards R. T., Bailes M., van Straten W., Britton M. C., 2001, MNRAS, 326, 358

Edwards R. T., Hobbs G. B., Manchester R. N., 2006, MNRAS, 372, 1549

Einstein A., 1905, Annalen der Physik, 322, 891

Enoki M., Inoue K. T., Nagashima M., Sugiyama N., 2004, ApJ, 615, 19

Fienga A., Manche H., Laskar J., Gastineau M., 2008, A&A, 477, 315

Foster R. S., Backer D. C., 1990, ApJ, 361, 300

Foster R. S., Wolszczan A., Camilo F., 1993, ApJ, 410, L91

Freire P. C. C., Ransom S. M., Bégin S., Stairs I. H., Hessels J. W. T., Frey L. H., Camilo F., 2008, ApJ, 675, 670

Gold T., 1968, Nature, 218, 731

Goldreich P., Julian W. H., 1969, ApJ, 157, 869

Grishchuk L. P., 2005, Phys. Uspekhi, , 1235

Groth E. J., 1975, ApJS, 29, 443

Hankins T. H., Rickett B. J., 1975, in Methods in Computational Physics Volume 14 — Radio Astronomy. Academic Press, New York, p. 55

Helfand D. J., Manchester R. N., Taylor J. H., 1975, ApJ, 198, 661

Hellings R. W., Downs G. S., 1983, ApJ, 265, L39

Hemberger D. A., Stinebring D. R., 2008, ApJ, 674, L37

Henrichs H. F., van den Heuvel E. P. J., 1983, Nature, 303, 213

Hewish A., Bell S. J., Pilkington J. D. H., Scott P. F., Collins R. A., 1968, Nature, 217, 709

Hobbs G. B., Edwards R. T., Manchester R. N., 2006, MNRAS, 369, 655

Hobbs G., Lyne A. G., Kramer M., Martin C. E., Jordan C., 2004, MNRAS, 353, 1311

Hobbs G. et al., 2009, MNRAS, accepted

Holmberg J., Flynn C., 2004, MNRAS, 352, 440

Hotan A. W., Bailes M., Ord S. M., 2005, MNRAS, 362, 1267

Hotan A. W., Bailes M., Ord S. M., 2006, MNRAS, 369, 1502

Hotan A. W., van Straten W., Manchester R. N., 2004, PASA, 21, 302

Hulse R. A., Taylor J. H., 1975, ApJ, 195, L51

Irwin A. W., Fukushima T., 1999, A&A, 348, 642

Jacoby B. A., Bailes M., van Kerkwijk M. H., Ord S., Hotan A., Kulkarni S. R., Anderson S. B., 2003, ApJ, 599, L99

Jacoby B. A., Hotan A., Bailes M., Ord S., Kuklarni S. R., 2005, ApJ, 629, L113

Jaffe A. H., Backer D. C., 2003, ApJ, 583, 616

Janssen G. H., Stappers B. W., Kramer M., Purver M., Jessner A., Cognard I., 2008, in Bassa C., Wang Z., Cumming A., Kaspi V. M., eds, 40 Years of Pulsars: Millisecond Pulsars, Magnetars and More. p. 633

Jenet F. A., Hobbs G. B., Lee K. J., Manchester R. N., 2005, ApJ, 625, L123

Jenet F. A. et al., 2006, ApJ, 653, 1571

Johnston S., Galloway D., 1999, MNRAS, 306, L50

Johnston S. et al., 1993, Nature, 361, 613

Kaspi V. M., Taylor J. H., Ryba M., 1994, ApJ, 428, 713

Kopeikin S. M., 1995, ApJ, 439, L5

Kopeikin S. M., 1996, ApJ, 467, L93

Kopeikin S. M., 1999, MNRAS, 305, 563

Kramer M., Lyne A. G., O'Brien J. T., Jordan C. A., Lorimer D. R., 2006, Science, 312, 549

Kramer M. et al., 2006b, Science, 314, 97

Krasinsky G. A., Brumberg V. A., 2004, Celestial Mechanics and Dynamical Astronomy, 90, 267

Lattimer J. M., Prakash M., 2007, Phys. Rep., 442, 109,165

Livingstone M. A., Kaspi V. M., Gavriil F. P., Manchester R. N., Gotthelf E. V. G., Kuiper L., 2007, Ap&SS, 308, 317

Löhmer O., Kramer M., Driebe T., Jessner A., Mitra D., Lyne A. G., 2004, A&A, 426, 631

Lomb N. R., 1976, Astrophys. Space Sci., 39, 447

Lommen A. N., Backer D. C., 2001, ApJ, 562, 297

Lommen A. N., 2002, in Becker W., Lesch H., Trümper J., eds, WE-Heraeus Seminar on Neutron Stars, Pulsars, and Supernova Remnants. Max-Plank-Institut für Extraterrestrische Physik, Garching, p. 114

Lorimer D. R., Kramer M., 2005, Handbook of Pulsar Astronomy. Cambridge University Press

Lorimer D. R. et al., 1995a, ApJ, 439, 933

Lorimer D. R., Yates J. A., Lyne A. G., Gould D. M., 1995b, MNRAS, 273, 411

Lorimer D. R., Lyne A. G., Bailes M., Manchester R. N., D'Amico N., Stappers B. W., Johnston S., Camilo F., 1996, MNRAS, 283, 1383

Lyne A. G., Brinklow A., Middleditch J., Kulkarni S. R., Backer D. C., Clifton T. R., 1987, Nature, 328, 399

Maggiore M., 2000, Phys. Rep., 331, 283

Manchester R. N., Taylor J. H., 1977, Pulsars. Freeman, San Francisco

Manchester R. N. et al., 1996, MNRAS, 279, 1235

Manchester R. N. et al., 2001, MNRAS, 328, 17

Manchester R. N., Hobbs G. B., Teoh A., Hobbs M., 2005, AJ, 129, 1993

Manchester R. N., 2008, in Bassa C., Wang Z., Cumming A., Kaspi V. M., eds, 40 Years of Pulsars: Millisecond Pulsars, Magnetars and More. p. 584

Matsakis D. N., Taylor J. H., Eubanks T. M., 1997, A&A, 326, 924

McHugh M. P., Zalamansky G., Vernotte F., Lantz E., 1996, Phys. Rev. D, 54, 5993

McLaughlin M. A. et al., 2006, Nature, 439, 817

Melrose D., 2004, in Camilo F., Gaensler B. M., eds, Young Neutron Stars and Their Environments, IAU Symposium 218. Astronomical Society of the Pacific, San Francisco, p. 349

Nice D. J., 2006, Adv. Space Res., 38, 2721

Nordtvedt K., 1990, Phys. Rev. Lett., 65, 953

Ord S. M., Jacoby B. A., Hotan A. W., Bailes M., 2006, MNRAS, 371, 337

Ord S. M., Johnston S., Sarkissian J., 2007, Solar Phys., 245, 109

Ostriker J. P., Gunn J. E., 1969, ApJ, 157, 1395

Pacini F., 1968, Nature, 219, 145

Pitjeva E. V., 2005, Solar System Research, 39, 176

Press W. H., Teukolsky S. A., Vetterling W. T., Flannery B. P., 1992, Numerical Recipes: The Art of Scientific Computing, 2nd edition. Cambridge University Press, Cambridge

Prialnik D., 2000, An Introduction to the Theory of Stellar Structure and Evolution. Cambridge University Press

Rajagopal M., Romani R. W., 1995, ApJ, 446, 543

Ransom S. M., Hessels J. W. T., Stairs I. H., Freire P. C. C., Camilo F., Kaspi V. M., Kaplan D. L., 2005, Science, 307, 892

Rickett B. J., 1990, Ann. Rev. Astr. Ap., 28, 561

Rohlfs K., Wilson T. L., 2000, Tools of Radio Astronomy. Springer-Verlag, Berlin

Romani R. W., 1989, in Ögelman H., van den Heuvel E. P. J., eds, Timing Neutron Stars. Kluwer, Dordrecht, p. 113

Ruderman M. A., Shaham J., 1983, Nature, 304, 425

Ruderman M. A., Sutherland P. G., 1975, ApJ, 196, 51

Sandhu J. S., Bailes M., Manchester R. N., Navarro J., Kulkarni S. R., Anderson S. B., 1997, ApJ, 478, L95

Sandhu J. S., 2001, PhD thesis, California Institute of Technology

Sazhin M. V., 1978, Sov. Astron., 22, 36

Scargle J. D., 1982, ApJ, 263, 835

Scargle J. D., 1989, ApJ, 343, 874

Schutz B. F., 1993, A first course in general relativity. Cambridge University Press

Segelstein D. J., Rawley L. A., Stinebring D. R., Fruchter A. S., Taylor J. H., 1986, Nature, 322, 714

Sesana A., Vecchio A., Colacino C. N., 2008, MNRAS, 390, 192

Shapiro I. I., 1964, Phys. Rev. Lett., 13, 789

Shklovskii I. S., 1970, Sov. Astron., 13, 562

Smarr L. L., Blandford R., 1976, ApJ, 207, 574

Splaver E. M., Nice D. J., Stairs I. H., Lommen A. N., Backer D. C., 2005, ApJ, 620, 405

Stairs I. H., 2003, Living Reviews in Relativity, 6, 5, http://www.livingreviews.org/lrr-2003-5/

Standish E. M., 2004, A&A, 417, 1165

Staveley-Smith L. et al., 1996, Publications of the Astronomical Society of Australia, 13, 243

Staveley-Smith L. et al., 1996b, PASA, 13, 243

Stinebring D. R., Ryba M. F., Taylor J. H., Romani R. W., 1990, Phys. Rev. Lett., 65, 285

Taylor J. H., Cordes J. M., 1993, ApJ, 411, 674

Taylor J. H., Weisberg J. M., 1982, ApJ, 253, 908

Taylor J. H., 1992, Philos. Trans. Roy. Soc. London A, 341, 117

Taylor J. H., 1993, in Fontaine G., Tran Thanh van J., eds, Particle Astrophysics. p. 367

Thorsett S. E., Dewey R. J., 1996, Phys. Rev. D, 53, 3468

Torres R. M., Loinard L., Mioduszewski A. J., Rodriguez L. F., 2007, ArXiv e-prints, 708

Toscano M., Sandhu J. S., Bailes M., Manchester R. N., Britton M. C., Kulkarni S. R., Anderson S. B., Stappers B. W., 1999, MNRAS, 307, 925

Valls-Gabaud D., 2007, in IAU Symposium. p. 281

van Haasteren R., Levin Y., McDonald P., Lu T., 2008, ArXiv e-prints

van Straten W., Britton M., Bailes M., Anderson S., Kulkarni S., 2000, in Kramer M., Wex N., Wielebinski R., eds, ASP Conf. Ser. 202: IAU Colloq. 177: Pulsar Astronomy - 2000 and Beyond. Astronomical Society of the Pacific, San Francisco, p. 283

van Straten W., Bailes M., Britton M., Kulkarni S. R., Anderson S. B., Manchester R. N., Sarkissian J., 2001, Nature, 412, 158

van Straten W., 2004, ApJ, 152, 129

van Straten W., 2006, ApJ, 642, 1004

Verbiest J. P. W. et al., 2008, ApJ, 679, 675

Verbunt F., Lewin W. H. G., van Paradijs J., 1989, MNRAS, 241, 51

Walker M. A., Koopmans L. V. E., Stinebring D. R., van Straten W., 2008, MNRAS, 388, 1214

Weise W., 2008, Nuclear Physics A, 805, 115

Wietfeldt R., Straten W. V., Rizzo D. D., Bartel N., Cannon W., Novikov A., 1998, A&AS, 131, 549

Williams J. G., Turyshev S. G., Boggs D. H., 2004, Phys. Rev. Lett., 93, 261101

Wyithe J. S. B., Loeb A., 2003, ApJ, 590, 691

You X.-P. et al., 2007, MNRAS, 378, 493

You X. P., Hobbs G. B., Coles W. A., Manchester R. N., Han J. L., 2007, ApJ, 671, 907

Zakamska N. L., Tremaine S., 2005, AJ, 130, 1939

Appendix A

PTA Sensitivity

In this appendix we derive a simplified formalism for estimating the sensitivity of a pulsar timing array (PTA) to a gravitational wave background (GWB) of given amplitude, A. This derivation produces results equivalent to those resulting from equation (14) of Jenet et al. (2005), but is more readily implemented and inherently treats optimal weighting (or prewhitening) of the pulsar power spectra.

The detection statistic is the sample cross covariance of the residuals of two pulsars i and j, separated by an angle $\theta_{i,j}$:

$$R(\theta_{i,j}) = \frac{1}{N_{\mathrm{s}}} \sum_{t=0}^{T} T_{\mathrm{res},i}(t) \times T_{\mathrm{res},j}(t) \tag{A.1}$$

(where N_{s} is the number of samples in the cross covariance and T is the data span.) The expected value of $R(\theta_{i,j})$ is the covariance of the clock error, which is 100% correlated, plus the cross covariance of the GWB, $\sigma_{\mathrm{GW}}^2 \zeta(\theta_{i,j})$. The clock error can be included in the fit, but one must also include its variance in the variance of the detection statistic. It is better to estimate the clock error and remove it, which also removes its "self noise". So in subsequent analysis we neglect the clock noise. We model the pulsar timing residuals as a GWB term and a noise term: $T_{\mathrm{res}}(t) = T_{\mathrm{GW}}(t) + T_{\mathrm{N}}(t)$, with variances σ_{G}^2 and σ_{N}^2. $\zeta(\theta_{i,j})$ is the cross-correlation curve predicted by Hellings & Downs (1983), as a function of the angle between the pulsars, $\theta_{i,j}$:

$$\zeta(\theta_{i,j}) = \frac{3}{2} x \log x - \frac{x}{4} + \frac{1}{2}$$

in which $x = (1 - \cos\theta_{i,j})/2$.

Since the detection significance will be limited by the variance in the sample

cross covariance, we consider

$$
\begin{aligned}
&\mathrm{Var}(R(\theta_{i,j})) \\
&= \mathrm{Var}\left(\sum \left(\frac{(T_{\mathrm{GW},i} + T_{\mathrm{N},i})(T_{\mathrm{GW},j} + T_{\mathrm{N},j})}{N_{\mathrm{s}}} \right) \right) \\
&= \sigma_{\mathrm{G},i}^2 \sigma_{\mathrm{G},j}^2 \frac{(1 + \zeta(\theta_{i,j})^2)}{N_{\mathrm{s}}} + \frac{\sigma_{\mathrm{N},i}^2 \sigma_{\mathrm{G},j}^2 + \sigma_{\mathrm{G},i}^2 \sigma_{\mathrm{N},j}^2}{N_{\mathrm{s}}} + \frac{\sigma_{\mathrm{N},i}^2 \sigma_{\mathrm{N},j}^2}{N_{\mathrm{s}}}.
\end{aligned}
$$
$$(A.2)$$

Which, after prewhitening, becomes (notice our notation $\sigma_{\mathrm{PW}} = \varsigma$):

$$
\begin{aligned}
&\mathrm{Var}(R_{\mathrm{PW}}(\theta_{i,j})) \\
&= \varsigma_{\mathrm{G}}^4 \frac{(1 + \zeta(\theta_{i,j})^2)}{N_{\mathrm{s}}} + \varsigma_{\mathrm{G}}^2 \frac{(\varsigma_{\mathrm{N},i}^2 + \varsigma_{\mathrm{N},j}^2)}{N_{\mathrm{s}}} + \frac{\varsigma_{\mathrm{N},i}^2 \varsigma_{\mathrm{N},j}^2}{N_{\mathrm{s}}}.
\end{aligned}
$$
$$(A.3)$$

in which we have used $\varsigma_{\mathrm{G},i}^2 = \varsigma_{\mathrm{G},j}^2 = \varsigma_{\mathrm{G}}^2$, which will be proven shortly.

We derive the GWB power from equations (??) and (??), for a GWB with spectral index $\alpha = -2/3$:

$$
P_{\mathrm{GWB}}(f) = K(f/f_{\mathrm{ref}})^{-13/3},
$$
$$(A.4)$$

with K a constant proportional to the amplitude of the GWB and $f_{\mathrm{ref}} = 1\,yr^{-1}$.

Defining the corner frequency, f_{c}, as the frequency at which the gravitational wave power equals the noise power, enables us to use equation (A.4) to determine the noise power: $P_{\mathrm{Noise}} = K(f_{\mathrm{c}}/f_{\mathrm{ref}})^{-13/3}$.

As illustrated by Jenet et al. (2005), the steep spectral index of GWB-induced residuals implies that large gains in sensitivity can be achieved through optimal prewhitening of the data. Assesssment of the variance of both the GWB and noise components of the residuals after prewhitening, can most easily be done through integration of the spectral powers, multiplied by the whitening filter, $W(f)$, which is a type of Wiener filter, designed to minimize the error in the estimation of σ_{G} and is of the form (as derived in §5.3.2): $W(f) = P_{\mathrm{GWB}}/(P_{\mathrm{GWB}} + P_{\mathrm{Noise}})^2$. Rescaling the weighting function thus defined, we get:

$$
W(f) = C \frac{\left(f/f_{\mathrm{ref}}\right)^{-13/3}}{\left(1 + (f/f_{\mathrm{c}})^{-13/3}\right)^2}
$$
$$(A.5)$$

with C a normalisation constant chosen for convenience to be:

$$
C = \left(\sum_f \frac{\left(f/f_{\mathrm{ref}}\right)^{-26/3}}{\left(1 + (f/f_{\mathrm{c}})^{-13/3}\right)^2} \right)^{-1}
$$
$$(A.6)$$

The prewhitened variances then become:

$$
\begin{aligned}
\varsigma_{\mathrm{G}}^2 &= \sum_f K(f/f_{\mathrm{ref}})^{-13/3} C \frac{(f/f_{\mathrm{ref}})^{-13/3}}{\left(1 + (f/f_{\mathrm{c}})^{-13/3}\right)^2} \\
&= K
\end{aligned}
\tag{A.7}
$$

$$
\begin{aligned}
\varsigma_{\mathrm{N}}^2 &= \sum_f K(f_{\mathrm{c}}/f_{\mathrm{ref}})^{-13/3} C \frac{(f/f_{\mathrm{ref}})^{-13/3}}{\left(1 + (f/f_{\mathrm{c}})^{-13/3}\right)^2} \\
&= KC \sum_f \frac{\left(f_{\mathrm{c}} f / f_{\mathrm{ref}}^2\right)^{-13/3}}{\left(1 + (f/f_{\mathrm{c}})^{-13/3}\right)}
\end{aligned}
\tag{A.8}
$$

which justifies our choice for C and shows that, based on our weighting scheme, $\varsigma_{\mathrm{G},i}^2 = \varsigma_{\mathrm{G},j}^2 = K$, as used earlier.

Since the spectra are effectively bandlimited to f_{c} after prewhitening, both the GWB and noise will have the same number of degrees of freedom, namely: $N_{\mathrm{dof}} = 2T_{\mathrm{obs}}f_{\mathrm{c}} - 1$, where T_{obs} is the length of the data span and therefore the inverse of the lowest frequency, implying there are $T_{\mathrm{obs}}f_{\mathrm{c}}$ independent frequencies measured below f_{c}. Since each frequency adds a real and imaginary part, there are twice as many degrees of freedom as there are independent frequency samples; quadratic fitting removes a single degree of freedom from the total. Notice that N_{dof} is the number of independent samples in the cross-covariance spectrum and therefore replaces N_{s} in equations (A.1) and (A.3).

The optimal least-squares estimator for K (and hence for the amplitude of the GWB), based on a given set $R_{\mathrm{PW}}(\theta_{i,j})$ with unequal errors, is (from equations A.1 and A.7) :

$$
\tilde{K} = \frac{\sum R_{\mathrm{PW}}(\theta_{i,j}) \zeta(\theta_{i,j}) / \mathrm{Var}(R_{\mathrm{PW},i,j})}{\sum \zeta(\theta_{i,j})^2 / \mathrm{Var}(R_{\mathrm{PW},i,j})}
\tag{A.9}
$$

The variance of this estimator is:

$$
\mathrm{Var}(\tilde{K}) = \frac{1}{\sum \zeta(\theta_{i,j})^2 / \mathrm{Var}(R_{\mathrm{PW},i,j})}
\tag{A.10}
$$

We can now write the expected signal-to-noise of a given timing array as the square root of the sum over all pulsar pairs of equation (A.7) divided by the square root of equation (A.10)

$$
S = \sqrt{\sum_{i=1}^{N_{\mathrm{psr}}-1} \sum_{j=i+1}^{N_{\mathrm{psr}}} \frac{\varsigma_{\mathrm{G}}^4 \zeta^2 N_{\mathrm{dof}}}{\varsigma_{\mathrm{G}}^4 (1 + \zeta^2) + \varsigma_{\mathrm{G}}^2 (\varsigma_{\mathrm{N},i}^2 + \varsigma_{\mathrm{N},j}^2) + \varsigma_{\mathrm{N},i}^2 \varsigma_{\mathrm{N},j}^2}}.
\tag{A.11}
$$

Rewriting leads to:

$$
S = \sqrt{\sum_{i=1}^{N_{\mathrm{psr}}-1} \sum_{j=i+1}^{N_{\mathrm{psr}}} \frac{\zeta^2 N_{\mathrm{dof}}}{1 + \zeta^2 + \left(\varsigma_i'\right)^2 + \left(\varsigma_j'\right)^2 + \left(\varsigma_i' \varsigma_j'\right)^2}}
\tag{A.12}
$$

where $\varsigma_i' = \varsigma_{\mathrm{N},i}/\varsigma_{\mathrm{G}}$.

Appendix B

Nomenclature

The following glossary defines the various mathematical symbols and acronyms used throughout the thesis.

A	Dimensionless amplitude of the GWB
a	Semi-major axis of the binary orbit
α	Right ascension, RA
A_{e}	True anomaly of the binary orbit
$a_{\odot}$	Acceleration of the Solar System
a_{i}	Amplitude of the electric field in direction i.
A/D	Analogue-to-digital converter
AFB	Analogue filter bank (also "FB")
AOP	Annual-orbital parallax
ASKAP	Australian SKA pathfinder
AU	Astronomical unit ($1\,\mathrm{AU} = 149597870\,\mathrm{km}$)
AXP	Anomalous X-ray pulsar
B	Bandwidth
B	Source brightness
B_0	Magnetic field strength at the surface of the pulsar (Gauss)
$\vec{b}$	Vector pointing from the BB to the pulsar
BAT	Barycentric arrival time
BB	Binary barycentre
c	speed of light ($= 3 \times 10^8\,\mathrm{m/s}$)
CPSR/CPSR2	Caltech-Parkes-Swinburne recorder versions one and two.
D	Dispersion constant, $D = 4.15 \times 10^3\,\mathrm{MHz^2 pc^{-1} cm^3 s}$
$\vec{d}$	Vector pointing from the SSB to the pulsar or to the BB
Δ	Timing delay
δ	Declination, dec
D_{k}	Kinematic distance
D_{π}	Parallax distance

δ_x	Kronecker delta ($\delta_x = 1$ if $x = 0$; $\delta_x = 0$ if $x \neq 0$).
DFT	discrete Fourier transform
DM	Dispersion measure or integrated electron density
Δ_8	Stability parameter
E	Fourier transform of e
e	Orbital eccentricity
$\vec{e}$	Electric field vector, decomposed into e_x, e_y and $e_z = 0$.
EOS	Equation of state
EPTA	European pulsar timing array
f	Observing frequency
$f_{\rm ref}$	Reference frequency, $f_{\rm ref} = 1\,{\rm yr}^{-1}$.
ϕ	Phase
FAST	Five hundred metre aperture spherical telescope
FFT	Fast Fourier transform
FPTM	Fast pulsar timing machine
G	Gain
G	Newton's gravitational constant ($G = 6.67259 \times 10^{-11}\,{\rm Nm^2 kg^{-2}}$)
γ	Gravitational redshift parameter
GBT	Green Bank telescope
GC	Globular cluster
GW	Gravitational wave
GWB	Gravitational wave background
GR	General relativity
H_0	Hubble constant
h	Planck's constant ($h = 6.6260755 \times 10^{-34}\,{\rm Js}$)
h_c	Characteristic strain spectrum of the GWB
I	moment of inertia of the pulsar ($\approx 10^{45}\,{\rm g\ cm^2}$)
i	Inclination angle of the binary orbit. $i = 0°$ is seen as a clockwise rotation; $i = 90°$ is an edge-on orbit; $i = 180°$ is counter-clockwise rotation.
IF	Intermediate frequency
IPTA	International pulsar timing array
ISM	Interstellar medium
Jy	Jansky, unit of flux density ($1\,{\rm Jy} = 10^{-26}\,{\rm W\ m^{-2} Hz^{-1}}$)
k	Boltzmann's constant ($k = 1.380658 \times 10^{-23}\,{\rm J/K}$)
λ	Wavelength
LEAP	Large European array for pulsars - a PTA based on interferometric coupling of the radio telescopes that form the EPTA.
LLR	Lunar laser ranging
LNA	Low noise amplifier
LO	Local oscillator
M	Mass of the binary system ($M = M_{\rm psr} + M_c$)
$M_{\rm psr}$	Pulsar mass
M_c	Mass of the binary companion

$M_\odot$	Solar mass (1.989×10^{30} kg)
μ	Proper motion (often decomposed in RA and dec: μ_α; μ_δ)
MeerKAT	Extended Karoo array telescope. The South African SKA prototype
MSP	Millisecond pulsar
MTM	Matrix template matching
ν	Observing frequency ($\nu = f$)
$\ddot{\nu}$	Second time derivative of the pulsar spin frequency
n_e	Electron density (cm^{-3})
N_p	Number of polarisations
NANOGrav	North American nanohertz observatory for gravitational waves (North American pulsar timing array)
P	Pulse period
P	Power
$\dot{P}$	Spin period derivative, spindown
$\vec{p}$	Vector pointing from the telescope to the pulsar
π	Parallax, PX
P_b	Binary period (days)
$\dot{P}_b$	First derivative of the binary period, orbital decay
PCM	Polarimetric calibration modelling
PPTA	Parkes pulsar timing array
PTA	Pulsar timing array
R	Pulsar radius
r	Shapiro delay range
$\vec{r}$	Vector pointing from the telescope to the SSB
$\bar{\rho}$	Coherency matrix. Contains the coherency products.
RF	Radio frequency
RRAT	Rotating radio transient
S	Stokes parameters. Contains four components: I, Q, U, V.
S	PTA sensitivity (in standard deviations) to a GWB.
S_0	Total intensity
S_{peak}	Brightness of the pulse peak
s	Shapiro delay shape
σ	Standard deviation, RMS
ς_0	White noise variance of a pulse profile
ς_G	Timing RMS due to the GWB (or due to other noise sources in case of ς_N, after prewhitening.
σ_G	Timing RMS due to the GWB.
σ_N	Timing RMS due to noise sources other than the GWB.
σ_z	Stability parameter based on Allen variance
SAT	Site arrival time
SGR	Soft gamma repeater
SKA	Square kilometre array
SMBH	Supermassive black hole

SNR	Signal to noise ratio
sr	Steradian, unit of solid angle
SSB	Solar system barycentre
SSE	Solar system ephemerides
T	Time span of the data set, length of observational campaign.
T_0	Time of periastron passage
T_A	Antenna temperature
T_b	Brightness temperature
T_N	Noise temperature
$\theta_{i,j}$	Angular separation between pulsars i and j.
τ_c	Characteristic age
TAI	Temps atomique international - international atomic time
TNO	Trans-Neptunian object
TOA	(pulse) time-of-arrival
u	Eccentric anomaly of the binary orbit
$\vec{v}$	Pulsar (or binary) velocity. Note that proper motion μ is the projection of $\vec{v}$ onto the plane of the sky.
VLBI	Very long baseline interferometry
$W(f)$	Wiener filter for prewhitening of residuals.
Ω	Longitude of ascending node. Defined from North through East.
Ω_{gw}	Energy density of the GWB per unit logarithmic frequency interval.
ω	Longitude of periastron
$\dot{\omega}$	Periastron advance
$x = a \sin i$	Projected semi-major axis of the binary orbit
$\zeta(\theta)$	Hellings & Downs correlation at separation θ.

Publications

The following publications appear as chapters in this thesis:

Precision Timing of PSR J0437−4715: An Accurate Pulsar Distance, a High Pulsar Mass, and a Limit on the Variation of Newton's Gravitational Constant Verbiest, J. P. W.; Bailes, M.; van Straten, W.; Hobbs, G. B.; Edwards, R. T.; Manchester, R. N.; Bhat, N. D. R.; Sarkissian, J. M.; Jacoby, B. A. & Kulkarni, S. R. *The Astrophysical Journal* Volume 679, Issue 1, pp. 675−680, May 2008

The following papers were prepared with the assistance of the candidate during the course of this thesis:

Upper Bounds on the Low-Frequency Stochastic Gravitational Wave Background from Pulsar Timing Observations: Current Limits and Future Prospects Jenet, F. A.; Hobbs, G. B.; van Straten, W.; Manchester, R. N.; Bailes, M.; Verbiest, J. P. W.; Edwards, R. T.; Hotan, A. W.; Sarkissian, J. M. & Ord, S. M. *The Astrophysical Journal* Volume 653, Issue 2, pp. 1571−1576, December 2006

Dispersion measure variations and their effect on precision pulsar timing You, X. P.; Hobbs, G.; Coles, W. A.; Manchester, R. N.; Edwards, R.; Bailes, M.; Sarkissian, J.; Verbiest, J. P. W.; van Straten, W.; Hotan, A.; Ord, S.; Jenet, F.; Bhat, N. D. R. & Teoh, A. *Monthly Notices of the Royal Astronomical Society* Volume 378, Issue 2, pp. 493−506, June 2007

Using pulsars to limit the existence of a gravitational wave background Hobbs, G.; Jenet, F.; Lommen, A.; Coles, W.; Verbiest, J. P. W.& Manchester, R. *40 Years of Pulsars: Millisecond Pulsars, Magnetars and More. AIP Conference Proceedings* Volume 983, pp. 630−632, February 2008

Gravitational-radiation losses from the pulsar−white-dwarf binary PSR J1142−6545 Bhat, N. D. R.; Bailes, M. & Verbiest, J. P. W. *Physical Review D* Volume 77, Issue 12, id. 124017, June 2008

Extremely High Precision VLBI Astrometry of PSR J0437−4715 and Implications for Theories of Gravity Deller, A. T.; Verbiest, J. P. W.; Tingay, S. J. & Bailes, M. *The Astrophysical Journal* Volume 685, Issue 1, pp. L67−70, September 2008

Gravitational wave detection using pulsars: status of the Parkes Pulsar Timing Array project Hobbs, G. B.; Bailes, M.; Bhat, N. D. R.; Burke-Spolaor,

S.; Champion, D. J.; Coles, W.; Hotan, A.; Jenet, F.; Kedziora-Chudczer, L.; Khoo, J.; Lee, K. J.; Lommen, A.; Manchester, R. N.; Reynolds, J.; Sarkissian, J.; van Straten, W.; To, S.; Verbiest, J. P. W.; Yardley, D. & You, X. P. *Publications of the Astronomical Society of Australia* Accepted for publication in Volume 26, 2009

TEMPO2, a new pulsar timing package. III: Gravitational wave simulation Hobbs, G.; Jenet, F.; Lee, K. J.; Verbiest, J. P. W.; Yardley, D.; Manchester, R.; Lommen, A.; Coles, W.; Edwards, R. & Shettigara, C. *Monthly Notices of the Royal Astronomical Society* Accepted for publication in 2009